

Ab initio investigations of the Rashba spin-orbit coupling in the electronic structure of surfaces

Dissertation

zur Erlangung des akademischen Grades
doctor rerum naturalium (Dr. rer. nat.)

vorgelegt der
Naturwissenschaftlichen Fakultät II
der Martin-Luther-Universität Halle-Wittenberg

von **S. Hossein Mirhosseini**
geboren am 03.01.1976 in Yazd, Iran

Gutachterinnen / Gutachter:

1. Jürgen Henk, PD Dr.
2. Wolfram Hergert, Prof. Dr.
3. Evgueni Chulkov, Prof. Dr.

Halle an der Saale, 20. Mai 2010

This thesis is based on the following publications:

- * H. Mirhosseini, A. Ernst, S. Ostanin, and J. Henk
Tuning independently the Fermi energy and spin splitting in Rashba systems:
Ternary alloys on Ag(111)
arXiv:cond-mat.matrl-sci: 1005.1162v1 (2010)
- * H. Mirhosseini, A. Ernst, and J. Henk
Electron correlation beyond local density approximation: Self-interaction correction
in Gadolinium
J. Phys.: Condens. Matter 22 245601 (2010)
- * H. Mirhosseini, I. V. Maznichenko, S. Abdelouahed, S. Ostanin, A. Ernst, I. Mertig,
and J. Henk
Towards a ferroelectric control of Rashba spin-orbit coupling: Bi on BaTiO₃ (001)
from first principles
Phys. Rev. B **80**, 073406 (2010)
- * H. Mirhosseini, J. Henk, A. Ernst, S. Ostanin, C.-T. Chiang, P. Yu,
A. Winkelmann, and J. Kirschner
Unconventional spin structure of unoccupied spin-orbit split surface states in surface
alloys
Phys. Rev. B **79**, 245428 (2009)
- * L. Moreschini, A. Bendounan, I. Gierz, C. R. Ast, H. Mirhosseini, H. Höchst,
K. Kern, J. Henk, A. Ernst, S. Ostanin, F. Reinert, and M. Grioni
Assessing the atomic contribution to the Rashba spin-orbit splitting in surface alloys:
Sb/Ag(111)
Phys. Rev. B **79**, 075424 (2009)
- * Emmanouil Frantzeskakis, Stéphane Pons, Hossein Mirhosseini, Jürgen Henk,
Christian R. Ast, and Marco Grioni
Tunable Spin Gaps in a Quantum-Confined Geometry
Phys. Rev. Lett. **101**, 196805 (2008)

Abstract In the emerging field of spin electronics, a new generation of devices utilizes the Rashba effect which is present in systems with inversion asymmetry. The present work reports on selected *ab initio* investigations of the Rashba effect in surfaces. The main aims of this work are to gain a comprehensive understanding of the ‘common Rashba systems’ and to explore the new features of ‘more complicated Rashba systems’.

To achieve the first goal we studied the Rashba parameters and Rashba characteristics of the ordered surface alloy Sb/Ag(111) as well as of disordered binary surface alloys, i. e. $\text{Bi}_x\text{Sb}_{1-x}/\text{Ag}(111)$ and $\text{Pb}_x\text{Sb}_{1-x}/\text{Ag}(111)$, and disordered ternary surface alloys, i. e. $\text{Bi}_x\text{Pb}_y\text{Sb}_{1-x-y}/\text{Ag}(111)$. The results of our investigation in conjunction with those previously carried out make a systematic study of this unique class of Rashba systems possible.

In this work, ‘more complicated Rashba systems’ include the system of Bi/Cu(111) with an unconventional spin topology, the system of Bi/BaTiO₃ with a ferroelectric material as the substrate, the trilayer system of BiAg/Ag/Si in which quantum well states and surface states interact, and the (0001) surface of gadolinium as a strongly correlated magnetic material. The features of these systems are captured either by our full-relativistic code or by model calculations. A good knowledge of the influential parameters in the common Rashba systems, i. e. the first goal, is essential to understanding the behavior of the more complicated systems.

The first part of the thesis consists of four short chapters describing the basics of the surface states and the Rashba effect, the importance of the self-interaction correction, and the methods used for our calculations. The second part consists of a short review of the results and includes six selected papers.

Contents

1	Introduction	1
2	The Rashba splitting of surface states	3
2.1	Surface states	3
2.2	Rashba effect	4
3	Self-interaction correction	7
3.1	Density-functional theory	7
3.2	Local (spin) density approximation	8
3.3	Local self-interaction correction	9
3.4	Transition state approximation	10
4	A brief review of methods	13
4.1	Multiple scattering theory	13
4.1.1	The Green's function in MST	15
4.2	Layer KKR	17
4.3	Coherent potential approximation	18
4.3.1	Single-site KKR-CPA	19
5	Selected results	21
5.1	Systematic study	21
5.2	More complicated systems	27
5.3	Summary	34
5.4	Selected results	34
	Paper I: Assessing the atomic contribution to the Rashba spin-orbit splitting in surface alloys: Sb/Ag(111)	35
	Paper II: Tuning independently the Fermi energy and spin splitting in Rashba systems: Ternary surface alloys on Ag(111)	43
	Paper III: Unconventional spin topology in surface alloys with Rashba-type spin splitting	57
	Paper IV: Towards a ferroelectric control of Rashba spin-orbit coupling: Bi on BaTiO ₃ (001) from first principles	65
	Paper V: Tunable Spin Gaps in a Quantum-Confined Geometry	71

Paper VI: Electron correlation beyond local density approximation: Self- interaction correction in Gadolinium	77
Acknowledgment	91
Erklärung an Eides statt	92
Curriculum Vitae	93

Chapter 1

Introduction

The spin-orbit interaction, that is the coupling of the orbital angular momentum and the spin of an electron, manifests itself in the electronic structure of solids in various ways. For example, it results in the magnetocrystalline anisotropy in magnetic samples and is the origin of the magnetic dichroism in x-ray absorption. Other examples are the Dresselhaus effect and the Rashba effect in systems with broken inversion symmetry.

In nonmagnetic materials with inversion symmetry, Kramers' degeneracy implies non spin-polarized electronic states. Spin-orbit interaction shows up as Dresselhaus effect if the inversion symmetry of a bulk solid is broken [1]. At an interface, e.g. in a semiconductor heterostructure, inversion symmetry is broken in a natural way. The band-bending present in semiconductors heterostructures can be viewed as a potential gradient perpendicular to the interface plane. The spin-orbit coupling, that is – in a nonrelativistic formulation – proportional to the gradient of the potential, results in Rashba spin-orbit coupling and consequently in polarized electronic states in a two-dimensional electron gas (2DEG) confined to the band-bending region. The Rashba effect lifts Kramers' degeneracy and can be probed by de-Haas-van-Alphen oscillations [2].

The standard model for the Rashba effect relies on an isotropic two-dimensional electron gas (see section 2.2). The potential gradient corresponds to an effective magnetic field in the rest frame of the electron and leads to a Zeeman splitting. Consequently, the splitting is proportional to the electron velocity. The Rashba effect shows up in a unique spin topology of the electronic states.

At metal surfaces, effects similar to those in semiconductor 2DEGs are observed. Here, the 2DEG is replaced by surface states (introduced in chapter 2.1). The potential gradient is given by the image-potential barrier. This Rashba effect has been intensively studied for the surface states of Au(111) [3], giving a paradigm of Rashba-split surface states [4–6]. Bi grown on Ag(111) results in an ordered superstructure. The surface state within the Bi-Ag top layer shows an unmatched Rashba splitting [5]: The experimental Rashba parameter of $3.05 \text{ eV}\text{\AA}$, that is 9 times larger than in Au(111), is explained by an in-plane potential gradient which is intrinsic to the (111) surfaces of cubic solids [7].

The present work reports on selected *ab initio* investigations of the Rashba effect in surfaces. For the ordered surface alloy Sb/Ag(111), which shows a small spin split-

ting, the atomic contribution to the Rashba spin-orbit coupling is studied in **paper I**. Knowing the properties of three ordered surface alloys, (Bi, Pb, and Sb)/Ag(111), the challenge is how to tune these properties. In **paper II** we examine the possibility to independently tune the Rashba characteristics in disordered ternary surface alloys $\text{Bi}_x\text{Pb}_y\text{Sb}_{1-x-y}/\text{Ag}(111)$. Surface alloying is not the only way to modify the Rashba characteristics. The control of the Rashba characteristics is the topic of **paper IV** and **paper V**. **Paper IV** proposes a ferroelectric controlling of the Rashba spin-orbit coupling which may be utilized in future spin-electronic devices. The electronic structure at the Fermi level of the trilayer system BiAg/Ag/Si is studied in **paper V**.

Not all Rashba systems follow the standard Rashba model. Bi/Cu(111) is an example and is studied in **paper III**. Hybridization that is the reason of the unconventional spin topology in Bi/Cu(111) is a fundamental effect and our findings are relevant for spin electronics in general.

The magnetic system gadolinium requires a treatment which is beyond the conventional local spin-density approximation, due to the strong electronic correlation. A self-interaction correction method, which is one of the remedies to the self-interaction error, is applied to study strongly correlated gadolinium. **Paper VI** studies the Rashba-like behavior of the surface states of Gd(0001) as well as the magnetic properties of bulk Gd.

Chapter 2

The Rashba splitting of surface states

2.1 Surface states

In an infinite crystal the problem of band structure calculations, in the framework of density functional theory, is based on the motion of an electron in an effective periodic potential. This assumption for the boundary condition obscures some features of interest associated with a finite crystal, e.g. the surface of a crystal. In a finite crystal there is no restriction for wavevectors to be real, consequently \mathbf{k} may assume complex values. The corresponding energies lie inside the region that is forbidden for real \mathbf{k} . The wavefunctions describing these levels, the surface states, are damped in the direction of the vacuum. Surface states are also damped inside the crystal but in an oscillatory way.

Surface states were first studied by Tamm in a semi-finite crystal using a direct-matching approach [8]. The calculations were carried out in a one dimensional system with terminated Kronig-Penney (KP) potential [9]. Tamm's pioneering work was followed by a number of publications. Maue used a nearly-free-electron approach and connects the existence condition of a surface state with the form of the crystal potential and the surface position. Shockley [10] considered the formation of surface states as the function of the lattice constant. He defined Tamm-Goodwin surface states and Maue-Shockley surface states. The latter occur for a periodic potential without edge effects in the end cell while the former appear when the end cell is distorted. Zak's work [11] connects the appearance of surface states to the symmetry of the unperturbed energy bands.

Another way of looking at surface states is to view these states as an electron trapped between the surface of the crystal and the surface barrier potential. Suppose an electron outside the crystal travels to and away from the surface. If the wave ψ_- carries unit flux towards the crystal a portion of the wave will be reflected

$$\psi_+ = r_C e^{i\phi_C} \psi_-, \quad (2.1)$$

where ψ_+ carries flux away from the crystal towards the surface barrier. In its turn ψ_+

will impinge on the surface barrier and be reflected back towards the crystal

$$\psi_- = r_B e^{i\phi_B} r_C e^{i\phi_C} \psi_-, \quad (2.2)$$

where r_B and r_C are the real part of the reflection coefficients and ϕ_B and ϕ_C are the phase changes occurring upon reflection. Summing up all the repeated scatterings gives the total amplitude of ψ_- which is proportional to

$$[1 - r_B r_C \exp i(\phi_B + \phi_C)]^{-1}. \quad (2.3)$$

A pole in (2.3) denotes a bound state. Thus the conditions of appearing surface states are

$$r_B r_C = 1 \quad (2.4)$$

and

$$\phi_B \phi_C = 2\pi n. \quad (2.5)$$

Since $r_B \leq 1$ and $r_C \leq 1$, (2.4) gives that both are unity. This means that there are no propagating state within the crystal and no possibility of flux escaping from the crystal into vacuum.

Image states can be classified into two categories [12]: (*i*) crystal-induced states that originate from rapid variation of the phase changes occurring upon reflection from the crystal surface, and (*ii*) image-induced states that appear due to rapid variation of the phase changes occurring upon reflection from the barrier potential.

2.2 Rashba effect

Spin-orbit coupling (SOC) is a relativistic effect. In the rest frame of an electron moving in an electric field, the electron experiences a magnetic field. The Zeeman interaction

$$H_{zee} = 2\mu_0\mu_B \mathbf{H} \cdot \mathbf{s} \quad (2.6)$$

aligns the electron spin \mathbf{s} parallel to the magnetic field \mathbf{H} and consequently makes a direction of spin more favorable than another one. This results in a splitting in energy. The importance of the spin-orbit interaction, although its magnitude is small, is that it breaks the symmetry of the Schrödinger equation. The spin-orbit interaction can be included in the Schrödinger equation by adding the Pauli Hamiltonian

$$H_{SOC} = \alpha \mathbf{L} \cdot \mathbf{S}. \quad (2.7)$$

For a spherical potential $V(\mathbf{r})$, \mathbf{L} and \mathbf{S} are orbital and spin momentum, and the spin-orbit parameter α can be written as

$$\alpha = \frac{\hbar}{2m^2c^2} \frac{1}{r} \frac{dV(r)}{dr}. \quad (2.8)$$

In order to treat magnetic systems in a non-perturbative way, one starts with the Dirac equation

$$H = \boldsymbol{\alpha} \cdot \mathbf{p}c + \beta mc^2 + V, \quad (2.9)$$

where $\boldsymbol{\alpha}$ and β are Dirac matrices [13].

If a Hamiltonian is invariant under time reversal, e.g. the above Dirac Hamiltonian, it follows that $E(\mathbf{k}, \uparrow) = E(-\mathbf{k}, \downarrow)$. If a crystal has a center of inversion, it implies that $E(\mathbf{k}, \uparrow) = E(-\mathbf{k}, \uparrow)$. Combining these relations yields Kramers' degeneracy, $E(\mathbf{k}, \uparrow) = E(\mathbf{k}, \downarrow)$, which states in a crystal with the center of inversion the electronic states are not spin-polarized.

Spin degeneracy is a result of both time-reversal and inversion symmetry. At a surface, breaking of the inversion symmetry results, via the spin-orbit coupling, to a splitting in the dispersion relation. In a two-dimensional free-electron gas the potential in z direction confines electrons to the surface. Thus, the spin-orbit Hamiltonian can be written as

$$H_{SOC} = \gamma_R(\sigma_x \partial_y - \sigma_y \partial_x), \quad (2.10)$$

where γ_R is the Rashba parameter which is proportional to the gradient of the potential V in z direction. Inserting the free-electron eigenfunctions in the Hamiltonian which includes the Rashba term (2.10) yields a splitting in the free electron eigenvalues,

$$E_{\pm} = \frac{\hbar^2 k^2}{2m^*} \pm \gamma_R |\mathbf{k}_{\parallel}|. \quad (2.11)$$

The eigenfunctions are fully spin-polarized

$$\mathbf{P}_{\pm}(\mathbf{k}_{\parallel}) = \frac{1}{|\mathbf{k}_{\parallel}|} \begin{pmatrix} \pm k_y \\ \mp k_x \\ 0 \end{pmatrix}, \quad (2.12)$$

The spins of the electronic states are in the xy plane, align in opposite directions, and are perpendicular to the wave vector \mathbf{k}_{\parallel} .

The nearly free electron (NFE) model is able to describe the nature of the splitting but it cannot give a correct quantitative result. The experimental splitting, e.g. in Au(111) [3], is much larger than what is estimated by a NFE model. This small splitting is an artifact of the model; the core region of the ionic potential, where the gradient of the potential is large, is neglected.

It has been shown, in the framework of the tight-binding model, that γ is linearly dependent on (i) the atomic spin-orbit splitting and (ii) the surface potential. A large atomic spin-orbit interaction (SOI) and a large gradient of the surface potential result in a large splitting of the surface state dispersion [14]. Adsorption of oxygen, for example, enhances the spin splitting due to increasing of the surface-potential gradient [15].

A potential gradient within the plane leads to another contribution to the spin-orbit interaction [7]. The interplay of both contributions, in-plane and out-of-plane gradient potential, manifests itself as an enhanced splitting in the anisotropic confinement plane

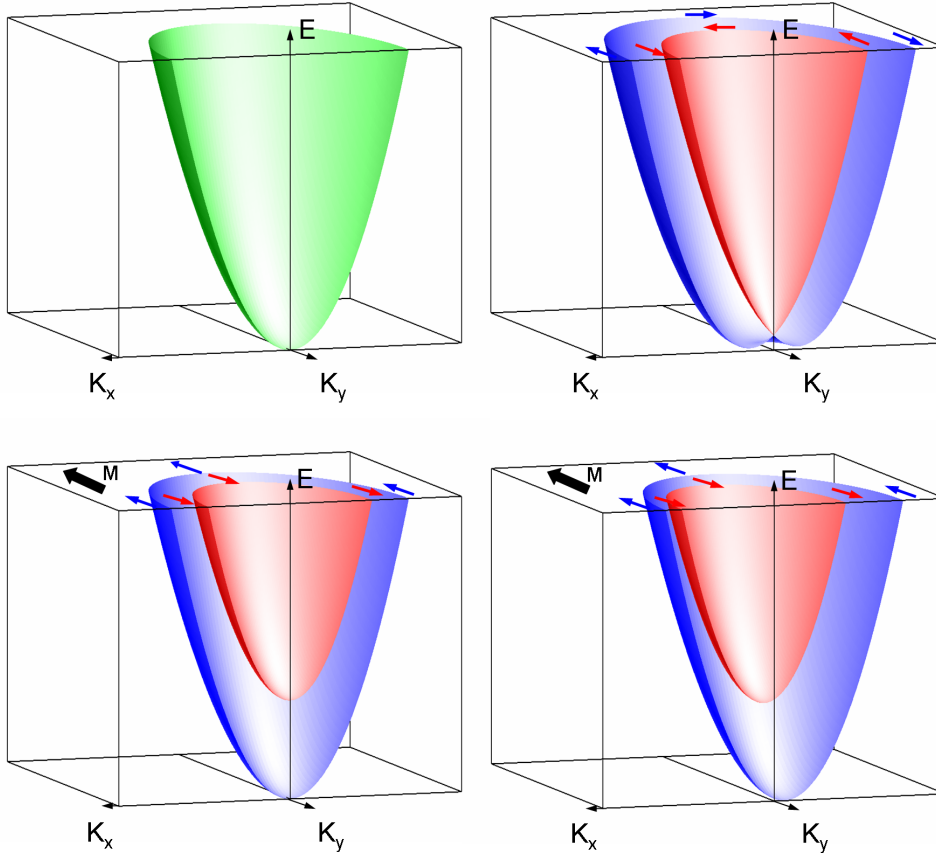


Figure 2.1: Schematic spin structure of Rashba-split and exchange-split surface states at a non-magnetic surface (top) and at a magnetic surface (bottom). The left panels show systems with inversion symmetry while the right panels show systems without inversion symmetry. The Rashba spin-orbit coupling in a ferromagnetic two-dimensional electron with in-plane magnetization \mathbf{M} removes the inversion symmetry of the spin-split band structure, $E(+\mathbf{k}_{\parallel}) \neq E(-\mathbf{k}_{\parallel})$ for $\mathbf{k}_{\parallel} \perp \mathbf{M}$ (bottom right).

and a nonzero spin polarization in z direction. First-principles calculations predicts a nonzero but small \mathbf{P}_z for L-gap surface states in Au(111) [6] and a sizeable \mathbf{P}_z for surface alloys, e.g. $(\sqrt{3} \times \sqrt{3})\text{-R}30^\circ\text{Bi/Ag(111)}$ [5].

At a magnetic surface, e.g. Gd(0001), spin degeneracy is lifted by the exchange interaction and spins are align along the quantization axis. The effect of the spin-orbit interaction is mainly a modification of the energy dispersion. Figure 5.4 depicts the spin structure of Rashba split surface states at a non-magnetic and at a magnetic surface.

Chapter 3

Self-interaction correction

3.1 Density-functional theory

An exact description of the many-body problem requires the solution of the Schrödinger equation with $3N$ coupled spatial degrees of freedom. For macroscopic systems the number of electrons is quite large and the solution to the N -electron problem has to be approximated.

The original density-functional theory (DFT) is the Thomas-Fermi (TF) method which – although is not accurate enough for present-day calculations – illustrates the way DFT works. In TF theory the total-energy functional consists of the kinetic-energy functional (an explicit function of the density of a non-interacting electron system), the external energy functional, the local exchange term (after Dirac) and the classical Hartree energy functional. The attraction of the method is evident by the fact that the equation for the density is quite simpler than that for the many-body wavefunction [16].

The electron density of a many-body system, $\rho(\mathbf{r})$, determines the number of electrons N and the external potential $V_{ext}(\mathbf{r})$. The Hohenberg and Kohn (HK) [17] theorems state that for any system of interacting particles in an external potential $V_{ext}(\mathbf{r})$, the latter is determined uniquely, except for a constant, by $\rho(\mathbf{r})$. Furthermore the theorems introduce the variational principle for the energy: The universal functional of the energy in terms of density can be defined such as the exact ground-state energy of the system is the global minimum value of this functional.

The HK theorems provide no guidance to construct the functionals. It was the *ansatz* made by Kohn and Sham (KS) [18] that makes DFT the most widely method for electronic structure calculations. The KS *ansatz* assumes that the ground-state electron density of the interacting system is equal to that of some chosen non-interacting reference system. The ground-state wavefunction of the non-interacting system can be expressed by a Slater determinant of N one-particle solutions, $\phi_i(\mathbf{r})$, with lowest energy. The

corresponding electron density and the kinetic energy can be written as ¹

$$\rho_s(\mathbf{r}) = \sum_i^N \phi_i^*(\mathbf{r})\phi_i(\mathbf{r}) \quad (3.1)$$

and

$$T_s = - \sum_i^N \langle \phi_i | \nabla^2 | \phi_i \rangle, \quad (3.2)$$

respectively. The kinetic energy of the non-interaction system is not the exact kinetic energy of the system of interest, $T[\rho]$. The KS idea is to set up a problem in such a way that $T_s[\rho]$ is its kinetic energy component. The KS energy functional can then be written as

$$E_{KS}[\rho] = T_s[\rho] + E_H[\rho] + E_{ext}[\rho] + E_{xc}[\rho]. \quad (3.3)$$

The exchange-correlation energy $E_{xc}[\rho]$ contains the difference between the kinetic energy of interacting and non-interacting system, and the nonclassical part of the electron-electron interaction

$$E_{xc}[\rho] \equiv T[\rho] - T_s[\rho] + V_{ee}[\rho] - E_H[\rho], \quad (3.4)$$

where $V_{ee}[\rho]$ and $E_H[\rho]$ indicate electron-electron energy functional and Hartree term, respectively.

3.2 Local (spin) density approximation

The choice of the approximation for the exchange-correlation potential is crucial. Solids can often be described as being close to the limit of the homogeneous electron gas. In this limit the effects of exchange and correlation are local in character and the local density approximation (LDA) [18] is a suitable approximation.

In LDA the exchange-correlation energy per particle of a homogenous electron gas is used to make the exchange-correlation potential

$$E_{xc}^{LDA}[\rho] = \int d\mathbf{r} \rho(\mathbf{r}) \epsilon_{xc}^{hom}(\rho(\mathbf{r})), \quad (3.5)$$

$$V_{xc}^{LDA}(\mathbf{r}) = \epsilon_{xc}(\rho(\mathbf{r})) + \rho(\mathbf{r}) \frac{\delta \epsilon_{xc}(\rho(\mathbf{r}))}{\delta \rho(\mathbf{r})}. \quad (3.6)$$

The second term in the last equation is called response potential [19] and is due to the change in the exchange-correlation hole density.

The local spin density (LSD) approximation is the spin-polarized extension of LDA. The LSD exchange-correlation potential is expressed as

$$V_{xc,\sigma}^{LSD}(\mathbf{r}) = \frac{\delta}{\delta \rho_\sigma} (\rho(\mathbf{r}) \epsilon_{xc}(\rho_\uparrow, \rho_\downarrow)). \quad (3.7)$$

¹In the following we use Rydberg atomic units, $\hbar = 1$ and $2m = 1$.

3.3 Local self-interaction correction

Although the LDA electronic structure cannot claim quantitative accuracy for the determination of the electronic structure, LDA generally provides a qualitative understanding. The success of LDA, which is impressive despite its crude presumption, must be largely due to a cancellation of errors [16]. Despite of the LDA's success, there are serious shortcomings: The properties of $3d$ metal oxides are described badly, the band gap of semiconductors are underestimated, in f -systems the density of states is in strong disagreement with experiment, in some cases LDA gives qualitatively wrong results for Mott-Hubard insulators, to name a few. Some of the discrepancies are due to the restriction of DFT to describe the ground-state properties. But some failures can be attributed to the partial cancellation of the spurious self-interaction of an electron with itself, which is present in the KS effective potential. This kind of systematic error can be corrected by removing the self-interaction from the total energy functional. Perdew and Zunger [20], who first addressed this problem in the context of DFT, proposed a self-interaction version of E_{xc} ,

$$E_{xc}^{SIC}[\rho_{\alpha\sigma}] = E_{xc}^{LSD}[\rho_{\uparrow}, \rho_{\downarrow}] - \sum_{\alpha\sigma}^{occ} (E_H[\rho_{\alpha\sigma}] + E_{xc}^{LSD}[\rho_{\alpha\sigma}, 0]), \quad (3.8)$$

where $\alpha\sigma$ is a combined index labeling the orbital and spin, respectively. The SI correction potential becomes

$$V_{\alpha\sigma}^{SIC}(\mathbf{r}) = \frac{\delta E_{xc}^{LSD}[\rho_{\uparrow}, \rho_{\downarrow}]}{\delta \rho_{\sigma}} - V_H[\rho_{\alpha\sigma}](\mathbf{r}) - V_{xc,\sigma}^{LSD}[\rho_{\alpha\sigma}](\mathbf{r}). \quad (3.9)$$

The special feature of the SIC is the dependence of the potential on the individual orbital densities which makes the orbitals to be non-orthogonal. The orthonormal KS orbitals are replaced by orbitals which minimize the self-interaction corrected energy functional. Varying (3.8) with respect to the orbital spin densities with the constraint that SIC orbitals form a set of orthonormal functions leads to the SIC eigenvalue equations

$$(H^{LDA} + V_{\alpha}^{SIC}) | \phi_{\alpha} \rangle = \sum_{\alpha'} \lambda_{\alpha\alpha'} | \phi_{\alpha'} \rangle \quad (3.10)$$

with the localization condition

$$\langle \phi_{\alpha} | V_{\alpha}^{SIC} - V_{\beta}^{SIC} | \phi_{\beta} \rangle = 0. \quad (3.11)$$

The localization condition ensures the stability of the SIC energy functional with respect to infinitesimal unitarian mixing of the orbitals [21].

Self-interaction is significant for localized states and it tends to zero for extended states since in the latter case the Coulomb interaction of an electron with itself is of order $1/N$. For more itinerant systems SIC does not give localized solutions, and it then reduces to the LDA. Accordingly, the application to semiconductors, e.g. Si, does not increase the fundamental LDA gap [22]. The self interaction correction has been applied to d - and f -electron systems in different methods [23–26].

A simplified version of SIC approximation based on multiple scattering theory implements the SI correction locally [26]. All one-particle properties including the charge density can be calculated from the single-particle Green's function,

$$\rho_\sigma = -\frac{1}{\pi} \int_{E_B}^{E_F} dE \Im G_{LL,\sigma}(\mathbf{r}, \mathbf{r}; E), \quad (3.12)$$

where ρ_σ is the total valence charge density per spin σ . E_B and E_F denote the bottom of valence band and the Fermi energy, respectively. From this density the effective potential is calculated for the next iteration of the self-consistency cycle.

Within KKR method the degree of localization is determined by the Wigner delay time, that is the energy derivative of the single-site phase shift [27]

$$\tau_W = \frac{d\delta_l(E)}{dE}, \quad (3.13)$$

which for localized valence states is large. For a localized state, in a spherically symmetric potential, characterized by quantum number n , angular momentum L and spin σ the charge density is

$$\rho_{nL\sigma}^{SIC} = -\frac{1}{\pi} \int_{E_1}^{E_2} dE \Im G_{LL,\sigma}(\mathbf{r}, \mathbf{r}; E). \quad (3.14)$$

Here, E_1 and E_2 lie slightly below and above the energy of the state $nL\sigma$. The charge density is used to construct the effective self-interaction free potential for site i as

$$V_{eff,iL\sigma}^{LSD-SIC} = V_{eff,\sigma}^{LSD}(\mathbf{r}) + V^{SIC} \quad (3.15)$$

and

$$V^{SIC} = -V_H[\rho_{iL\sigma}^{SIC}](\mathbf{r}) - V_{xc}^{LSD}[\rho_{iL\sigma}^{SIC}, 0](\mathbf{r}). \quad (3.16)$$

For each self-interaction corrected channel, labeled by $\tilde{L}\tilde{\sigma}$, the \tilde{L} element of the t -matrix calculated from the LSD potential is replaced by the one obtained from the SI-corrected potential,

$$\tilde{t}_{L\sigma}^i = t_{L\sigma}^i (1 - \delta_{L,\tilde{L}} \delta_{\sigma,\tilde{\sigma}}) + t_{\tilde{L}\sigma}^{i,LSD-SIC} \delta_{L,\tilde{L}} \delta_{\sigma,\tilde{\sigma}}. \quad (3.17)$$

The new t -matrix \tilde{t} is used to calculate the SI-corrected scattering path operator.

In the local self-interaction correction (LSIC) method the localization condition (3.11) is not applied and the energy minimization of the total energy determines the best configuration. The total energies are invariant under a rotation of the coordinate system owing to symmetry adapted spherical harmonics.

3.4 Transition state approximation

In the calculation of ground-state properties, e. g. magnetic ordering and local magnetic moments, the SI correction is applied with full strength. For excited states, it appears

that the binding energies of the SI-corrected localized levels are significantly too large when compared to those determined from spectroscopical data, i. e. from photoemission intensities. This ‘overcorrection’ of the SIC is attributed to the orbital relaxation.

The density-functional theory of Hohenberg, Kohn, and Sham applies only if the occupation number of the orbitals are either zero or one. If the occupancy of one of the single-particle states has been changed, one has to generalize the theory by including the occupation number, as was done by Janak [28]. According to Janak’s theorem, the derivative of the total energy with respect to the orbital occupation equals the eigenenergy of the corresponding orbital,

$$\frac{\partial E}{\partial f_\alpha} = \langle \psi_\alpha | H^{\text{LSD}} | \psi_\alpha \rangle = \epsilon_\alpha, \quad (3.18)$$

where H^{LSD} is the LSD Hamiltonian and f_α is the occupation number of the orbital ψ_α , and

$$\sum_{\alpha}^{\text{occ}} f_\alpha = N. \quad (3.19)$$

The removal energy can be calculated by removing an electron from an occupied state,

$$\Delta E_{\text{relaxed}} = - \int_0^1 df_\alpha \epsilon_\alpha(f_\alpha). \quad (3.20)$$

To evaluate the above integrals the eigenvalues of relaxed orbitals must be calculated. Several ways to calculate the removal energy have been proposed [29] but they lead to unphysical effects [30]. In Slater’s transition state approximation (STSA) [31] one calculates $\epsilon_\alpha(f_\alpha)$ only at the midpoint rather than calculating function inside the integral for all values between 0 and 1.

I start from the Taylor expansion of the eigenvalue as a function of the occupation number in the neighborhood of F_α ,

$$\epsilon_\alpha(f_\alpha) = \epsilon(F_\alpha) + (f_\alpha - F_\alpha) \left(\frac{\partial \epsilon}{\partial f_\alpha} \right)_{f_\alpha=F_\alpha}. \quad (3.21)$$

The restriction to the first order is justified if the eigenvalue depends almost linearly on its occupation number [32, 33]. Inserting (3.21) into (3.20) and integration from $f_\alpha = 1$ to $f_\alpha = 1 - p$ gives

$$E(f_\alpha = 1 - p) - E(f_\alpha = 1) = -p\epsilon_\alpha(F_\alpha) + \left[\frac{p^2}{2} - p(1 - F_\alpha) \right] \left(\frac{\partial \epsilon_\alpha}{\partial f_\alpha} \right)_{f_\alpha=F_\alpha}. \quad (3.22)$$

To have a method similar to Koopmans’ theorem one would need the eigenvalues at full occupancy. For $F_\alpha = 1$ and $p = 1$,

$$\Delta E_{\text{relaxed}} = -\epsilon_\alpha(1) + \frac{1}{2} \left(\frac{\partial \epsilon_\alpha}{\partial f_\alpha} \right)_{f_\alpha=1}. \quad (3.23)$$

The first term is the energy of the fully occupied orbital α . The second term accounts for the orbitals relaxation. This term includes a ‘non-Koopmans’-like correction (relaxation of the localized state) and the relaxation energy (relaxation of the other orbitals). In many applications to localized states, the orbitals relaxation is significant. To achieve an accurate electron removal energy, the second term of (3.23) has to be included in the energy calculation. Using the Hellmann-Feynman theorem [16], the second term on the right-hand side of (3.23) can be written as

$$\frac{\partial \epsilon_\alpha}{\partial f_\alpha} = \left\langle \psi_\alpha \left| \frac{\partial H^{\text{LSD}}}{\partial f_\alpha} \right| \psi_\alpha \right\rangle. \quad (3.24)$$

If the relaxation of other orbitals is neglected (in analogy to Koopmans’ theorem), then (3.24) reduces to

$$\frac{\partial \epsilon_\alpha}{\partial f_\alpha} = \left\langle \psi_\alpha \left| u_\alpha + \rho_\alpha \frac{\partial \epsilon_{\text{xc}}}{\partial \rho} \right| \psi_\alpha \right\rangle, \quad (3.25)$$

where u_α is the Coulomb potential associated with orbital α . For $f_\alpha = 1$, the first term is the self-Coulomb interaction of an electron. The second term is the change of the exchange-correlation energy (to first order in the occupation number) of the system due to the removing one electron from the orbital α . (3.25) can be interpreted as the self-interaction of an orbital whose occupation number is reduced. Adding this positive term to the energy of the orbital α increases the removal energy calculated within LSD. Thus, the removal energy of a localized orbital with corrected potential V_α becomes

$$\Delta E_{\text{unrelaxed}} = - \langle \psi_\alpha | H^{\text{LSD}} | \psi_\alpha \rangle - \frac{1}{2} \langle \psi_\alpha | V_\alpha^{\text{SIC}} | \psi_\alpha \rangle. \quad (3.26)$$

This is the unrelaxed removal energy when an electron is removed from orbital α . The removal energy is larger than its experimental counterpart because the relaxation of other orbitals is neglected.

As is apparent from (3.26), the removal energy of the orbital α is calculated with half strength of the SIC potential associated with this orbital. By this method, i. e. by calculating the LSD and the SIC ground-state potentials, one obtains removal energies with good accuracy [25, 30]. Following previous works we call this approach transition-state approximation (TSA).

Chapter 4

A brief review of methods

4.1 Multiple scattering theory

Multiple scattering theory (MST) is a technique which can be used to solve a linear partial differential equation, e.g. the Schrödinger equation

$$[-\nabla^2 + V(\mathbf{r})]\psi(\mathbf{r}) = E\psi(\mathbf{r})^1, \quad (4.1)$$

over a region which is divided into nonoverlapping subregions, e.g. individual potentials V_i such that the domains of these potentials are disjoint,

$$V(\mathbf{r}) = \sum_{i=1}^N V_i(\mathbf{r}_i), \quad \mathbf{r}_i = \mathbf{r} - \mathbf{R}_i, \quad D_{V_i} \cap D_{V_j} = \begin{cases} \emptyset & i \neq j \\ D_{V_i} & i = j \end{cases}.$$

The main task of MST is to obtain the properties of a system of scatterers by solving the single-particle Schrödinger equation (4.1) for each scatterer. For a spherically symmetric potential, e.g. a muffin-tin potential [34], the solution of the Schrödinger equation (4.1) is considerably simplified. In spherical coordinates, the Hamiltonian can be written as

$$H = -\frac{1}{r^2} \frac{\partial}{\partial r} (r^2 \frac{\partial}{\partial r}) + \frac{L^2}{r^2} + V(\mathbf{r}), \quad (4.2)$$

where \mathbf{L} is the angular momentum operator and

$$L^2 = -\left[\frac{1}{\sin \theta} \frac{\partial}{\partial \theta} (\sin \theta \frac{\partial}{\partial \theta}) + \frac{1}{\sin \theta} \frac{\partial^2}{\partial \phi^2} \right]. \quad (4.3)$$

H , L^2 , and L_z have common eigenfunctions and the solutions of the Schrödinger equation (4.1) can be written in the form

$$\psi(\mathbf{r}) = \sum_{lm} c_{lm} R_l(\mathbf{r}) Y_{lm}(\hat{\mathbf{r}}), \quad \hat{\mathbf{r}} = \frac{\mathbf{r}}{|\mathbf{r}|}, \quad (4.4)$$

¹In the following we use Rydberg atomic units, $\hbar = 1$ and $2m = 1$.

where c_{lm} are expansion coefficients. The spherical harmonics $Y_{lm}(\hat{\mathbf{r}})$ are the eigenfunctions of L^2 and L_z such that

$$L^2 Y_{lm}(\hat{\mathbf{r}}) = l(l+1) Y_{lm}(\hat{\mathbf{r}}) \quad (4.5)$$

and

$$L_z Y_{lm}(\hat{\mathbf{r}}) = m Y_{lm}(\hat{\mathbf{r}}). \quad (4.6)$$

Here l and m are orbital angular momentum and azimuthal quantum numbers, respectively. The radial amplitudes $R_l(\mathbf{r})$ satisfy the radial Schrödinger equation

$$\left[\frac{1}{2} \left(-\frac{1}{r^2} \frac{d}{dr} \left(r^2 \frac{d}{dr} \right) + \frac{l(l+1)}{r^2} \right) + V(\mathbf{r}) - k^2 \right] R_l(k, r) = 0 \quad (4.7)$$

and can be characterized as ‘regular solutions’ which vanish at the origin and ‘irregular solutions’ which diverge at the origin.

For the case in which the potential $V(\mathbf{r})$ vanishes, the ‘general solutions’ contain regular solutions, which are finite in the limit $r \rightarrow 0$ and can be written in terms of spherical Bessel function j_l , and irregular solutions, which diverge for $r \rightarrow 0$ and can be written in terms of spherical Neumann functions n_l . For large r , the centrifugal term $l(l+1)/r^2$ vanishes and solutions behave asymptotically as plane waves. By linear combination of regular and irregular solutions, the required asymptotical behavior can be obtained (in terms of spherical Hankel functions h_l^\pm).

For a nonvanishing potential it is convenient to match the solutions inside the sphere to those outside the sphere. The phase shifts δ_l can be calculated by matching the general solutions for outside the range of the potential (or $V = 0$) with the regular radial amplitudes R_l at the muffin-tin boundary

$$\tan \delta_l(E) = \frac{L_l(E, r) j_l(kr) - j'_l(kr)}{L_l(E, r) n_l(kr) - n'_l(kr)}, \quad (4.8)$$

where L_l is the logarithmic derivative of the radial amplitudes R_l at the sphere boundary.

The phase shifts play an important role in single-site scattering. The derivative of the phase shift with respect to the energy is proportional to the Wigner delay time [27], the time by which the scattered wave is delayed with respect to the incident wave. Having the obtained phase shift, one can calculate the single-site ‘transition matrix’, or t -matrix, [35, 36]

$$t_l(E) = -k^{-1} \sin \delta_l(E) \exp(i\delta_l(E)). \quad (4.9)$$

The t -matrix is a central quantity in MST. All the building blocks of MST, such as scattering path operator, structure constant, and scattering solutions, are achieved from t -matrices.

4.1.1 The Green's function in MST

Any representation of a resolvent is called a Green's function. The resolvent of a time-independent, linear, hermitian differential operator H (Hamiltonian) is defined formally by

$$G(z) = (zI - H)^{-1}, \quad (4.10)$$

where z is a complex variable with $Re\{z\} \equiv E$ and $Im\{z\} \equiv s$.

The Green's function of a perturbed system can be written as a series that corrects the Green's function of the unperturbed system. This can be done by the Dyson equation which connects a non-interacting system with Hamiltonian H_0 to an interacting system with Hamiltonian $H = H_0 + V$. If $G_0(z)$ and $G(z)$ are the resolvent of H_0 and H , $G(z)$ can be expressed in terms of $G_0(z)$ and V

$$G(z) = G_0(z)[1 + VG(z)]. \quad (4.11)$$

By defining the T -operator as

$$T(z) = V(z) + V(z)G(z)V(z), \quad (4.12)$$

$G(z)$ can be written as

$$G(z) = G_0(z) + G_0(z)T(z)G_0(z). \quad (4.13)$$

For an ensemble of N scatterers, the effective potential V can be seen as the sum of individual effective potentials which their domains being disjoint in space. The T -operator (4.12) can be written in terms of scattering path operators [37]

$$T = \sum_{nm} \tau^{nm}, \quad (4.14)$$

where

$$\tau^{nm} = t^n \delta_{nm} + t^n G_0 \sum_{k \neq n} \tau^{km}. \quad (4.15)$$

The t -matrix t^n and the Green's function G_0 describe the scattering from the potential on the scattering centers n and the free propagation between the scattering centers, respectively.

The Green's function $G(\mathbf{r}, \mathbf{r}'; E)$ when \mathbf{r} and \mathbf{r}' are near some site n can be expressed as

$$G = G^n + G^n T_{nn} G^n, \quad (4.16)$$

where the single-site Green's function

$$G^n = G_0 + G_0 t^n G_0 \quad (4.17)$$

describes the propagation of an electron in the field of the potential of the site n and

$$T_{nn} = \sum_{i \neq n} \sum_{j \neq n} \tau^{ij} \quad (4.18)$$

sums all scattering events which neither begin nor end on the site n . Inserting (4.17) and (4.18) into (4.16) leads to the expression

$$\begin{aligned} G(\mathbf{r}_n + \mathbf{R}_n, \mathbf{r}'_n + \mathbf{R}_n; E) &= \sum_{LL'} Z_L^n(\mathbf{r}_n; E) \tau_{LL'}^{nn} Z_{L'}^n(\mathbf{r}'_n; E) \\ &- \sum_L Z_L^n(\mathbf{r}_{<}; E) \tilde{J}_L^n(\mathbf{r}_{>}; E). \end{aligned} \quad (4.19)$$

The elements of $\tau_{LL'}^{nn}$ are obtained from

$$\tau_{LL'}^{nm} = \left([t_{LL'}^n]^{-1} \delta_{nm} - G_{0,LL'}^{nm} \right)^{-1}, \quad (4.20)$$

where $G_{0,LL'}^{nm}$ indicates the structure constant [38]. The scattering solutions Z and \tilde{J} are the solutions of the Schrödinger equation for a external field at site n . The main properties Z and \tilde{J} are listed in Table 4.1.1.

If \mathbf{r} and \mathbf{r}' refer to different origins, i. e. $\mathbf{r} = \mathbf{r}_n + \mathbf{R}_n$ and $\mathbf{r}' = \mathbf{r}_m + \mathbf{R}_m$, the Green's function can be expressed as [39]

$$G(\mathbf{r}_n + \mathbf{R}_n, \mathbf{r}_m + \mathbf{R}_m; E) = \sum_{LL'} Z_L^n(\mathbf{r}_n; E) \tau_{LL'}^{nm}(E) Z_{L'}^m(\mathbf{r}_m; E). \quad (4.21)$$

In principle all one-particle properties, such as charge and magnetization density, can be directly obtained from G . The expectation value of a one-particle operator A can be expressed as

$$A_{ab} = \mp \frac{1}{\pi} \int_{E_a}^{E_b} dE \text{Tr} [\Im(A G^\pm(\mathbf{r}, \mathbf{r}; E))]. \quad (4.22)$$

where $G^\pm(\mathbf{r}, \mathbf{r}'; E)$ are side limits of the Green's function G .

If the Hamiltonian is translational invariant, a lattice Fourier transformation of $\tau_{LL'}^{nm}(E)$ can be formed. The equation of motion for the scattering path operator in momentum space is then

$$\tau_{LL'}^{nm}(\mathbf{k}, E) = \left[(t_{LL'}^n(E))^{-1} \delta_{nm} - G_{0,LL'}^{nm}(\mathbf{k}, E) \right]^{-1}. \quad (4.23)$$

This is the KKR equation which is in particular important since it allows to obtain the electronic structure. It implies that whenever the KKR determinant vanishes the corresponding scattering path operator has a singularity [35, 36, 38].

4.2 Layer KKR

For a system with reduced symmetry the three dimensional wave vector \mathbf{k} is not a good quantum number. Therefore the 3D Fourier transform of the equation of motion cannot be applied anymore. In layer KKR a solid is partitioned into layers of atoms and these layers are divided into three regions: an interface region and two bulk regions on both sides of the interface region. The main task of layer KKR is to determine the scattering properties of the whole solid. This is achieved by constructive calculation of the scattering properties of a single site (an atom for example), a single layer, stacks of layers and eventually the entire solid. In this method a mixed basis set of partial waves, like in the conventional KKR method, and plane waves, between layers of atoms, are used. Theories of low-energy electron diffraction and photoemission also use these approach.

The central equation of layer KKR is (4.19) which can be written as

$$G(\mathbf{r}_i, \mathbf{r}'_j; E) = \sum_{LL'} J_L^\alpha(\mathbf{r}; E) \Gamma_{LL'}^\alpha J_{L'}^\alpha(\mathbf{r}'; E) - \sum_L J_L^\alpha(\mathbf{r}_{<}; E) H_L^\alpha(\mathbf{r}_{>}; E). \quad (4.24)$$

The main properties of H and J are listed in Table 4.1.1. The scattering paths $\Gamma_{LL'}$ are separated into interlayer and intralayer scattering events and can be expressed as

$$\Gamma_{LL'} = \left[(t^\alpha)^{-1} \left[\frac{1}{\Omega} \int_{\Omega} dk^2 \tau_i^{\alpha\alpha}(\mathbf{k}) - t^\alpha \right] (t^\alpha)^{-1} \right]_{LL'}. \quad (4.25)$$

Boundary condition determines $\Gamma_{LL'}$: The Bloch condition parallel to the layers determines the interlayer scattering path, and correct reflection at both sides of the interface layer determines the interlayer scattering path. The elements needed to calculate Γ are as following [40]:

- (i) the scattering from an isolated atom, t^α , cf. (4.9),
- (ii) the scattering within an isolated layer which is 2D Fourier transform of (4.20),

$$T_i(\mathbf{k}, E) = (t^{-1}(E) - g(\mathbf{k}, E))^{-1}, \quad (4.26)$$

Table 4.1: Properties of scattering solutions

Function	Behavior for $r \rightarrow 0$	Asymptotic for $r \rightarrow \infty$
$ Z\rangle$	regular	$ j\rangle t^{-1} + h\rangle$
$ \tilde{J}\rangle$	irregular	$ j\rangle$
$ J\rangle$	regular	$ j\rangle + h\rangle t$
$ H\rangle$	irregular	$ h\rangle$

where g is the 2D Bloch Green's function,

(iii) the scattering path operator which sums all scattering paths which end with a scattering event within layer i ,

$$[\tau_i^{\alpha\alpha}(k)]_{LL'} = \left[T_i(\mathbf{k}) R_i^{eff} T_i(\mathbf{k}) + T_i(\mathbf{k}) \right]_{LL'}^{\alpha}, \quad (4.27)$$

where effective reflection, R_i^{eff} describes the back scattering by all layers excluding layer i .

4.3 Coherent potential approximation

In a disordered system the configurationally averaged matrix elements of a hermitian operator can be calculated in a simple way by calculating the configurationally averaged Green's function, $\langle G^+(\mathbf{r}, \mathbf{r}'; E) \rangle$. The configuration average of the Green's function can be written as [38]

$$\langle G(z) \rangle = \left\langle \frac{1}{z - H} \right\rangle = \frac{1}{z - H_0 - \Sigma(z)}, \quad (4.28)$$

where $H = H_0 + V$ and $\Sigma(z)$ being the (translationally invariant) electron self-energy operator. H can be written as

$$H = \underbrace{H_0 + W(z)}_{H'(z)} + \underbrace{V - W(z)}_{V'(z)}, \quad (4.29)$$

where W is the superposition of (translationally invariant) energy-dependent site quantities W_i . The resolvent $G(z)$ and the self-energy $\Sigma(z)$ can be written in terms of $G' = [z - H']^{-1}$ (which is translationally invariant and no longer configuration dependent)

$$\langle G(z) \rangle = [1 + G' \langle T(z) \rangle] G'(z), \quad (4.30)$$

$$\Sigma(z) = W(z) + \langle T(z) \rangle [1 + G'(z) \langle T(z) \rangle]^{-1}, \quad (4.31)$$

$$(4.32)$$

where $T(z)$ denotes the perturbation caused by $V'(z)$,

$$T(z) = V'(z) + V'(z) G'(z) V'(z). \quad (4.33)$$

For a chosen medium $W(z)$ the configurational averaged Green's function $G(z; W(z))$ equals the translationally invariant Green's function $G'(z; W(z))$ if and only if $\langle T(z) \rangle = 0$. This is the so-called coherent potential approximation (CPA) condition. It states that the configurational averaged Green's function can be replaced by that of an effective medium $W(z)$ if on the average there is no additional scattering due to $W(z)$. Since $V'(z)$ is a superposition of site dependent quantities, a multiple scattering expansion can be applied.

4.3.1 Single-site KKR-CPA

The total T -operator can be written in terms of single-site T -operators

$$T(z) = \sum_i Q_i(z), \quad (4.34)$$

$$Q_i(z) = t_i(z) + t_i(z)G'(z) \sum_{j \neq i} Q_j(z). \quad (4.35)$$

The average of T -matrix, $\langle T(z) \rangle$, is therefore given by

$$\langle T(z) \rangle = \sum_i \langle Q_i(z) \rangle. \quad (4.36)$$

Keeping only the single-site quantities (omitting thus fluctuation terms) leads to the single-site approximation for the configuration average

$$\langle Q_i(z) \rangle = \langle t_i(z) \rangle [1 + G'(z) \sum_{j \neq i} \langle Q_j(z) \rangle]. \quad (4.37)$$

Within the single-site approximation for a given periodic complex function $W(z)$ the CPA condition is reduced to $\langle t_i(z; W(z)) \rangle = 0$.

Suppose a medium consists of a system with a coherent t -matrix t_c on each site. The additional scattering that occurs when an impurity atoms with t -matrix t_A is introduced into the lattice (at the origin) can be calculated as

$$\tau_\alpha^{00} = D_\alpha^{00} \tau_c^{00}, \quad (4.38)$$

where

$$D_A^{00}(E) = [1 - \tau_c^{00}(E)(t_c^{-1}(E)) - t_A^{-1}(E)]^{-1}, \quad (4.39)$$

and

$$\tau_c^{00}(E) = \frac{1}{\Omega_{BZ}} \int d\mathbf{k} [t_c^{-1}(E) - G(\mathbf{k}, (E))]^{-1}. \quad (4.40)$$

The CPA condition for obtaining the coherent medium implies that the additional scattering due to replacing t_c at the origin by t_A should vanish. Therefore for an alloy with n components with concentrations c_α , the CPA condition is given by

$$\sum_{\alpha=A,B,\dots} c_\alpha \tau_\alpha^{00} = \tau_c^{00} \quad (4.41)$$

or

$$\sum_{\alpha=A,B,\dots} c_\alpha D_\alpha^{00} = 1. \quad (4.42)$$

In KKR-CPA calculations the single-site t -matrix for the coherent lattice is only a guess, therefore the KKR-CPA equations have to be solved self-consistently.

Site-diagonal properties. After solving the KKR-CPA equations the electronic structure of a site occupied by a particular type of atom can be calculated from the Green's function generated from the scattering path operator calculated for that type of atom. The density of states can be calculated as

$$\rho(E) = \frac{1}{\Omega_{BZ}} \int d\mathbf{k} A_B(\mathbf{k}, E), \quad (4.43)$$

where A_B is the Bloch spectral function, which is the trace over the imaginary part of the k -projection of the Green's function,

$$A_B(\mathbf{k}, E) = -\frac{1}{\pi} \Im[Tr G^+(\mathbf{k}, E)]. \quad (4.44)$$

For real energies the second term of (4.21) is real and the density of states of a disordered system reads

$$\rho^i(E) = -\frac{1}{\pi} \sum_{\alpha=A,B,\dots} c_\alpha \Im[Tr[D_\alpha^{ii}(E)\tau_c^{ii}(E)F^{i\alpha,i\alpha}(E)]], \quad (4.45)$$

$$F_{LL'}^{i\alpha,i\alpha} = \int dr Z_L^i(\mathbf{r}_i; E)Z_{L'}^i(\mathbf{r}_i; E), \quad (4.46)$$

where the indices $i\alpha$ mean that site i is occupied by α .

Non-site-diagonal properties. In a binary alloy sites i and j may be occupied by species A or B . Then the average for a non-site diagonal Green's function can be written in terms of non-site-diagonal scattering path operator, $\langle \tau^{ij}(E) \rangle_{i\alpha,j\beta} = D_\alpha^{ii}\tau_c^{ij}D_\beta^{jj}$. After some mathematics the Bloch spectral function can be written as [36]

$$\begin{aligned} A_B(\mathbf{k}, E) &= -\frac{1}{\pi} \left(\sum_{\alpha=A,B} c_\alpha \Im[Tr(D_\alpha^{ii}(E)\tau_c^{ii}(E)F^{i\alpha,i\alpha}(E))] \right. \\ &\quad \left. + \sum_{\alpha,\beta=A,B} c_\alpha c_\beta \Im[Tr(D_\alpha^{ii}(E)\bar{\tau}(\mathbf{k}, E)D_\beta^{ii}(E)F^{i\alpha,i\beta}(E))] \right) \end{aligned} \quad (4.47)$$

where $\bar{\tau}(\mathbf{k}, E) = \tau_c(\mathbf{k}, E) - \tau_c^{ii}(E)$ and $\tau_c(\mathbf{k}, E) = [t_c^{-1}(E) - G(\mathbf{k}, E)]^{-1}$

Chapter 5

Selected results

This chapter is devoted to the selected results. The first part of this chapter gives a summary of the selected publications which are categorized in two groups. The second part of this chapter consists of six selected papers.

5.1 Systematic study

Model calculations determine the influential parameters in the Rashba systems as atomic spin-orbit splitting, in-plane potential gradient, and out-of-plane potential gradient [7, 14]. Experimental results add another parameter to the abovementioned: the relaxation of the atoms of the surface layer which determines the contribution of different p orbitals [4].

In **paper I**, the atomic contribution to the Rashba spin-orbit splitting is examined. The structural parameters of Sb/Ag(111) are very close to those of the Bi/Ag(111) and Pb/Ag(111) systems, see figure 5.1. The Sb adatoms replace every third Ag atom in the topmost layer to form a surface alloy with a $\sqrt{3} \times \sqrt{3} - R30^\circ$ surface geometry with nominal SbAg_2 stoichiometry.

Figure 5.2 shows the ARPES intensity maps and the calculated spectral densities for the SbAg_2 alloy along the high-symmetry directions of the two-dimensional Brillouin zone. By analogy with the isostructural PbAg_2 and BiAg_2 alloys, we attribute the lower band to states of mainly sp_z . The upper band has mainly $p_x p_y$ character. The spin polarization of these surface states is mainly in plane and normal to the wave vector. The dispersion of the calculated bands follows nicely the experimental data.

Interestingly, the outcome of the KKR calculations in terms of orbital hybridization indicates a similar admixture of $p_x p_y$ character in the sp_z bands for both the Sb/Ag and the Bi/Ag systems. This is a key point as it shows that the sensitivity to the in-plane gradient should be about the same in both systems. Therefore, the smaller splitting in Sb/Ag(111) compared to Bi/Ag(111) is mainly due to the smaller atomic spin-orbit interaction.

The main achievement of **paper I** is the following scenario: for a sizable splitting,

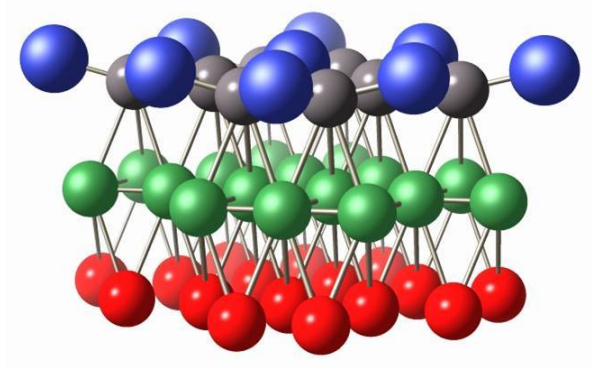


Figure 5.1: Side view of the $\sqrt{3} \times \sqrt{3} - R30^\circ$ structure of ordered surface alloys on Ag(111). Sb (Bi or Pb) atoms are shown in blue, illustrating the outward relaxation of Sb in the surface layer. Ag atoms of the first, second and third layer are shown in gray, green and red, respectively.

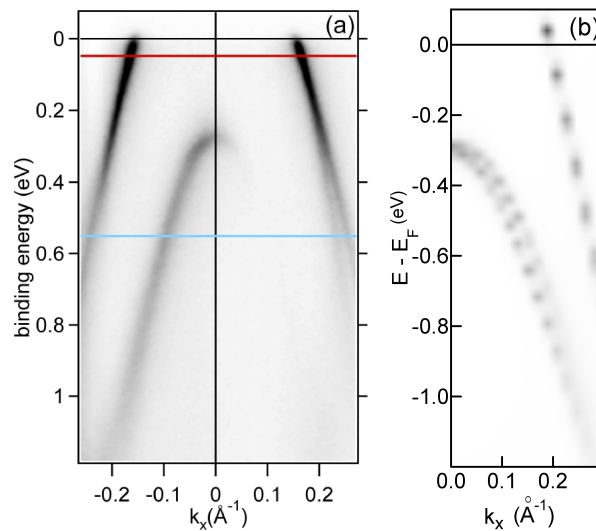


Figure 5.2: (a): ARPES intensity maps of the SbAg_2 surface alloy, measured around the $\bar{\Gamma}$ point along the $\bar{\Gamma} - \bar{K}$ direction of the two-dimensional Brillouin zone. (b): The calculated total spectral density along the $\bar{\Gamma} - \bar{K}$ direction.

a strong atomic contribution is inevitable. An additional mechanism here, the in-plane gradient can increase the splitting, as seen for Bi/Ag(111) and Pb/Ag(111). However, such mechanism can only ‘trigger’ the effect. Without a strong atomic contribution, the splitting is small, as proven in the present work on Sb/Ag(111). On the other hand, the band splitting is not simply proportional to the relevant atomic spin-orbit parameter.

The main goal of **paper II** is to examine the possibility of tuning the Rashba characteristics of the surface alloys on Ag(111). In **paper II**, we complete the picture of the disordered binary alloys by investigating the $\text{Bi}_x\text{Sb}_{1-x}/\text{Ag}(111)$ and $\text{Pb}_x\text{Sb}_{1-x}/\text{Ag}(111)$ systems. Then we extend our calculations to ternary alloys and show the possibility of independently tuning of the Rashba characteristics. Part of our results is supported by recent experimental findings.

The ordered surface alloys Bi/Ag(111), Pb/Ag(111), and Sb/Ag(111), which have been investigated by first-principles calculations and in experiments, differ with respect to their Rashba characteristics k_R , E_R , and E_0 (cf. figure 5.3). The challenge is how to tune these properties. One possible way is to mix these three systems to achieve a surface alloy with desirable properties. The idea of **paper II** is as follows. Bi/Ag(111) has a large splitting and occupied sp_z surface states, while Pb/Ag(111) has a large splitting and unoccupied sp_z surface states. In a disordered binary alloy $\text{Bi}_x\text{Pb}_{1-x}/\text{Ag}(111)$ the Fermi energy can be tuned by the concentration x , while keeping a large spin splitting. In contrast, Sb/Ag(111) has occupied surface states with almost the same binding energy as those in Bi/Ag(111) but a minor splitting. This allows to tune mainly the spin splitting but keeping the Fermi energy in $\text{Bi}_x\text{Sb}_{1-x}/\text{Ag}(111)$. Thus, by an appropriate choice of concentrations x and y in a ternary alloy $\text{Bi}_x\text{Pb}_y\text{Sb}_{1-x-y}/\text{Ag}(111)$ we expect to tune the Fermi energy and the splitting independently.

In **paper II**, first we consider the properties of the disordered binary alloys. The following paragraphs mention the main results.

In the disordered binary alloy $\text{Bi}_x\text{Pb}_{1-x}/\text{Ag}(111)$ the ratio of the Rashba energy E_R and the Fermi energy E_F can be chosen within a wide range, in dependence on the Bi concentration x [41]. Pb has one valence electron less than Bi, which explains the sizable shift of the surface states to higher energies (cf. the panels on the right-hand side of figure 5.4). Although the relaxation is of the same order, the splitting is smaller for Pb.

Recently, the surface states of the disordered binary alloys $\text{Bi}_x\text{Sb}_{1-x}/\text{Ag}(111)$ were mapped out by angle-resolved photoelectron spectroscopy. The momentum offset k_R evolves continuously with increasing Bi concentration x . The splitting decreases sizably for $x < 0.50$ [42]. In theory, the outward relaxation of Bi is larger than for Sb (15% and 9.6%, respectively). Consequently the charge which is removed from the Sb muffin-tin sphere (0.94%) is smaller than that of Bi (0.99%). Since Bi and Sb are iso-electronic, with valence-shell configuration $5p^3$ and $6p^3$, E_0 remains almost unaffected by x , as can be seen in the bottom row of figure 5.4. The spin splitting for Sb is much less than for Bi, in agreement with the atomic spin-orbit parameter (0.4 eV and 1.25 eV).

To complete the picture of the binary alloys we turn to $\text{Pb}_y\text{Sb}_{1-y}/\text{Ag}(111)$, for which experimental results are not available. As the Pb concentration increases, E_0 shifts

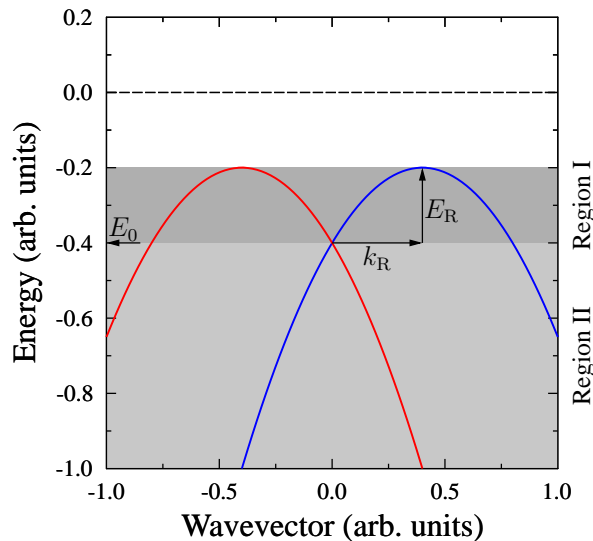


Figure 5.3: Schematic dispersion of Rashba-split surface states in a surface alloy, with negative effective mass m^* . E_0 , k_R , and E_R denote the crossing point of the bands at $k_{\parallel} = 0$, the splitting, and the Rashba energy, respectively. The spin orientation is indicated by the bands' colors (blue, red). The grey areas highlight the regions I (dark grey) and II (light grey).

down from $E_F + 0.6$ eV to $E_F - 0.4$ eV, implying that the surface states become completely filled at about $y = 0.3$ (cf. the panels on the left-hand side of figure 5.4). As for $\text{Bi}_x\text{Sb}_{1-x}/\text{Ag}(111)$, the spin splitting increases with y .

Our investigation of the disordered binary surface alloys, given in the first part of **paper II**, suggests three underlying mechanisms which influence the splitting of the surface states.

A first mechanism is relaxation. The outward relaxations of Sb, Pb, and Bi are in accord with their atomic radii; the larger the atomic radius, the larger the outward relaxation. The relaxation is accompanied by a charge transfer from the atomic sphere to the surrounding: the larger the relaxation, the larger the charge transfer [43]. This mechanism determines the energy position of the degenerate point E_0 and, consequently, the Fermi energy or band-filling of the surface states (2DEG).

A second mechanism is the atomic spin-orbit parameter. Bi and Pb are heavy elements with large SO parameter (1.25 eV for Bi and 0.91 eV for Pb [44]), in contrast to the lighter element Sb (0.4 eV [44]). The Rashba splitting depends both on the atomic SO-coupling strength and the potential gradient [14]. Since the latter should not differ considerably among the considered systems, the spin splitting is mainly determined by the atomic SO coupling.

A third mechanism is electron doping or band filling. Pb has one electron less than Bi ($Z_{\text{Pb}} = 82$, $Z_{\text{Bi}} = 83$). Within a rigid-band model, the surface states in Pb/Ag(111) are shifted to higher energies, as compared to those in Bi/Ag(111). This picture is confirmed

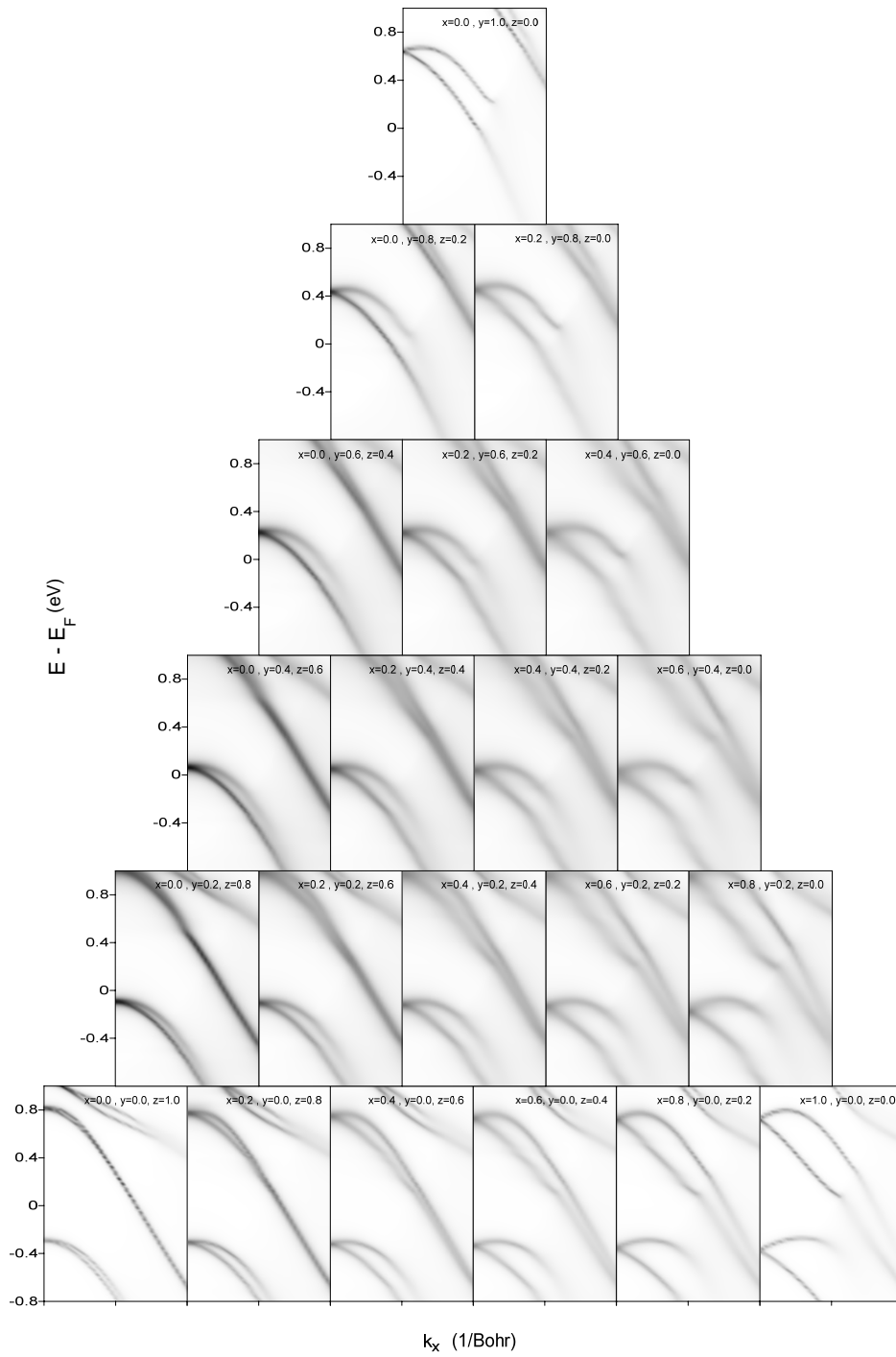


Figure 5.4: Surface states of disordered ternary alloys $\text{Bi}_x\text{Pb}_y\text{Sb}_{1-x-y}/\text{Ag}(111)$ along $\bar{\Gamma}-\bar{K}$ of the two-dimensional Brillouin zone. The spectral density at a heavy-element site $\text{Bi}_x\text{Pb}_y\text{Sb}_{1-x-y}$ is depicted as linear gray scale, with dark gray corresponding to high spectral weight.

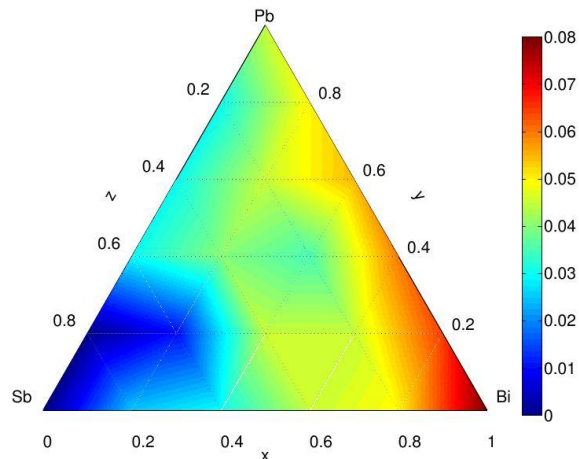


Figure 5.5: Spin splitting in disordered ternary alloys $\text{Bi}_x\text{Pb}_y\text{Sb}_{1-x-y}/\text{Ag}(111)$. The surface-state displacement k_R (in reciprocal space) is depicted as color scale as a function of Bi concentration x , Pb concentration y , and Sb concentration $z = 1 - x - y$. The color bar on the right is in units of \AA^{-1} .

by experiments and first-principles calculations [41].

Having established the ingredients which are necessary for independently tuning the Fermi energy and the spin splitting in the surface alloys, we now mix them to disordered ternary alloys $\text{Bi}_x\text{Pb}_y\text{Sb}_{1-x-y}/\text{Ag}(111)$.

In figure 5.4 the surface-state dispersions of ternary alloys $\text{Bi}_x\text{Pb}_y\text{Sb}_{1-x-y}/\text{Ag}(111)$ are shown. The Rashba characteristic of the ternary alloys follow the general trends of the binary alloys which have been discussed before. In the ternary alloys with larger outward relaxation (i. e. the Bi- and Pb-rich compounds), the degenerate point E_0 shifts toward higher energies (main mechanism: relaxation). The larger the concentration of heavy elements Bi and Pb as compared to the Sb concentration, the larger the splitting k_R (main mechanism: atomic spin-orbit parameter). The degenerate point E_0 shifts upward with increasing Pb concentration (main mechanism: band filling).

The shift k_R of the surface states in reciprocal space versus concentrations x and y is shown in figure 5.5. As expected, the smallest splitting (dark blue) shows up for Sb/Ag(111) ($z = 1 - x - y = 1$), while the largest (dark red) corresponds to Bi/Ag(111) ($x = 1$). For Pb/Ag(111), k_R is of intermediate order (green/yellow). Surprisingly, the splitting is not monotonic, as one might have expected in a rigid-band picture. For example, k_R shows a local minimum at $(x, y, z) \approx (0.4, 0.4, 0.2)$.

As k_R , the Rashba energy E_R depends monotonously in a large range of concentrations (not shown here). Sizable Rashba energies are found mainly for Bi-rich alloys, say for $x > 0.5$. This implies that for accessing region I (cf. figure 5.3), Bi-rich surface alloys are inevitable. The energy E_0 of the degeneracy point depends almost linearly on the heavy elements' concentrations x and y (not shown here). For equal Bi and Sb concentrations ($x = z$) it is nearly constant; upon adding Pb, E_0 shifts up. For systems with about

40 % of Pb concentration, E_0 is very close to the Fermi level E_F , so that the latter lies in region I.

In summary, in **paper II** we investigate three underlying mechanism that can control the Rashba characteristics of the surface alloys on Ag(111). It is also shown that in disordered ternary surface alloys $\text{Bi}_x\text{Pb}_y\text{Sb}_{1-x-y}/\text{Ag}(111)$, the Fermi energy and the Rashba splitting can be independently tuned by choosing the concentrations x and y of Bi and Pb, respectively.

In ‘systematic study’ section, the ordered surface alloys Sb/Ag(111) and disordered binary and ternary surface alloys on Ag(111) are studied. The main achievement of this section are as follows. (i) We examine the atomic spin-orbit contribution to the Rashba splitting. (ii) Our *ab initio* investigation in conjunction with those previously carried out confirm the outcomes of the model calculations. (iii) We examine three mechanisms that can tune the Rashba characteristics in the Rashba systems. (iv) We show the possibility of tuning independently the Fermi energy and the spin splitting in Rashba systems.

5.2 More complicated systems

Here, ‘more complicated systems’ include Bi/Cu(111) with an unconventional spin topology (**paper III**), the system of Bi/BaTiO₃ with a ferroelectric material as the substrate (**paper IV**), the trilayer system of Bi/Ag/Si in which quantum well states and surface states interact (**paper V**), and the (0001) surface of gadolinium as a strongly correlated magnetic material (**paper VI**). The features of these systems are captured either by first-principles calculations or by model calculations.

The first studied system is Bi/Cu(111) for which experimental data are available. Bi/Cu(111) has a similar structure to Bi/Ag(111) but due to the much smaller lattice constant of Cu as compared to Ag, the Bi atoms are more relaxed outward (by 38 % of the bulk interlayer distance of Cu) than in Bi/Ag(111).

The spin-averaged spectral density of a Bi site shows the split sp_z and p_xp_y surface states. The sp_z bands cross at $E_F + 0.1$ eV; their Rashba splitting is $\Delta k = 0.10$ Bohr⁻¹ (Bi/Ag(111): $\Delta k = 0.14$ Bohr⁻¹). The p_xp_y bands cross at $E_F + 1.4$ eV (experiment: $E_F = 1.38 \pm 0.05$ eV), with $\Delta k = 0.08$ Bohr⁻¹ (experiment: $\Delta k = 0.12 \pm 0.02$ Bohr⁻¹). The theoretical results thus are consistent with the experimental findings.

What makes the Bi/Cu(111) system special is not the occupied but the unoccupied surface states that show a spin topology which cannot be explained by the standard Rashba model. For the sp_z branch we find the expected conventional spin topology (line a in figure 5.6) which is imposed by the Rashba model. In contrast, the p_xp_y branch shows a red-red-blue-blue coding at, say, $E_F + 1.0$ eV (line b in figure 5.6); thus, the spins of these surface states have identical rotation direction.

Deviations from a smooth dispersion, as seen at the kink in figure 5.6 (at $(E, \mathbf{k}) \approx (E_F + 0.6$ eV, ± 0.12 Bohr⁻¹)), indicate hybridization of electronic states. A group-theoretical analysis shows that wavefunctions can be represented either as [45]

$$|\psi\rangle = |sp_z \uparrow\rangle + |p_x \uparrow\rangle + |p_y \downarrow\rangle \quad (5.1)$$

or as

$$|\psi\rangle = |sp_z \downarrow\rangle + |p_x \downarrow\rangle + |p_y \uparrow\rangle \quad (5.2)$$

The spinors $|\uparrow\rangle$ and $|\downarrow\rangle$ are quantized with respect to the y axis. Both the outer sp_z band and the inner $p_x p_y$ state belong to the representation of equation (5.1) and hence are allowed to hybridize. Thus, if the usually dominating $|p_y \downarrow\rangle$ component of the inner $p_x p_y$ state is surpassed by the $|p_x \uparrow\rangle$ component, the spin polarization of this state changes sign. At the kink, where the inner $p_x p_y$ band and outer sp_z band approach, both the $|sp_z \uparrow\rangle$ and the $|p_y \downarrow\rangle$ orbitals show a significant spectral density. The inner sp_z and the outer $p_x p_y$ states belong to the representation of equation (5.2) and hybridize as well but less due to their larger (E, \mathbf{k}) ‘distance’. This group-theoretical explanation is fully supported by spin- and orbital-resolved spectral densities.

In summary, there is more to the spin-resolved electronic structure of surface states in surface alloys than first imagined. The basic properties are still described by the Rashba model but important details such as size of the splitting—influenced by the in-plane potential gradient—and the spin structure—altered significantly by hybridization of surface states, as reported here—should be considered when proposing new spin-electronics devices.

The main achievements of **paper III** are: (i) Adding another piece of data to our knowledge about Rashba systems by studying a new Rashba system with a structure similar to Bi/Ag(111). Comparing the systems of Bi on the Ag(111) and Cu(111) surface shows the important role of the substrate. The $4p$ atomic spin-orbit parameter of Cu

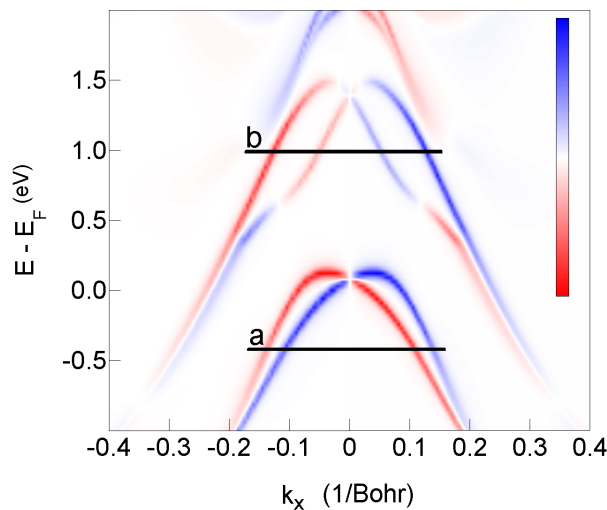


Figure 5.6: Spin-resolved electronic structure of Bi/Cu(111) as obtained by first-principles calculations. The difference $n(E, \mathbf{k})|_{\uparrow} - n(E, \mathbf{k})|_{\downarrow}$ of the spin-projected spectral densities for a Bi site is depicted as color scale (red= negative, white= zero, and blue= positive). The spin projection is in-plane and perpendicular to the wave vector. Horizontal lines are guides to the conventional (line a) and unconventional (line b) spin topology of the sp_z and the $p_x p_y$ states, respectively.

(0.03 eV) is about one-fourth of the $5p$ atomic spin-orbit parameter of Ag (0.11 eV) [43]. Consequently the size of the spin splitting is smaller in surface alloys on Cu(111) than surface alloys on Ag(111). (ii) Studying a system with the ‘Unconventional spin topology’. The spin topology is attributed to the hybridization of occupied and unoccupied states. Since hybridization is a general mechanism, the effect seen in Bi/Cu(111) is probable for similar systems: The unoccupied states in the Bi/Ag(111) system also show a hybridization with the occupied states.

The Rashba systems studied so far show very different Rashba characteristics. Several ways of controlling the Rashba characteristics are discussed in the selected results. In **paper IV** we propose a new route for manipulating the Rashba splitting of electronic states in an adsorbed layer: While keeping a Bi adlayer, we use a ferroelectric, here BaTiO₃(001), in place of a metallic or semiconducting substrate. The reversal of the intrinsic electric polarization P in the perovskite by an external electric field is equivalent to reversing the mutual displacements of Ti and O atoms in [001] direction. Consequently, the charge density at the Bi/BaTiO₃ interface is changed, leading eventually to a modification of the Rashba splitting of the surface states in the Bi adlayer.

Rashba/ferroelectric systems have a number of advantages. First, because the electric polarization P is changed by an electric pulse in contrast to a steady electric field, the Rashba splitting would remain switched permanently. This feature makes such a system suitable for information storage devices. Second, the deposition of adatoms could alter the surface electronic structure significantly and switching of the splitting may be difficult or even impossible. Thus, Bi/BaTiO₃ and similar systems lend themselves support for a new class of materials for spin electronics devices.

A total-energy analysis shows that for both P_{\uparrow} and P_{\downarrow} , the polarization at the topmost TiO₂ layer is negative (i. e. $z_{\text{Ti}} < z_{\text{O}}$). However, the relaxations of these atoms differ: $z_{\text{Ti}} - z_{\text{O}} = -0.13 \text{ \AA}$ for P_{\uparrow} and -0.18 \AA for P_{\downarrow} .

The Bi adlayer gives rise to occupied $6p$ electronic states in the fundamental band gap of the surface BaTiO₃ stack. These are mostly confined to the Bi layer but show also considerable spectral weight in the adjacent layer, making them subject to switching of P . The dispersions of the Bi surface states show the typical signatures of the Rashba splitting: k_R and the Rashba energy E_R which are indicated in figure 5.7 (a).

The switching of the electric polarization P affects indeed the Rashba splitting k_R , thereby confirming the above motivation. The strength of this spin-electric coupling is quantified by the relative change in k_R ; for $\bar{\Gamma} - \bar{M}$ it is about 4.5% whereas for $\bar{\Gamma} - \bar{X}$ it is about 5.5%. These numbers are qualitatively explained on one hand by the weak polarization dependence of the surface geometry and on the other hand by the strong localization of the Bi $6p$ states to the adlayer. Both a larger relaxation and a stronger hybridization of the Bi states with those of the substrate could enhance the effect.

In summary, our theoretical investigation in **paper IV** provides a proof of concept for spin-electric coupling in an adlayer of a heavy p metal on a ferroelectric substrate. Switching of the intrinsic electric polarization P in the ferroelectric [here: BaTiO₃] affects the strength of the Rashba splitting in the adlayer [here: Bi]. This work predicts a

moderate spin-electric coupling but a large absolute Rashba-type spin splitting. Nevertheless, it is conceivable to increase the effect by larger atomic displacements in particular at the ferroelectric/adlayer interface. Our findings may pave a route for spin-electronic devices.

In **paper V**, we introduce another way for controlling the electronic structure at the Fermi level. We investigate the trilayer system of Bi/Ag/Si(111) in which the electronic structure at the Fermi energy is tailored by tuning the thickness of the buffer layer.

Experiments on thin layers of bismuth on silicon have shown the spin-orbit splitting of the surface states but failed to highlight any splitting of the Bi bulk electronic states [46]. It was also shown for this system that the hybridization between bulk and surface states removes the spin-orbit splitting of the surface states. To combine the giant spin

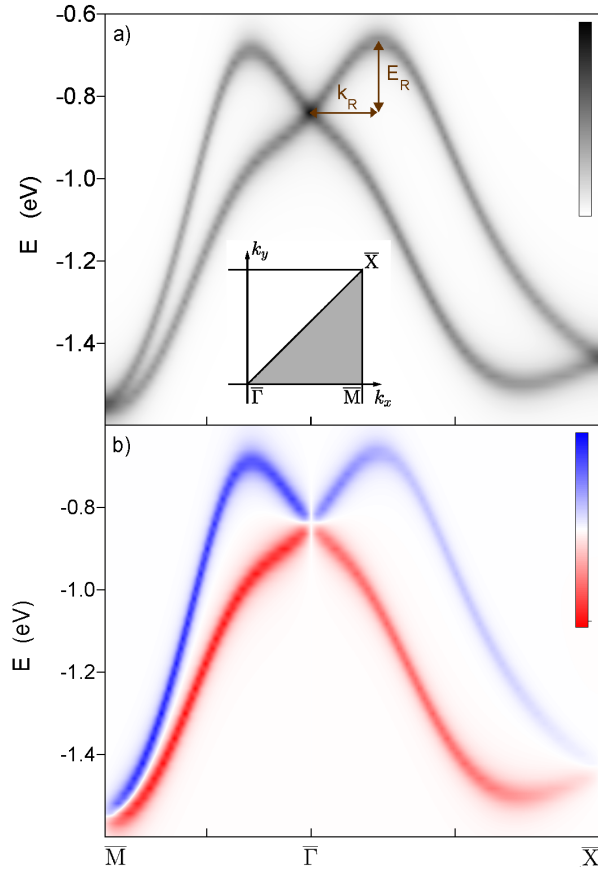


Figure 5.7: Surface states in Bi/BaTiO3(001) for P_{\uparrow} . (a) Spin-integrated Bloch spectral density for Bi imaged as gray scale (white 0, black 400 states/Hartree) along $\bar{M}-\bar{\Gamma}-\bar{X}$ of the two-dimensional Brillouin zone. The Rashba splitting k_R and the Rashba energy E_R are indicated. The inset shows a quarter of the Brillouin zone. (b) Spin-resolved density for Bi depicted as color scale. Blue (red) indicates a positive (negative) difference $n_{\uparrow} - n_{\downarrow}$, with the spin projection normal to \mathbf{k}_{\parallel} .

splitting of the Bi/Ag(111) surface alloy with the established electronics material silicon, we investigated a trilayer system composed of a BiAg surface alloy, a thin Ag film and a Si substrate.

For the systems with Si substrate, focusing here on exemplary results for $d = 10$ [figure 5.8 (b)] and 19 [figure 5.8(c)], quantum well states (QWSs) show up as parabolas centered at $\bar{\Gamma}$. The most striking difference to Bi/Ag(111) [figure 5.8 (a)] are spin-dependent band gaps at $(E, \mathbf{k}_{\parallel})$ points at which the QWSs would cross the Bi bands. With increasing thickness of the Ag buffer, the number QWSs increases and the widths of the gaps decrease. We now address, in particular, the electronic structure at the Fermi level. For $d = 10$ ML [figure 5.8 (e)], highly spin-polarized states show up at $\mathbf{k} = \mathbf{k}_F = 0.22 \text{ \AA}^{-1}$, with a spin polarization of about 33%. On the contrary, a complete gap appears for $d = 19$ ML, figure 5.8 (f). These findings imply that the spin-dependent electronic structure at the Fermi level — and thus the transport properties — can be drastically modified by the Ag film thickness.

In summary, findings of **paper V** suggest that it is indeed possible to match systems with large spin-orbit splitting [here: Bi/Ag/(111)] with a semiconductor substrate. Furthermore, interfacial properties can be custom tailored, in the present case by a single parameter, namely, the Ag buffer layer thickness.

The main goal of **Paper VI** is to study the surface states of a magnetic surface. What makes the study of Gd(0001) interesting is the electron correlation. Conventional LSDA calculations predict almost all the properties of the Gd bulk and surface incorrectly. In the framework of DFT, the remedy of this problem is an exchange-correlation energy functional which treats the electron correlation in an improved way. We choose the local version of the self-interaction correction method which is described in chapter 2.

Applying SIC to calculate the ground state properties of Gd, e. g. magnetic ordering and local magnetic moments, is very successful. For excited states, it appears that the binding energies of the SI-corrected localized levels are significantly too large when compared to those determined from spectroscopical data, i. e. from photoemission intensities. This ‘overcorrection’ of the SIC is attributed to the orbital relaxation. SIC calculations are ground state calculations and one cannot expect accurate results for excited states. In our calculations we used the transition state approximation (TSA), that is an average of two ground state potentials (LSD and SIC potentials), to obtain a better agreement with experiments that are associated with the excited states.

The occupied surface states of Gd(0001) are mostly d_{z^2} -majority states which hybridize with the $4f$ -majority states. Consequently, the treatment of the electronic correlation within the $4f$ states has an effect on both binding energy and dispersion of the surface states. The d - f hybridization of the surface state can be quantified by the ratio of the d - and f - contributions to its spectral density N at $\mathbf{k}_{\parallel} = 0$. In agreement with the increased local magnetic moment at the surface ($8.0 \mu_B$ for SIC and $7.3 \mu_B$ for LSD), the d - f hybridization of the surface state is larger for SIC ($d/f = 7$) than for LSD ($d/f = 50$).

The majority surface-state dispersion of Gd(0001) is shown in figure 5.9. For the LSD

approximation, the binding energy of 0.22 eV at $\mathbf{k}_{\parallel} = 0$ ($\bar{\Gamma}$) deviates sizably from the experimental result (0.16 eV, dots). More striking is, however, the positive dispersion at small wave vectors which does not match the negative dispersion in experiment. Application of the SIC leaves the binding energy almost unchanged (0.23 eV) but results in a strongly negative dispersion which also does not fit to experiment. The surface-state dispersion calculated by TSA shows a plateau at small \mathbf{k}_{\parallel} , and the binding energy of 0.18 eV almost hits that of the experiment.

Another feature of figure 5.9 is the displacement of energy dispersion curves in the regions with positive and negative \mathbf{k} . At a magnetic surface, spin degeneracy is lifted by the exchange interaction and majority spins are align along the quantization axis. The effect of the Rashba spin-orbit interaction is mainly a modification of the energy dispersion, i. e. moving the dispersion relations with respect to each other.

In summary, **paper VI** shows that the self-interaction correction to the local spin-

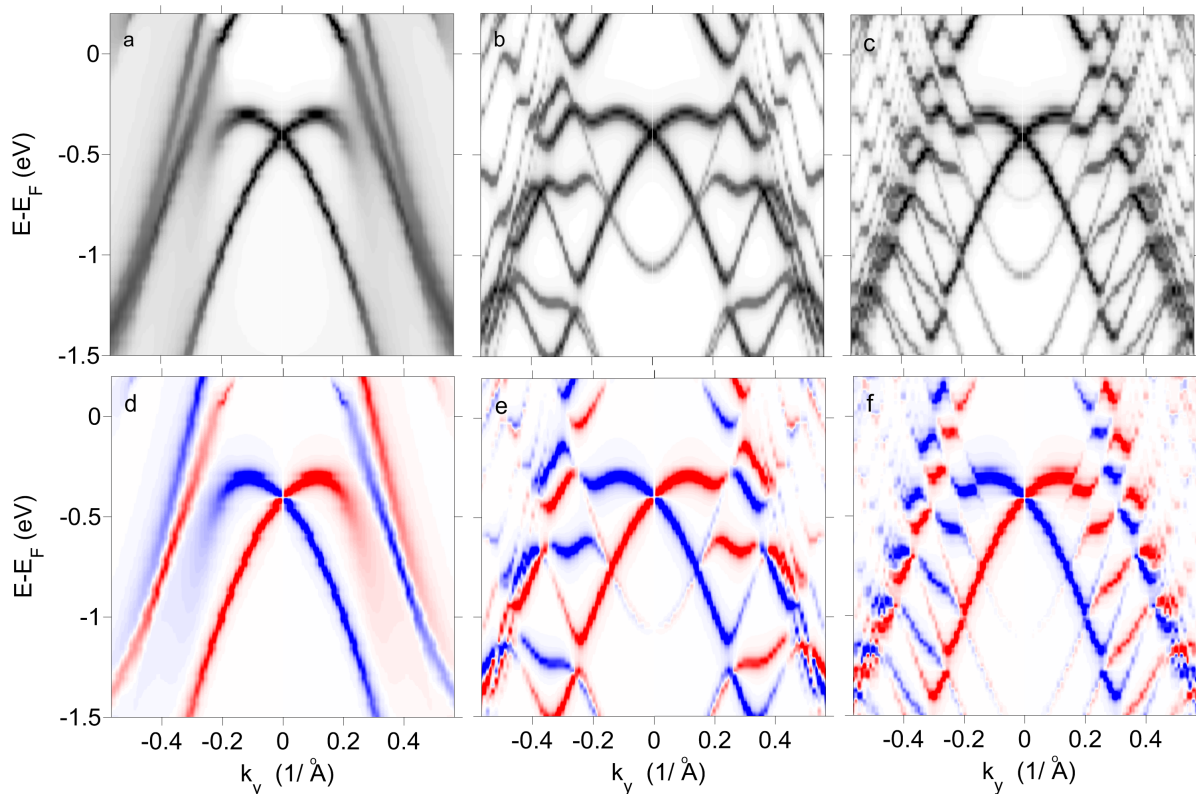


Figure 5.8: Effect of QWSs on the spin-split electronic structure of the Bi/Ag surface alloy, as obtained from first-principles electronic-structure calculations. (a)-(c): The spectral density at the Bi site is displayed as gray scale (with white indicating vanishing spectral weight) for Bi/Ag(111) (a) and Bi/Ag/Si(111) for Ag buffer thicknesses $d = 10$ (b) and $d = 19$ (c). (d)-(f): The spin polarization of the electronic states is visualized by $\Delta N(E, \mathbf{k}_{\parallel})$, i. e. the difference of the spin-up and the spin-down spectral density. Red and blue indicate positive and negative values, respectively, where white is for zero ΔN .

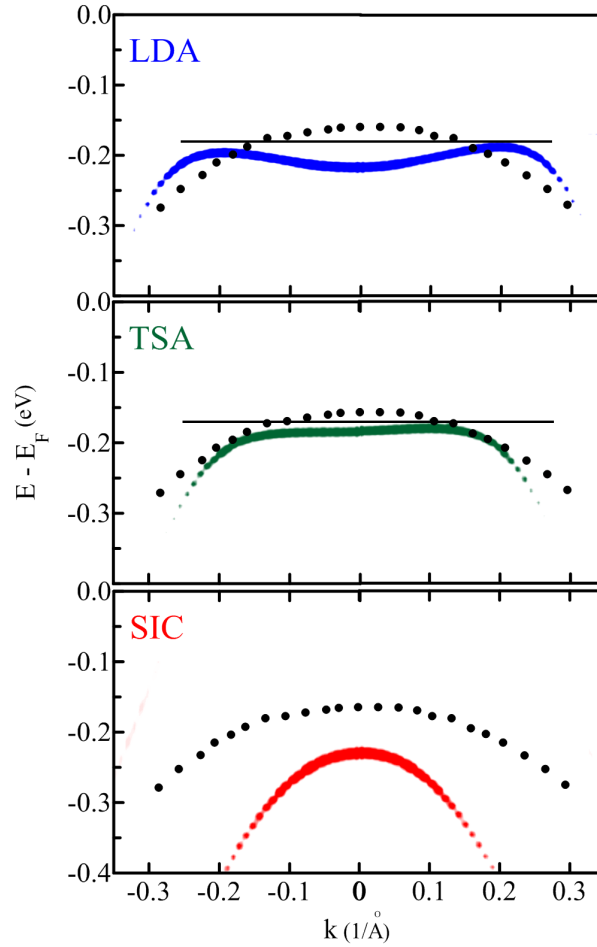


Figure 5.9: Effect of electronic correlations on the d_{22} -majority surface state of Gd(0001). The spectral densities calculated within the local spin-density (LSD) approximation, the transition-state approximation (TSA), and the self-interaction correction (SIC) are shown along the $\bar{M} - \bar{\Gamma} - \bar{M}$ line of the surface Brillouin zone. Experimental data (dots) are reproduced from [15]. The Rashba effect shows up as asymmetry of the dispersion ($E(\mathbf{k}) \neq E(-\mathbf{k})$). The in-plane magnetization is perpendicular to \mathbf{k}_{\parallel} , \mathbf{k}_{\parallel} along $\bar{M} - \bar{\Gamma} - \bar{M}$.

density approximation improves considerably the description of ground-state properties of correlated systems. Its flavor for excited states, i. e. the transition-state approximation, is capable to describe correctly spectroscopic data.

The main achievement of **Paper VI** is the successful deal with a complex interplay of electronic correlations, surface relaxation, and spin-orbit coupling on the magnetic ordering, the Curie temperature and the surface-state dispersion. A key issue in our calculations is these do not rely on any adjustable parameter which is related to electronic correlations.

5.3 Summary

To summarize this chapter, we investigate several different Rashba systems. I categorize the Rashba systems to two groups; the ‘common Rashba systems’ and ‘more complicated Rashba systems’.

Studying the common surface alloys Rashba systems leads to a systematic study of this unique class of Rashba systems. The outcomes of the model calculations, which are taken as simple as possible to be solveable, are confirmed by our *ab initio* calculations. Thus the first part of this study provide a comprehensive understanding of surface Rashba systems.

More complicated systems are the systems that show a peculiar behavior. A good knowledge of the influential parameters in the common Rashba systems is essential to understanding the behavior of the more complicated systems.

Among the more complicated systems, Bi/Cu(111) has a twofold role. On one hand the studying of the occupied states of Bi completes our knowledge about the common Rashba systems. On the other hand the unoccupied states of Bi show a unconventional spin topology which is considered as a peculiar behavior of the system.

Among the studied systems, three of them could find applications in new spintronic devices. The common feature of these systems is to have tunable Rashba characteristics. Rashba characteristics k_R and E_R can be independently tuned by choosing the concentrations of Bi and Pb in disordered ternary surface alloys $\text{Bi}_x\text{Pb}_y\text{Sb}_{1-x-y}/\text{Ag}(111)$. In the trilayer system of Bi/Ag/Si(111), the band gap structure at the Fermi level can be tailored by the Ag layer thickness. A ferroelectric control of Rashba spin-orbit coupling is proposed in the system of Bi/BaTiO₃.

The study of the Rashba-like splitting of the surface states of a correlated magnetic surface has several advantages. It gives support for the experimental findings. It also could be a test for the method developed for our calculations. Treating a correlated system requires a method beyond the commonly used LSDA. In our calculations we used a simplified version of SIC. The transition state approximation considerably improves the description of excited states in systems with electronic correlations.

5.4 Selected results

The remain of this chapter is devoted to the selected publications. The previously briefly presented results could be found in the extended form in the publications.

Paper I

Assessing the atomic contribution to the Rashba spin-orbit splitting in surface alloys: Sb/Ag(111)

Assessing the atomic contribution to the Rashba spin-orbit splitting in surface alloys: Sb/Ag(111)L. Moreschini,¹ A. Bendouan,² I. Gierz,³ C. R. Ast,³ H. Mirhosseini,⁴ H. Höchst,⁵ K. Kern,³ J. Henk,⁴ A. Ernst,⁴ S. Ostanin,⁴ F. Reinert,⁶ and M. Grioni¹¹*Institut de Physique des Nanostructures, Ecole Polytechnique Fédérale de Lausanne (EPFL), CH-1015 Lausanne, Switzerland*²*Experimentelle Physik II, Universität Würzburg Am Hubland, D-97074 Würzburg, Germany and Synchrotron Soleil, L'Orme des Merisiers, Saint-Aubin, BP 48, F-91192 Gif-sur-Yvette Cedex, France*³*Max-Planck-Institut für Festkörperforschung, D-70569 Stuttgart, Germany*⁴*Max-Planck-Institut für Mikrostrukturphysik, D-06120 Halle (Saale), Germany*⁵*Synchrotron Radiation Center, University of Wisconsin, Stoughton, Wisconsin 53589, USA*⁶*Experimentelle Physik II, Universität Würzburg Am Hubland, D-97074 Würzburg, Germany and Gemeinschaftslabor für Nanoanalytik, Forschungszentrum Karlsruhe, D-76021 Karlsruhe, Germany*

(Received 20 October 2008; published 11 February 2009)

We have studied the electronic structure of the Ag(111)($\sqrt{3} \times \sqrt{3}$)R30°-Sb surface alloy by angle-resolved photoemission. We find two hybrid surface bands, similar to the isostructural Ag(111)-Bi interface. The spin-orbit coupling induced spin splitting in momentum space, however, is strongly reduced from the Bi case. First-principles and model band calculations correctly reproduce this difference. The present results illustrate the complex interplay of atomic and structural contributions at the origin of the large spin separation in these systems.

DOI: [10.1103/PhysRevB.79.075424](https://doi.org/10.1103/PhysRevB.79.075424)

PACS number(s): 73.20.At, 79.60.-i, 71.70.Ej

I. INTRODUCTION

The normal spin degeneracy of the electronic states of nonmagnetic solids is lifted by the spin-orbit (SO) interaction in systems that present a structural inversion asymmetry (SIA). This effect, first discussed for nearly free electrons (NFEs) by Rashba and Bychkov (RB),¹ has been extensively studied in semiconductor heterostructures,² with the prospect of future applications where spins could be manipulated by an electric field. It has been shown by angle-resolved photoelectron spectroscopy (ARPES) that an even larger effect occurs at the Au(111) surface.^{3–5} SO-split bands have later been observed at surfaces and interfaces of *p*,^{6–8} transition,^{9–12} and rare-earth¹³ metals, in disordered Au/Ag alloys¹⁴ and in Au quantum wires.¹⁵ Recently, large SO splittings have been measured by ARPES in single-layer ordered metallic alloys formed by high-*Z* metals (Bi and Pb) at the Ag(111) surface.^{16–18} In Bi/Ag(111), in particular, the wave-vector separation ($2 \cdot k_0$; see below) was found to be 1 order of magnitude larger than in Au(111), and much larger than typical values found in semiconductor heterostructures. It would be desirable to clarify the origin of such unexpectedly large values, both for fundamental reasons and because k_0 is an important figure of merit for possible applications.

The RB model considers two-dimensional (2D) free electrons subject to a surface electrostatic potential V_s whose gradient, the surface electric field, is assumed to be oriented along the surface normal \vec{e}_z . The electron spin couples to the magnetic field appearing in the rest frame of the electron. The free-electron parabola is replaced by a more complex but still isotropic dispersion $E_{\pm}(k) = \frac{\hbar^2 k^2}{2m} \pm \alpha_R k$, where the \pm subscript refers to the two spin states, and the quantization axis is perpendicular to \vec{e}_z and to \vec{k} . The Rashba parameter α_R , which is proportional to ∇V_s , indicates the strength of the coupling. A cut along a generic direction within the plane then yields two parabolic branches shifted away from $\bar{\Gamma}$ by

$k_0 = \frac{\alpha_R m}{\hbar^2}$. This picture is qualitatively consistent with the main experimental features, but quantitatively inaccurate, since typical values of ∇V_s yield band splittings orders of magnitude too small. Modern first-principles calculations^{16,19} achieve impressive quantitative agreement with the experimental data, but provide only limited insight of the physical origin of the splitting.

Since the electric field probed by the electron is strongest near the ion cores, a realistic description of the phenomenon should include atomic aspects. This was first accomplished in a tight-binding model, where the SO splitting depends on the product of the surface-potential gradient times the atomic SO parameter.²⁰ For clean metal surfaces the splitting depends not only on the atomic number *Z*, but also on the orbital character of the surface-state wave function, e.g., on the relative sizes of the *p* and *s* components in an *sp* surface state. It has been proposed that the asymmetry of the wave function near the position of the nuclei resulting from mixing different *l* states might be the single most important factor leading to a SO splitting.²¹ On the other hand, the direct or indirect role of the surface potential is illustrated by the observed dependence on the Miller indices of the surface,⁶ and also on the presence of adsorbates.²²

For surface alloys such as Bi/Ag(111) and Pb/Ag(111), the strength of the atomic SO interaction of both the substrate and the overlayer is clearly important, but is not the only relevant parameter. For instance, the SO coupling induced spin splitting measured for the Bi/Ag(111) alloy ($k_0 = 0.13 \text{ \AA}^{-1}$) is larger than for both the Ag(111) and Bi(111) surfaces. It is also four times larger than for the Pb/Ag(111) alloy ($k_0 = 0.03 \text{ \AA}^{-1}$),¹⁸ even if the *6p* atomic SO parameter ζ_{6p} increases by only 37% between Pb (0.91 eV) and Bi (1.25 eV).²³ The inhomogeneous charge distribution within the alloy yields an in-plane component of the surface-potential gradient which, in the presence of an in-plane SIA, also contributes to the SO splitting. The results of a NFE

model including the SO interaction indeed suggest that this term is crucial to achieve very large values of k_0 .²⁴ Moreover, spin-resolved ARPES measurements on Bi/Ag(111) and Pb/Ag(111) have detected a substantial out-of-plane component of the spin polarization, a telltale consequence of the in-plane gradient.²⁵ Surface corrugation, or equivalently the relaxation of the adsorbate layer, is another key parameter that controls the hybridization with the substrate, and therefore the orbital composition of the surface states.^{16,19} Finally, the electronic states of the alloys are more localized than the noble-metal surface states. As a result, they probe the surface-potential gradient more effectively, and the asymmetry of their wave functions is enhanced with respect to the clean metal counterparts.

Only a few combinations of p -metal adsorbates and noble-metal substrates have been studied so far. More experimental information is necessary to develop a comprehensive model of SO splitting in these systems. As a step in this direction we present here ARPES data and band-structure calculations for the Sb/Ag(111) surface alloy. The structural parameters of this interface are very close to those of the well-characterized Bi/Ag and Pb/Ag systems. The Sb adatoms replace every third Ag atom in the topmost layer to form a surface alloy with a $(\sqrt{3} \times \sqrt{3})R30^\circ$ surface superstructure with nominal SbAg_2 stoichiometry, similar to the substitutional PbAg_2 and BiAg_2 surface alloys formed by Pb and Bi at the Ag(111) surface. The alloy layer exhibits a preferential hcp stacking relative to the substrate, although an fcc stacking is also possible.^{26–28} Sb and Bi have the same s^2p^3 electronic configuration, but the atomic SO interaction in the Sb $5p$ valence states is considerably weaker [$\zeta_{5p}(\text{Sb}) = 0.4$ eV].²³ Therefore Sb/Ag(111) provides an almost ideal opportunity to assess the role of atomic contributions to the SO splitting.

II. METHODS

The SbAg_2 surface alloy was prepared by evaporation of 1/3 of a monolayer of Sb on the hot Ag(111) substrate ($T > 400$ K), followed by an annealing at $T = 600$ K. The crystalline order was checked by low-energy electron diffraction (LEED). ARPES measurements were performed in Würzburg and Stuttgart, utilizing He I ($h\nu = 21.2$ eV) radiation from a high-brightness monochromatized helium lamp, and at the Synchrotron Radiation Center in Madison, Wisconsin. Hemispherical electrostatic analyzers were used to measure ARPES intensity maps over acceptance angles of $\pm 13^\circ$ and $\pm 7^\circ$ in the nondispersive direction. The energy resolution was better than 10 meV, and the angular resolution was 0.3° , corresponding to a wave-vector uncertainty of $\sim 0.01 \text{ \AA}^{-1}$.

For the first-principles calculations we followed the multicode approach which already proved to be effective in reproducing the band structure of the Pb/Ag(111) and Bi/Ag(111) surface alloys.^{16,18} The geometric structure of the surface has been obtained by the Vienna *Ab Initio* Simulation Package (VASP). The surface electronic structure has been computed by our relativistic layer Korringa-Kohn-Rostoker (KKR) code,²⁹ using the optimized geometry as input. Since

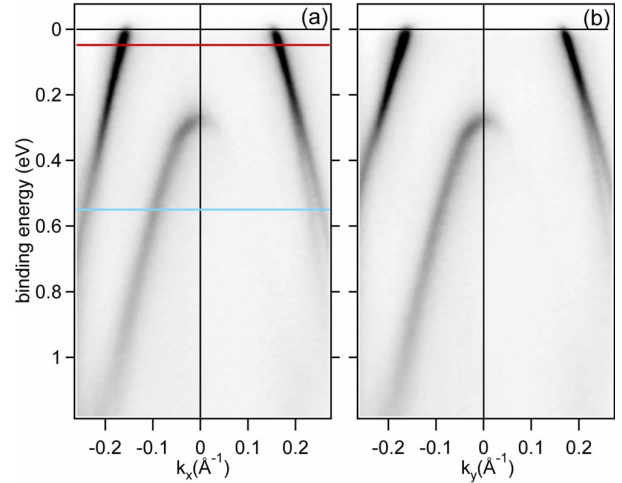


FIG. 1. (Color online) ARPES intensity maps ($h\nu = 21.2$ eV) of the SbAg_2 surface alloy, measured at $T = 100$ K around $\bar{\Gamma}$ along (a) the $\bar{\Gamma}\bar{K}$ and (b) the $\bar{\Gamma}\bar{M}$ directions of the surface BZ.

first-principles calculations do not allow to distinguish *per se* the various contributions (atomic, perpendicular SIA, and in-plane SIA) to the RB splitting, we calculated the surface band structure also within an NFE model. In the latter, the mechanisms involved in the formation of the SO split-band structure are parametrized, thus allowing their interplay to be investigated on a semiquantitative level.

III. RESULTS AND DISCUSSION

Figure 1 shows two ARPES intensity maps for the SbAg_2 alloy, measured around $\bar{\Gamma}$, the center of the hexagonal surface Brillouin zone (BZ), along the $\bar{\Gamma}\bar{K}$ [$\bar{K} = (0.84 \text{ \AA}^{-1}, 0)$] and $\bar{\Gamma}\bar{M}$ [$\bar{M} = (0, 0.72 \text{ \AA}^{-1})$] high-symmetry directions. They show two spectral features dispersing downward from $\bar{\Gamma}$, with an asymmetric intensity distribution that is due to ARPES transition matrix elements and to the geometry of the experiment. Although we will refer hereafter to each of these features as a “band”, both of them exhibit some internal structure, as discussed below. The lower-band maximum is at a binding energy of 0.27 eV and the dispersion is well approximated by a parabolic fit, with effective mass $m^* = -0.15 \pm 0.01 m_e$, where m_e is the bare electron mass. The upper band forms a hole pocket at $\bar{\Gamma}$. It crosses the Fermi level at $k_F(\bar{\Gamma}\bar{K}) = 0.15 \text{ \AA}^{-1}$ and $k_F(\bar{\Gamma}\bar{M}) = 0.17 \text{ \AA}^{-1}$. In this case a parabolic fit would yield ambiguous results because of this slight anisotropy and of the underlying internal structure.

The bands of Fig. 1 appear after the surface alloy is formed. They replace the Ag(111) Shockley state with minimum at ~ 0.06 eV on the clean surface, and reflect the hybridization between the adsorbate and the substrate states. By analogy with the isostructural PbAg_2 and BiAg_2 alloys,^{16,17} we attribute the lower band to states of mainly $\text{Sb}sp_z$ and $\text{Ag}s$ characters. The upper band has mainly p_{xy} character. These assignments are confirmed by our first-principles calculations. However, while in the Bi and Pb alloys each band

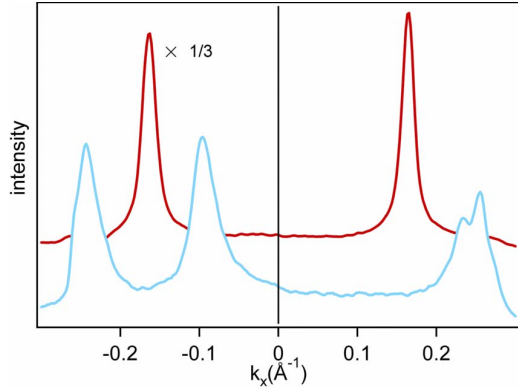


FIG. 2. (Color online) MDCs extracted from the ARPES map of Fig. 1(a), in correspondence of the horizontal lines at $E=0.05$ eV (top, red or dark gray line) and $E=0.55$ eV (bottom, blue or light gray line).

exhibits a clear SO splitting, the effect is considerably smaller here. The two split components are only resolved in the upper band for $k > 0.2 \text{ \AA}^{-1}$, near the edges of the intensity maps. Their different slopes suggest that they cross at about 0.3 eV binding energy and partially overlap up to the Fermi level. Such crossing is at variance with the Bi/Ag and Pb/Ag cases, where the SO-split bands are mainly shifted in k and only cross at the high-symmetry points $\bar{\Gamma}$ and \bar{M} . The lower band does not exhibit a visible splitting, but its trace is broader than the experimental wave-vector uncertainty, suggesting also in this case an underlying structure. The wave-vector broadening can be observed all the way to the band maximum, where the width in the energy direction is small, which again points to the presence of two underlying components.

These qualitative conclusions are confirmed by momentum distribution curves (MDCs) extracted from the intensity map of Fig. 1(a) in correspondence of the horizontal lines at $E=0.05$ eV and $E=0.55$ eV (Fig. 2). At 0.05 eV the line cuts only the upper band, and the corresponding MDC exhibits two sharp peaks on opposite sides of $\bar{\Gamma}$ with nearly Lorentzian line shapes. The MDC at 0.55 eV, which cuts both bands, shows broader line shapes for both bands, and partially resolved split components in the upper band at $k = \pm 0.25 \text{ \AA}^{-1}$. Remarkably, the intensity at the $k > 0$ crossing of the lower band (at $k \approx 0.08 \text{ \AA}^{-1}$) is totally suppressed.

To get more insight into the cause of the small splitting and of the peculiar crossing in the band structure of Sb/Ag(111), we performed first-principles calculations using the KKR method. The surface relaxation is a crucial parameter, as it influences both the size of in-plane and perpendicular potential gradient, and the amount of hybridization between sp_z and p_{xy} orbitals. The atomic positions as computed using the VASP yielded an outward relaxation of the Sb atoms of about 10%, close to the value of 15% found for Bi in Bi/Ag(111) and consistent with the slightly smaller size of the atomic radius of the Sb atom [2.9 \AA (Sb) vs 3.1 \AA (Bi)]. The value of 10% is somewhat larger than the 2–3% estimated from independent experiments.^{27,28} On Bi/Ag(111) no experimental structural data are available. However, the

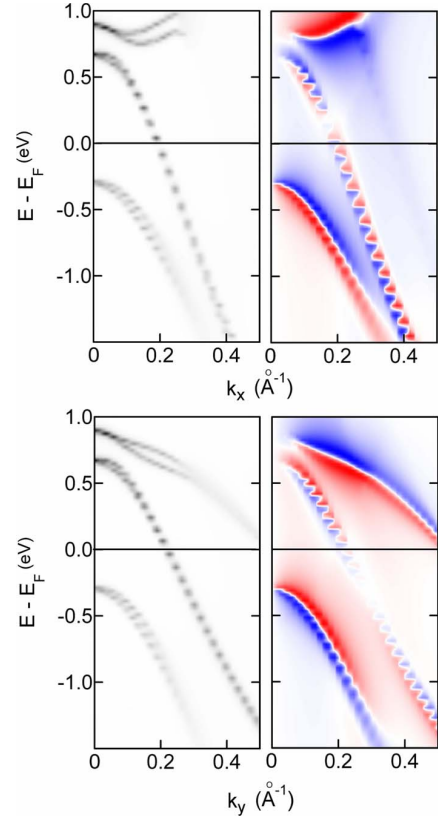


FIG. 3. (Color online) Left: the calculated total spectral density $N=(N_{\uparrow}+N_{\downarrow})$, for the $\bar{\Gamma K}$ (top) and $\bar{\Gamma M}$ (bottom) directions. Right: the in-plane spin polarization P_{σ} ($\sigma=x,y$ for $k=k_{y,x}$), depicted with positive and negative values represented by blue and red, respectively. White is for zero polarization.

buckling values produced by our simulations seem to indicate that we deal with two very similar interfaces.³⁰

The spectral densities as given by the KKR method are shown in Fig. 3 for the same maps of Fig. 1. The spin polarization of these surface states is mainly in plane and normal to the wave vector. Thus, for the wave vector along the x axis (y axis) the spin is oriented in the y direction (x direction), but with opposite orientation for the spin-split pairs of states. In the calculations we have decomposed the spectral density at a Bi site with respect to the spin components along these directions, thus obtaining the spin-resolved spectral densities N_{\uparrow} and N_{\downarrow} . The total spectral density $N=(N_{\uparrow}+N_{\downarrow})$ is shown in the left panels of the figure. The corresponding in-plane spin polarization $P_{\sigma}=[(N_{\uparrow}-N_{\downarrow})/(N_{\uparrow}+N_{\downarrow})]$ ($\sigma=x,y$ for $k=k_{y,x}$) is shown in the right panels. The dispersion of the calculated bands follows nicely the experimental data. The spin splitting, evident in the right panels, is barely visible in the total density maps. The maximum energy separation (<100 meV) would be detectable with our energy resolution, but the ARPES linewidth in these surface alloys is dominated by surface disorder, which explains why the experiment cannot access this detail. The calculation also reproduces the anomalous crossing in the upper (mainly p_{xy}) band set. It occurs in the vicinity of the Fermi level, in the region showing vanishing spin polarization, i.e., at (E, k_x)

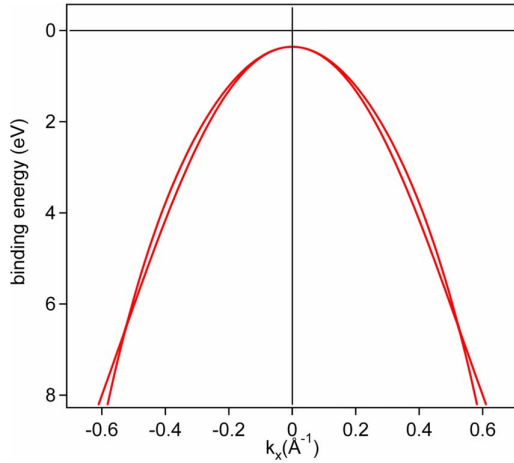


FIG. 4. (Color online) Split bands obtained from an NFE model including the SO interaction.

$= (0.2 \text{ eV}, 0.18 \text{ \AA}^{-1})$ and $(E, k_y) = (-0.4 \text{ eV}, 0.28 \text{ \AA}^{-1})$. A third set of bands at higher energies, dispersing upward in the $\bar{\Gamma K}$ direction, is ascribable to p_{xy} ($m_j = 3/2$) states.

Interestingly, the outcome of the KKR calculations in terms of orbital hybridization indicates a similar ($\approx 25\%$) admixture of p_{xy} character in the sp_z bands for both the Sb/Ag and the Bi/Ag systems. This is a key point as it shows that the “sensitivity” to the in-plane gradient should be about the same in both systems and cannot explain the difference in the size of the splitting. Therefore, the smaller splitting in Sb/Ag(111) compared to that in Bi/Ag(111) is mainly due to the smaller atomic SO interaction. In other words, a strong in-plane gradient is not effective in generating a strong SO splitting of the interface bands unless supported by a significant atomic contribution from the adsorbate. This consideration is not influenced by the top layer stacking since the calculations show no sizable difference between the faulted and the nonfaulted surface reconstructions.

The individual contributions to the SO splitting cannot be clearly separated, in particular in a first-principles computer code. However, in model calculations that capture the essential ingredients they can be switched on and off individually, and their mutual interplay on the splitting can be analyzed. An NFE model has been recently developed to treat the presence of SIAs in a 2D electron gas.²⁴ It qualitatively illustrates the different contributions from an in-plane and a perpendicular potential gradient to the spin splitting. If we calculate the band dispersion for an in-plane gradient only, we can reproduce the band crossing away from the $\bar{\Gamma}$ point. The result is displayed in Fig. 4 for the $\bar{\Gamma K}$ direction. As the perpendicular gradient is set to zero in this case, there is no momentum offset of the band maximum away from the $\bar{\Gamma}$ point. This can be attributed to the fact that the in-plane gradient results in higher-order contributions than the perpendicular gradient, which shows a linear contribution. Only the combination of the in-plane and the perpendicular gradients will result in a strong enhancement of the spin splitting according to the NFE model. For the present case of Sb/Ag(111) we qualitatively conclude that we have a strong in-

plane contribution of the potential gradient, but since the atomic SO interaction in Sb is much weaker than in Bi, a strong enhancement of the spin splitting cannot be expected. Notice that in a freestanding surface alloy, the in-plane inversion symmetry is conserved, and the SIA comes into play only when considering the interaction with the underlying substrate layers.

From the experimental and theoretical results we can then identify three ingredients to the spin-orbit splitting of the surface states: (i) the atomic contribution, due to the strong Coulomb potential of the nuclei, (ii) the perpendicular potential gradient, due to the surface-potential barrier, and (iii) the in-plane potential gradient, due to the surface geometry. The last one can be viewed as a crystal-field effect of the subsurface layers on the topmost layer. Both the perpendicular and the in-plane gradients break the symmetry of a freestanding Sb/Ag surface layer (which does not show Rashba splitting). The strongest contribution is the atomic one. The other two are orders of magnitude less than the atomic contribution and approximately of the same strength. This hierarchy suggests the following scenario: for a sizable splitting, a strong atomic contribution is inevitable, as can be seen from the surface-state splitting in the series Cu(111)-Ag(111)-Au(111). An additional mechanism (here, the in-plane gradient) can increase the splitting, as seen for Bi/Ag(111) and Pb/Ag(111). However, such mechanism can only “trigger” the effect. Without a strong atomic contribution, the splitting is small, as proven in the present work on Sb/Ag(111).

While the SbAg₂ bands are approximately free-electron-like near the center of the BZ, the dispersion is strongly affected by the lattice potential at larger k values. This aspect is not included in the simple RB model of the SO splitting, and adds interesting structure to the in-plane spin polarization.¹⁶ The departure from an isotropic dispersion is illustrated by the calculated band structure of Fig. 3. Hints of an anisotropy are visible already in the maps of Fig. 1: (i) the Fermi wave vectors of the upper band are different in the two directions, and (ii) the upper and lower bands get closer in energy along $\bar{\Gamma K}$ but not along $\bar{\Gamma M}$. The anisotropy is especially evident in the constant-energy contours of Fig. 5, obtained by cutting the experimental band structure at four binding energies between the Fermi level and 2.1 eV. At E_F [Fig. 5(a)] the map shows a hexagonal contour centered at $\bar{\Gamma}$ from the upper (p_{xy}) band. A second smaller contour, from the lower band, is present in the $E = 0.4 \text{ eV}$ map [Fig. 5(b)], but only part of it is visible due to the strong intensity modulation already evident in Fig. 1. Both contours grow in size at larger binding energies. In panel (c) the lower-band contour is also hexagonal, but rotated by 30° with respect to the upper-band contour, which is distorted into a flowerlike shape. Since the highest spin polarization is predicted at the corners of the hexagons,^{16,24} the angular mismatch of the constant-energy contours yields a similar offset in the spin polarization of the two bands. The larger and weaker hexagonal shape, visible in panels (a)–(d) of Fig. 5 and schematically reproduced in Fig. 5(e), is formed from arcs due to the backfolding of the NFE bulk Ag sp conduction band at the BZ boundaries of the surface alloy. These arcs cross the contours of the alloy bands without being distorted. Therefore

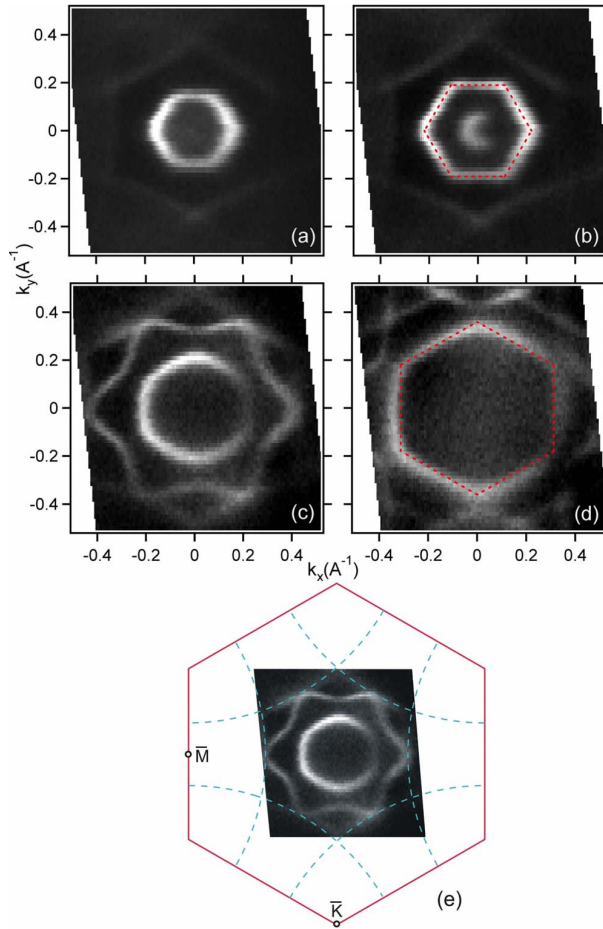


FIG. 5. (Color online) Constant-energy contours obtained at (a) the Fermi level and at (b) 0.4, (c) 1.3, and (d) 2.1 eV binding energies. The dashed hexagons are guides to the eye. Panel (e), which reproduces the data of panel (c), shows the surface BZ and the backfolded contours of the bulk Ag *sp* conduction band.

the backfolding of the Ag bulk band is simply a final-state effect, namely, the diffraction of the outgoing photoelectrons by the ordered overlayer.

It is interesting to compare the hexagonal contours of Fig. 5 with the circular Fermi surfaces of the Shockley states of the clean (111) surfaces of Cu, Ag, or Au. The larger size of the alloy Fermi surface relative to the BZ cannot entirely explain the difference. In particular, for the Au(111) surface the ratio ($k_F/\bar{\Gamma M}$) is only 30% smaller than the corresponding ratio for the SbAg₂ alloy. The Shockley states of clean noble metals with their weak lattice potential show free-electron-like behavior and thus a circular Fermi surface. The stronger effect of the lattice in the alloy is the result of the more anisotropic ionic charge distribution within the surface plane, where each Sb atom “sees” six Ag nearest neighbors and six Sb next-nearest neighbors with an inequivalent ionic potential. This anisotropy, only partially screened by the valence electrons, is indeed at the origin of the in-plane gradient, which contributes to the SO splitting.

IV. CONCLUSIONS

In summary, we have studied the electronic structure of the SbAg₂ surface alloy. We found obvious similarities with the bands of the isostructural BiAg₂ and PbAg₂ alloys, but a much smaller SO splitting and a non-rigid band shift in wave vector even for k values close to $\bar{\Gamma}$. The experimental data are well reproduced by first-principles relativistic calculations. These results indicate that large in-plane potential gradient, which plays a crucial role in the BiAg₂ surface alloy, is ineffective in producing a large SO splitting unless supported by a strong atomic SO interaction of one of the alloy constituents. On the other hand, the band splitting is not simply proportional to the relevant atomic SO parameter. More data on other surface alloys, grown on different substrates, are necessary to further clarify the interplay of atomic and structural parameters.

ACKNOWLEDGMENTS

M.G. kindly acknowledges clarifying discussions with G. Bihlmayer. This work was supported by the Swiss National Science Foundation and by the MaNEP NCCR. The Synchrotron Radiation Center is funded by the National Science Foundation under Award No. DMR-0537588. A.B. thanks the Alexander von Humboldt Foundation for financial support.

¹Y. A. Bychkov and E. I. Rashba, JETP Lett. **39**, 78 (1984).

²R. Winkler, *Spin-orbit Coupling Effects in Two-dimensional Electron and Hole Systems* (Springer, New York, 2003).

³S. LaShell, B. A. McDougall, and E. Jensen, Phys. Rev. Lett. **77**, 3419 (1996).

⁴G. Nicolay, F. Reinert, S. Hüfner, and P. Blaha, Phys. Rev. B **65**, 033407 (2001).

⁵M. Hoesch, M. Muntwiler, V. N. Petrov, M. Hengsberger, L. Patthey, M. Shi, M. Falub, T. Greber, and J. Osterwalder, Phys. Rev. B **69**, 241401(R) (2004).

⁶Y. M. Koroteev, G. Bihlmayer, J. E. Gayone, E. V. Chulkov, S. Blügel, P. M. Echenique, and P. Hofmann, Phys. Rev. Lett. **93**,

046403 (2004).

⁷K. Sugawara, T. Sato, S. Souma, T. Takahashi, M. Arai, and T. Sasaki, Phys. Rev. Lett. **96**, 046411 (2006).

⁸T. Hirahara, T. Nagao, I. Matsuda, G. Bihlmayer, E. V. Chulkov, Y. M. Koroteev, P. M. Echenique, M. Saito, and S. Hasegawa, Phys. Rev. Lett. **97**, 146803 (2006).

⁹E. Rotenberg, J. W. Chung, and S. D. Kevan, Phys. Rev. Lett. **82**, 4066 (1999).

¹⁰M. Hochstrasser, J. G. Tobin, E. Rotenberg, and S. D. Kevan, Phys. Rev. Lett. **89**, 216802 (2002).

¹¹A. M. Shikin, A. Varykhalov, G. V. Prudnikova, D. Usachev, V. K. Adamchuk, Y. Yamada, J. Riley, and O. Rader, Phys. Rev.

- Lett. **100**, 057601 (2008).
- ¹²Y. S. Dedkov, M. Fonin, U. Rüdiger, and C. Laubschat, Phys. Rev. Lett. **100**, 107602 (2008).
- ¹³O. Krupin, G. Bihlmayer, K. Starke, S. Gorovikov, J. E. Prieto, K. Döbrich, S. Blügel, and G. Kaindl, Phys. Rev. B **71**, 201403(R) (2005).
- ¹⁴H. Cercellier, C. Didiot, Y. Fagot-Revurat, B. Kierren, L. Moreau, D. Malterre, and F. Reinert, Phys. Rev. B **73**, 195413 (2006).
- ¹⁵I. Barke, F. Zheng, T. K. Rügheimer, and F. J. Himpsel, Phys. Rev. Lett. **97**, 226405 (2006).
- ¹⁶C. R. Ast, J. Henk, A. Ernst, L. Moreschini, M. C. Falub, D. Pacilé, P. Bruno, K. Kern, and M. Grioni, Phys. Rev. Lett. **98**, 186807 (2007).
- ¹⁷D. Pacilé, C. R. Ast, M. Papagno, C. Da Silva, L. Moreschini, M. Falub, A. P. Seitsonen, and M. Grioni, Phys. Rev. B **73**, 245429 (2006).
- ¹⁸C. R. Ast *et al.*, Phys. Rev. B **77**, 081407(R) (2008).
- ¹⁹G. Bihlmayer, S. Blügel, and E. V. Chulkov, Phys. Rev. B **75**, 195414 (2007).
- ²⁰L. Petersen and P. Hedegård, Surf. Sci. **459**, 49 (2000).
- ²¹G. Bihlmayer, Y. M. Koroteev, P. M. Echenique, E. V. Chulkov, and S. Blügel, Surf. Sci. **600**, 3888 (2006).
- ²²F. Forster, S. Hufner, and F. Reinert, J. Phys. Chem. B **108**, 14692 (2004).
- ²³K. Wittel and R. Manne, Theor. Chim. Acta **33**, 347 (1974).
- ²⁴J. Prempfer, M. Trautmann, J. Henk, and P. Bruno, Phys. Rev. B **76**, 073310 (2007).
- ²⁵F. Meier, H. Dil, J. Lobo-Checa, L. Patthey, and J. Osterwalder, Phys. Rev. B **77**, 165431 (2008).
- ²⁶S. A. de Vries, W. J. Huisman, P. Goettkindt, M. J. Zwanenburg, S. L. Bennett, I. K. Robinson, and E. Vlieg, Surf. Sci. **414**, 159 (1998).
- ²⁷E. A. Soares, C. Bittencourt, V. B. Nascimento, V. E. de Carvalho, C. M. C. de Castilho, C. F. McConville, A. V. de Carvalho, and D. P. Woodruff, Phys. Rev. B **61**, 13983 (2000).
- ²⁸P. D. Quinn, D. Brown, D. P. Woodruff, P. Bailey, and T. C. Q. Noakes, Surf. Sci. **511**, 43 (2002).
- ²⁹J. Henk, in *Handbook of Thin Film Materials*, edited by H. S. Nalwa (Academic, San Diego, 2001), Vol. 2, Chap. 10, p. 479.
- ³⁰Other calculations give a much higher value (0.85 Å) for the Bi relaxation in Bi/Ag(111) (Ref. 19). Nevertheless, the same reference gives a Pb relaxation in Pb/Ag(111) consistently higher than that observed experimentally [J. Dalmás, H. Oughaddou, C. Leandri, J. M. Gay, G. Le Gay, G. Treglia, B. Aufray, O. Bunk, and R. L. Johnson, Phys. Rev. B **72**, 155424 (2005)].

Paper II

Tuning independently the Fermi energy and spin splitting in
Rashba systems: Ternary surface alloys on Ag(111)

Tuning independently Fermi energy and spin splitting in Rashba systems: Ternary surface alloys on Ag(111)

H Mirhosseini, A Ernst, S Ostanin, and J Henk

Max-Planck-Institut für Mikrostrukturphysik, Weinberg 2, D-06120 Halle (Saale), Germany

E-mail: hossein@mpi-halle.de (H Mirhosseini)

PACS numbers: 71.70.Ej, 73.20.At, 71.15.Mb

Abstract. By detailed first-principles calculations we show that the Fermi energy and the Rashba splitting in disordered ternary surface alloys $\text{Bi}_x\text{Pb}_y\text{Sb}_{1-x-y}/\text{Ag}(111)$ can be independently tuned by choosing the concentrations x and y of Bi and Pb, respectively. The findings are explained by three fundamental mechanisms, namely the relaxation of the adatoms, the strength of the atomic spin-orbit coupling, and band filling. By mapping the Rashba characteristics, i.e. the splitting k_{R} and the Rashba energy E_{R} , and the Fermi energy of the surface states in the complete range of concentrations, we find that these quantities depend monotonically on x and y , with a very few exceptions. Our results suggest to investigate experimentally effects which rely on the Rashba spin-orbit coupling in dependence on spin-orbit splitting and band filling.

1. Introduction

In the emerging field of spin electronics, proposed device applications often utilize the Rashba effect [1] in a two-dimensional electron gas (2DEG). A prominent example is the spin field-effect transistor [2] in which the spin-orbit (SO) interaction in the 2DEG is controlled via a gate voltage [3, 4]. Other examples are a high critical superconducting temperature which shows up in materials with a sizable spin-orbit interaction [5] and the spin Hall effect [6–9].

The Rashba effect relies on breaking the inversion symmetry of the system and, consequently, shows up in semiconductor heterostructures and at surfaces. The breaking of the inversion symmetry results—via the spin-orbit coupling—in a splitting in the dispersion relation of electronic states which are confined to the interface [1]. In a simple model for a two-dimensional electron gas, a potential in z direction confines the electrons to the xy plane. The Hamiltonian of the spin-orbit coupling can thus be written as

$$\hat{H}_{\text{so}} = \gamma_{\text{R}}(\sigma_x \partial_y - \sigma_y \partial_x), \quad (1)$$

where the strength of the SO interaction is quantified by the Rashba parameter γ_{R} . Employing a plane-wave *ansatz* yields the dispersion relation

$$E_{\pm}(\vec{k}_{\parallel}) = E_0 + \frac{\hbar^2 k_{\parallel}^2}{2m^*} \pm \gamma_{\text{R}} |\vec{k}_{\parallel}|, \quad (2)$$

where m^* is the effective electron mass. The split electronic states are labeled by $+$ and $-$; their spins lie within the xy plane, are aligned in opposite directions, and are perpendicular to the wave vector \vec{k}_{\parallel} .

In a real system, the Rashba parameter γ_{R} comprises effectively two contributions [10]. The ‘atomic’ contribution is due to the strong potential of the ions (atomic spin-orbit coupling). The ‘confinement’ contribution is due to the structural inversion asymmetry which can be viewed as the gradient of the confinement potential in z direction. The larger this gradient and the atomic spin-orbit parameter, the larger γ_{R} and the splitting

$$k_{\text{R}} = \frac{|m^*| \gamma_{\text{R}}}{\hbar^2}, \quad (3)$$

which is defined as the shift of the band extremum off the Brillouin zone center ($\vec{k}_{\parallel} = 0$). Another quantification of the splitting is the Rashba energy

$$E_{\text{R}} = -\frac{\hbar^2 k_{\text{R}}^2}{2m^*} = -\frac{m^* \gamma_{\text{R}}^2}{2\hbar^2}, \quad (4)$$

that is the energy of the band extremum with respect to the energy E_0 for which the bands cross at $\vec{k}_{\parallel} = 0$.

The above dispersion relation suggests to distinguish two energy ranges. Region I is defined as the energy range between E_0 and the band extrema ($E \in [E_0 - E_{\text{R}}, E_0]$ for positive m^* or $E \in [E_0, E_0 + E_{\text{R}}]$ for negative m^*) [11]. Region II comprises the other range of band energies ($E > E_0$ for positive m^* or $E < E_0$ for negative m^*). The

density of states in region I is singular at the band extrema and decreases towards E_0 while in region II it is constant.

In view of designing device applications and investigating fundamental effects, it is desirable to tune both the strength γ_R of the Rashba spin-orbit coupling and the Fermi energy E_F of the 2DEG. In a semiconductor heterostructure, this can be achieved by an external gate voltage and by doping of the semiconductor host materials. At a surface, these quantities can be affected by adsorption of adatoms [12,13], by surface alloying [11], and by changing the thickness of buffer layers (e. g. in Bi/(Ag) $_n$ /Si(111) [14]). Recently, a ferroelectric control has been proposed [15].

Surface states in surface alloys show an unmatched Rashba splitting [16], as has been investigated in detail by scanning tunneling microscopy as well as by spin- and angle-resolved photoelectron spectroscopy. They are convenient systems for testing fundamental Rashba-based effects. The ordered surface alloys Bi/Ag(111), Pb/Ag(111), and Sb/Ag(111) have been investigated by first-principles calculations and in experiments [16–18]. These three systems differ with respect to their Rashba characteristics k_R and E_R , and by E_0 . The challenge we are dealing with is how to tune these properties *independently*.

The basic idea is as follows. Bi/Ag(111) has a large splitting and occupied sp_z surface states, while Pb/Ag(111) has a large splitting and unoccupied sp_z surface states. In a disordered binary alloy Bi $_x$ Pb $_{1-x}$ /Ag(111) the Fermi energy can be tuned by the concentration x , while keeping a large spin splitting. In contrast, Sb/Ag(111) has occupied surface states with almost the same binding energy as those in Bi/Ag(111) but a minor splitting. This allows to tune mainly the spin splitting but keeping the Fermi energy in Bi $_x$ Sb $_{1-x}$ /Ag(111). Thus, by an appropriate choice of concentrations x and y in a ternary alloy Bi $_x$ Pb $_y$ Sb $_{1-x-y}$ /Ag(111) we expect to tune the Fermi energy and the splitting *independently*. In particular, one could access the region I between E_0 and the band maxima which is important for high-temperature superconductivity [5].

We report on a first-principles investigation of disordered surface alloys Bi $_x$ Pb $_y$ Sb $_{1-x-y}$ /Ag(111), performed along the successful line of our previous works on both ordered and disordered alloys [11,16,18]. Since all ordered and disordered binary alloys show a $\sqrt{3} \times \sqrt{3}R30^\circ$ surface reconstruction, we assume this geometry also for the ternary alloys. The resulting substitutional disorder is described within the coherent potential approximation.

The paper is organized as follows. Our computational approach is sketched in section 2. The results are discussed in section 3, for binary alloys in section 3.4 and for ternary alloys in section 3.5. We give conclusions in section 4.

2. Computational aspects

We rely on our successful multi-code approach, based on the local density approximation to density functional theory. Because this is described in detail elsewhere [15], we deliberately sketch it in this paper.

The surface relaxations of ordered surface alloys were determined using the Vienna *Ab-initio* Simulation Package (VASP) [19], well-known for providing precise total energies and forces. The relaxed structural parameters serve as input for first-principles multiple-scattering calculations. Our Korringa-Kohn-Rostoker (KKR) method already proved successful for relativistic electronic-structure computations of Rashba systems [14, 20].

The central quantity in multiple-scattering theory is the Green function [21]

$$G(\vec{r}_n, \vec{r}'_m; E, \vec{k}) = \sum_{\Lambda\Lambda'} Z_{\Lambda}^n(\vec{r}_n; E) \tau_{\Lambda\Lambda'}^{nm}(E, \vec{k}) Z_{\Lambda'}^m(\vec{r}'_m; E)^* - \delta^{nm} \sum_{\Lambda} Z_{\Lambda}^n(\vec{r}_{<}; E) J_{\Lambda}^n(\vec{r}_{>}; E)^*, \quad (5)$$

where Z and J are regular and irregular scattering solutions of sites n and m at energy E and wavevector \vec{k} , respectively. \vec{r}_n is taken with respect to the position \vec{R}_n of site n ($\vec{r}_n = \vec{r} - \vec{R}_n$). $r_{<}$ ($r_{>}$) is the lesser (larger) of r_n and r'_m . $\Lambda = (\kappa, \mu)$ comprises the relativistic spin-angular-momentum quantum numbers [21]. The scattering-path operator τ is obtained in standard KKR from the so-called KKR equation [21], or in layer-KKR from the Dyson equation for the Green function [22].

The local electronic structure is analyzed in terms of the spectral density

$$N^n(E; \vec{k}) = -\frac{1}{\pi} \Im \text{Tr} G(\vec{r}_n, \vec{r}_n; E, \vec{k}). \quad (6)$$

By taking appropriate decompositions of the trace, the spectral density provides information on spin polarization and orbital composition of the electronic states.

Substitutional ternary alloys $\text{Bi}_x\text{Pb}_y\text{Sb}_{1-x-y}/\text{Ag}(111)$ are described within the coherent potential approximation (KKR-CPA), in which short-range order is neglected. From the agreement of the theoretical data with their experimental counterparts for the binary alloys $\text{Bi}_x\text{Pb}_{1-x}/\text{Ag}(111)$ [11], we conclude that short-range order is of minor importance in these systems. Hence, we applied the KKR-CPA also for the ternary alloys.

The effect of the disorder can be understood as a self-energy [23]. As a consequence, the spectral density of the disordered alloys becomes blurred (or smeared out) as compared to that of the ordered alloys.

3. Results and discussion

3.1. Geometry

Relaxations have been determined by VASP for the ordered alloys, with $\sqrt{3} \times \sqrt{3}R30^\circ$ reconstruction and face-centered-cubic (fcc) stacking (VASP cannot treat substitutional disorder within the CPA). It turns out that the relaxations of Sb, Bi, and Pb are in accord with their atomic radii. To be more precise, the outward relaxations are 9.6, 15, and 18 percent of the Ag(111) bulk interlayer spacing (2.33 Å), respectively, with respect to the positions of the Ag atoms in the topmost layer. Being negligibly small, in-plane displacements of Ag atoms are not considered.

Since all ordered and disordered binary alloys show a $\sqrt{3} \times \sqrt{3}R30^\circ$ surface reconstruction, we assume this geometry also for the ternary alloys. The relaxations of the disordered surface alloys were linearly interpolated, in dependence on the concentrations of the constituting elements Bi, Pb, and Sb. This assumption is within the spirit of the CPA; being a mean-field theory, a disordered system is described by an effective medium. Likewise the relaxation should be taken as a concentration-weighted average. We are aware, however, that in real samples, the relaxations of the constituting individual atoms could differ, as might be checked by scanning tunneling microscopy.

3.2. Mechanisms which influence the Rashba-split surface states

Before presenting details of our calculations, a brief discussion of the general trends and mechanisms is in order. For tuning the Fermi energy and spin splitting independently, the underlying mechanisms should be independent as well.

A first mechanism is relaxation. The outward relaxations of Sb, Pb, and Bi are in accord with their atomic radii; the larger the atomic radius, the larger the outward relaxation. The relaxation is accompanied by a charge transfer from the atomic sphere to the surrounding; the larger the relaxation, the larger the charge transfer [24]. This mechanism determines the energy position of the degenerate point E_0 —cf. (2)—and, consequently, the Fermi energy or band-filling of the surface states (2DEG).

A second mechanism is the atomic spin-orbit parameter. Bi and Pb are heavy elements with large SO parameter (1.25 eV for Bi and 0.91 eV for Pb [25]), in contrast to the lighter element Sb (0.4 eV [25]). The Rashba splitting depends both on the atomic SO-coupling strength and the potential gradient [10]. Since the latter should not differ considerably among the considered systems, the spin splitting is mainly determined by the atomic SO coupling. We expect that with increasing Sb content, the spin splitting decreases.

A third mechanism is electron doping or band filling. Pb has one electron less than Bi ($Z_{\text{Pb}} = 82$, $Z_{\text{Bi}} = 83$). Within a rigid-band model, the surface states in Pb/Ag(111) are shifted to higher energies, as compared to those in Bi/Ag(111). This picture is confirmed by experiments and first-principles calculations [11].

3.3. Ordered surface alloys

The ordered surface alloys Bi/Ag(111), Pb/Ag(111), and Sb/Ag(111) have been studied previously in detail [16–18]. They show two sets of surface states; a first set is unoccupied and consists mainly of $p_x p_y$ orbitals (for Bi/Cu(111), see [26]). In this paper, we focus on the other set which is either completely or partially occupied and consists of sp_z orbitals. The effective mass m^* of both sets is negative, implying a negative dispersion.

Sb/Ag(111). We address briefly the abovementioned relaxation mechanism by considering two cases for Sb/Ag(111): (i) an Sb relaxation as calculated by VASP

(9.6 %) and (ii) an artificial relaxation of 25 %. The charge transfer from the Sb muffin-tin spheres to the surrounding is increased for the larger relaxation (2.05 % as compared to 0.94 %, with respect to the nominal valence charge; cf. [24]). Consequently, the surface states are shifted towards higher energies by 0.16 eV, as obtained from the degeneracy point E_0 . Further, the spin splitting k_R becomes increased as well (0.03 \AA^{-1} as compared to 0.02 \AA^{-1}). This corroborates that the relaxation mainly affects the crossing point E_0 (or Fermi energy) rather than the spin splitting.

3.4. Disordered binary alloys

Bi_xPb_{1-x}/Ag(111). In the disordered binary alloy Bi_xPb_{1-x}/Ag(111), which has been studied previously [11], the ratio of the Rashba energy E_R and the Fermi energy E_F can be chosen within a wide range, in dependence on the Bi concentration x . For both Bi and Pb, 0.99 % of the atomic charge atom is removed from the muffin-tin sphere, which is in agreement with the close outward relaxation of Bi and Pb (15 % and 18 %). As noted before, Pb has one valence electron less than Bi, which explains the sizable shift of the surface states to higher energies (band-filling mechanism; cf. the panels on the right-hand side of figure 1). Although the relaxation is of the same order, the splitting is smaller for Pb (topmost panel in figure 1). This can be attributed to the smaller atomic spin-orbit parameter of Pb (0.91 eV for Pb and 1.25 eV for Bi [25]).

Bi_xSb_{1-x}/Ag(111). Recently, the surface states of the disordered binary alloys Bi_xSb_{1-x}/Ag(111) were mapped out by angle-resolved photoelectron spectroscopy. The momentum offset k_R evolves continuously with increasing Bi concentration x . The splitting decreases sizably for $x < 0.50$ [27].

In theory, the outward relaxation of Bi is larger than for Sb (15 % and 9.6 %, respectively). Consequently the charge which is removed from the Sb sphere (0.94 %) is smaller than that of Bi (0.99 %). Since Bi and Sb are iso-electronic, with valence-shell configuration $5p^3$ and $6p^3$, E_0 remains almost unaffected by x , as can be seen in the bottom row of figure 1. The spin splitting for Sb is much less than for Bi, in agreement with the atomic spin-orbit parameter (0.4 eV and 1.25 eV). In accord with experimental results, the Rashba splitting k_R evolves with Bi concentration x .

To elucidate further the effect of the relaxation, we calculated the splitting of Bi_{0.6}Sb_{0.4}/Ag(111) for two relaxations. The interpolated relaxation for Bi_{0.6}Sb_{0.4}/Ag(111) is 12.8 % (shown at $(x, y, z) = (0.6, 0.4, 0.0)$ in figure 1), for the artificial relaxed system the outward relaxation is taken as 19 % (not shown here). The charge transfer for the two systems is very close, and the difference in the splitting is negligibly small. Hence, the splitting is negligibly sensitive to the relaxation, as was already established for Sb/Ag(111).

Pb_ySb_{1-y}/Ag(111). To complete the picture of the binary alloys we turn to Pb_ySb_{1-y}/Ag(111), for which experimental results are not available. The trends which

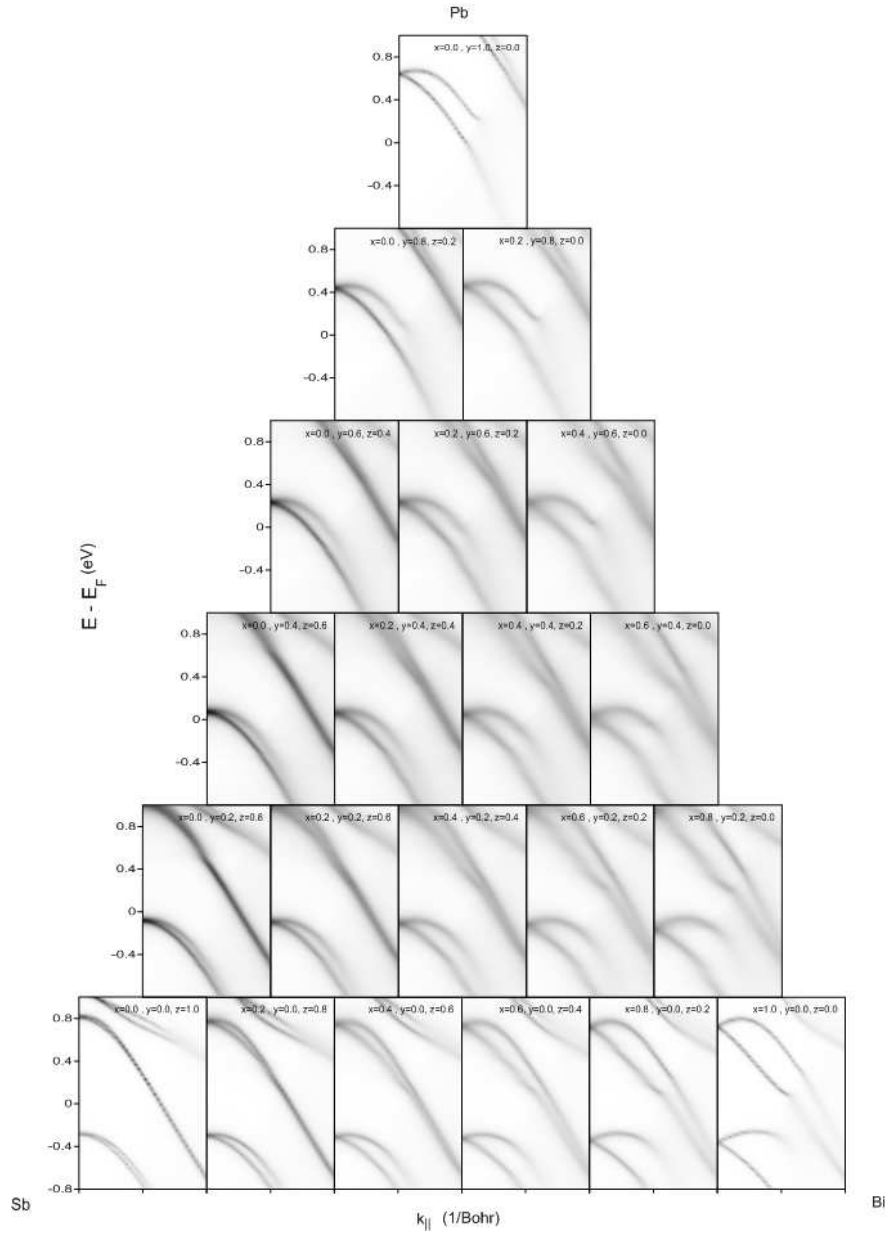


Figure 1. Surface states of disordered ternary alloys $\text{Bi}_x\text{Pb}_y\text{Sb}_{1-x-y}/\text{Ag}(111)$ along $\bar{\Gamma}-\bar{K}$ of the two-dimensional Brillouin zone. The spectral density at a heavy-element site $\text{Bi}_x\text{Pb}_y\text{Sb}_{1-x-y}$ is depicted as linear gray scale, with dark gray corresponding to high spectral weight; cf. (6).

have been discussed before are as well found in these alloys (cf. the panels on the left-hand side of figure 1). As the Pb concentration increases, E_0 shifts down from $E_F + 0.6$ eV to $E_F - 0.4$ eV, implying that the surface states become completely filled at about $y = 0.3$. As for $\text{Bi}_x\text{Sb}_{1-x}/\text{Ag}(111)$, the spin splitting increases with y .

3.5. Disordered ternary alloys $\text{Bi}_x\text{Pb}_y\text{Sb}_{1-x-y}/\text{Ag}(111)$

Having established the ingredients which are necessary for independently tuning the Fermi energy and the spin splitting in the surface alloys—by investigating the disordered binary surface alloys—we now mix them to disordered ternary alloys $\text{Bi}_x\text{Pb}_y\text{Sb}_{1-x-y}/\text{Ag}(111)$. By choosing appropriate concentrations x and y , the degeneracy point E_0 and the Rashba splitting are tuned. Note that the splitting k_R and the Rashba energy E_R are not fully independent; both can be expressed (in a free-electron model) in terms of the effective electron mass and the Rashba parameter [cf. (3) and (4)].

In figure 1 the surface-state dispersions of ternary alloys $\text{Bi}_x\text{Pb}_y\text{Sb}_{1-x-y}/\text{Ag}(111)$ are shown. The concentrations x and y have been varied in steps of 0.2. A common feature of the spectral density of the binary and ternary alloys is a finite lifetime of the spectral density, which is the consequence of the substitutional disorder.

The Rashba characteristic of the ternary alloys follow the general trends of the binary alloys which have been discussed before. In the ternary alloys with larger outward relaxation (i. e. the Bi- and Pb-rich compounds), the degenerate point E_0 shifts toward higher energies (main mechanism: relaxation). The larger the concentration of heavy elements Bi and Pb as compared to the Sb concentration, the larger the splitting k_R (main mechanism: atomic spin-orbit parameter). The degenerate point E_0 shifts upward with increasing Pb concentration (main mechanism: band filling).

The shift k_R of the surface states in reciprocal space versus concentrations x and y is shown in figure 2 (top). As expected, the smallest splitting (dark blue) shows up for $\text{Sb}/\text{Ag}(111)$ ($z = 1 - x - y = 1$), while the largest (dark red) corresponds to $\text{Bi}/\text{Ag}(111)$ ($x = 1$). For $\text{Pb}/\text{Ag}(111)$, k_R is of intermediate order (green/yellow). Surprisingly, the splitting is not monotonic, as one might have expected in a rigid-band picture. For example, k_R shows a local minimum at $(x, y, z) \approx (0.4, 0.4, 0.2)$.

As k_R , the Rashba energy E_R depends monotonously in a large range of concentrations (bottom in figure 2). Sizable Rashba energies are found mainly for Bi-rich alloys, say for $x > 0.5$. This implies that for accessing region I, Bi-rich surface alloys are inevitable. For smaller x (blue areas in the bottom panel of figure 2), the energy range of region I could be too small to be employed in experiments.

The energy E_0 of the degeneracy point depends almost linearly on the heavy elements' concentrations x and y (figure 3). For equal Bi and Sb concentrations ($x = z$) it is nearly constant; upon adding Pb, E_0 shifts up. For systems with about 40% of Pb concentration, E_0 is very close to the Fermi level E_F , so that the latter lies in region I [24].

In summary, the above results support that both Fermi energy and spin splitting in the surface states can be tuned independently, as is readily apparent from the different shapes in figure 2 and figure 3. A very interesting region in the ternary plots is around $(x, y, z) \approx (0.6, 0.3, 0.1)$, where the degenerate point E_0 and the Fermi energy E_F coincide. Keeping the Sb concentration constant and changing the Pb concentration of about 10% is accompanied by transition between region I and region II, while k_R and E_R are almost constant. It is also possible to tune E_R and k_R while keeping the position of degenerate point constant. The changes of k_R and E_R are not independent but k_R depends more sensitive on the concentrations than E_R .

4. Conclusions

Disordered ternary surface alloys $\text{Bi}_x\text{Pb}_y\text{Sb}_{1-x-y}/\text{Ag}(111)$ allow to fabricate a two-dimensional electron gas with specific Rashba spin-orbit splitting and Fermi energy

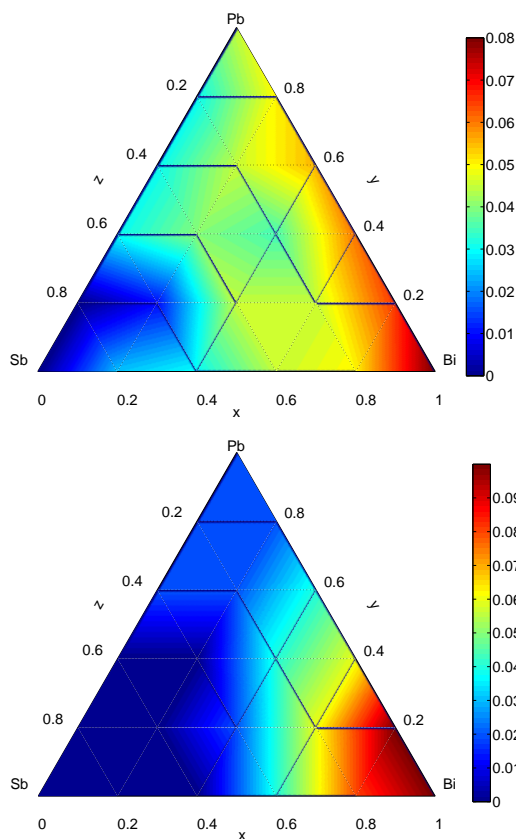


Figure 2. Spin splitting in disordered ternary alloys $\text{Bi}_x\text{Pb}_y\text{Sb}_{1-x-y}/\text{Ag}(111)$. Top: The surface-state displacement k_R (in reciprocal space) is depicted as color scale as a function of Bi concentration x , Pb concentration y , and Sb concentration $z = 1 - x - y$. The color bar on the right is in units of \AA^{-1} . Bottom: Same as in the top but for the Rashba energy E_R . The color bar is in eV.

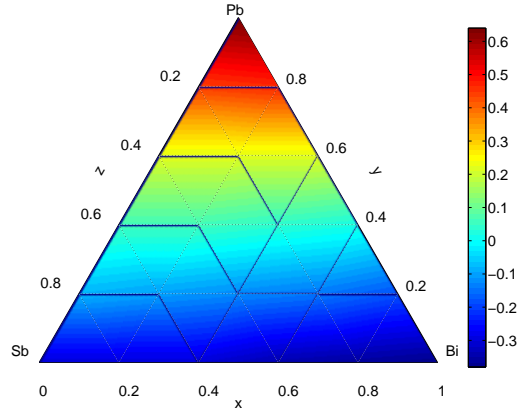


Figure 3. Surface-state energy in disordered ternary alloys $\text{Bi}_x\text{Pb}_y\text{Sb}_{1-x-y}/\text{Ag}(111)$. The degeneracy energy E_0 of the surface state, with respect to the Fermi level E_F , is depicted as color scale as a function of Bi concentration x , Pb concentration y , and Sb concentration $z = 1 - x - y$. The color bar on the right is in eV. At negative energies, the surface states are fully occupied (blue area).

which can be investigated by surface-scientific methods (scanning tunneling probes and especially photoelectron spectroscopy). In particular, the important transition from energy region I (that is, the Fermi energy E_F lies above the degeneracy point E_0) to region II (E_F below E_0) can be studied for different strengths of the Rashba spin-orbit coupling. Thus, the present study may stimulate further experiments on Rashba systems and their unique properties.

5. Acknowledgment

We gratefully acknowledge very fruitful discussions with Christian Ast, Hugo J Dil, Isabella Gierz, and Fabian Meier.

References

- [1] Yu. A. Bychkov and É. I. Rashba. Properties of a 2D electron gas with lifted degeneracy. *Sov. Phys. JETP Lett.*, 39:78, 1984. Translated from Ref. Bychkov84c.
- [2] S. Datta and B. Das. Electronic analogue of the electronic modulator. *Appl. Phys. Lett.*, 56(7):665, 1990.
- [3] J. Nitta, T. Akazaki, H. Takayanagi, and T. Enoki. Gate control of spin-orbit interaction in an inverted $\text{In}_{0.53}\text{Ga}_{0.47}\text{As}/\text{In}_{0.52}\text{Al}_{0.48}\text{As}$ heterostructure. *Phys. Rev. Lett.*, 78:1335, 1997.
- [4] Takaaki Koga, Junsaku Nitta, Hideaki Takayanagi, and Supriyo Datta. Spin-filter device based on the Rashba effect using a nonmagnetic resonant tunneling diode. *Phys. Rev. Lett.*, 88:126601, 2002.
- [5] E. Cappelluti, C. Grimaldi, and F. Marsiglio. Topological change of the Fermi surface in low-density Rashba gases: Application to superconductivity. *Phys. Rev. Lett.*, 98:167002, 2007.
- [6] J. E. Hirsch. Spin hall effect. *Phys. Rev. Lett.*, 83(9):1834, 1999.
- [7] Y. Kato, R. C. Myers, A. C. Gossard, and D. D. Awschalom. Coherent spin manipulation without magnetic fields in strained semiconductors. *Nature*, 427:50, 2004.

- [8] D. S. Saraga and D. Loss. Fermi liquid parameters in two dimensions with spin-orbit interaction. *Phys. Rev. B*, 72:195319, 2005.
- [9] S. O. Valenzuela and M. Tinkham. Direct electronic measurement of the spin hall effect. *Nature*, 442:176, 2006.
- [10] L. Petersen and P. Hedegård. A simple tight-binding model of spin-orbit splitting of *sp*-derived surface states. *Surf. Sci.*, 459:49, 2000.
- [11] C. R. Ast, D. Pacilé and L. Moreschini, M. C. Falub, M. Papagno, K. Kern, M. Grioni, J. Henk, A. Ernst, S. Ostanin, and P. Bruno. Spin-orbit split two-dimensional electron gas with tunable Rashba and Fermi energy. *Phys. Rev. B*, 77:081407(R), 2008.
- [12] F. Forster, S. Hüfner, and F. Reinert. Rare gases on noble-metal surfaces: An angle-resolved photoemission study with high energy resolution. *J. Phys. Chem. B*, 108:14692, 2004.
- [13] L. Moreschini, A. Bendounan, C. R. Ast, F. Reinert, M. Falub, and M. Grioni. Effect of rare-gas adsorption on the spin-orbit split bands of a surface alloy: Xe on Ag(111)-($\sqrt{3} \times \sqrt{3}$)R30°-Bi. *Phys. Rev. B*, 77:115407, 2008.
- [14] Emmanouil Frantzeskakis, Stéphane Pons, Hossein Mirhosseini, Jürgen Henk, Christian R. Ast, and Marco Grioni. Tunable spin gaps in a quantum-confined geometry. *Phys. Rev. Lett.*, 101(19):196805, Nov 2008.
- [15] H. Mirhosseini, I. V. Maznichenko, S. Abdelouahed, S. Ostanin, A. Ernst, I. Mertig, and J. Henk. Toward a ferroelectric control of rashba spin-orbit coupling: Bi on *batio3*(001) from first principles. *Phys. Rev. B*, 81(7):073406, Feb 2010.
- [16] Chr. R. Ast, J. Henk, A. Ernst, L. Moreschini, M. C. Falub, D. Pacilé, P. Bruno, K. Kern, and M. Grioni. Giant spin splitting through surface alloying. *Phys. Rev. Lett.*, 98:186807, 2007.
- [17] G. Bihlmayer, S. Blügel, and E. V. Chulkov. Enhanced Rashba spin-orbit splitting in Bi/Ag(111) and Pb/Ag(111) surface alloys. *Phys. Rev. B*, 75:195414, 2007.
- [18] L. Moreschini, A. Bendounan, I. Gierz, C. A. Ast, H. Mirhosseini, H. Höchst, K. Kern, J. Henk, A. Ernst, S. Ostanin, F. Reinert, and M. Grioni. Assessing the atomic contribution to the rashba spin-orbit splitting in surface alloys: Sb/ag(111). *Phys. Rev. B*, 79:075424, 2009.
- [19] G. Kresse and J. Furthmüller. Efficient iterative schemes for *ab initio* total-energy calculations using a plane-wave basis set. *Phys. Rev. B*, 54:11169, 1996.
- [20] J. Henk, A. Ernst, and P. Bruno. Spin polarization of the *L*-gap surface states on Au(111): A first-principles investigation. *Surf. Sci.*, 566–568:482, 2004.
- [21] J. Zabloudil, R. Hammerling, L. Szunyogh, and P. Weinberger, editors. *Electron Scattering in Solid Matter*. Springer, Berlin, 2005.
- [22] J. Henk. Theory of low-energy diffraction and photoelectron spectroscopy from ultra-thin films. In H. S. Nalwa, editor, *Handbook of Thin Film Materials*, volume 2, chapter 10, page 479. Academic Press, San Diego, 2001.
- [23] P. Weinberger. *Electron Scattering Theory of Ordered and Disordered Matter*. Clarendon Press, Oxford, 1990.
- [24] L. Moreschini, A. Bendounan, H. Bentmann, M. Assig, K. Kern, F. Reinert J. Henk, C. R. Ast, and M. Grioni. Influence of the substrate on the spin-orbit splitting in surface alloys on (111) noble-metal surfaces. *Phys. Rev. B*, 80:035438, 2009.
- [25] K. Wittel and R. Manne. Accurate calculation of ground-state energies in an analytic Lanczos expansion. *Theor. chim. Acta.*, 33:347, 1974.
- [26] H. Mirhosseini, J. Henk, A. Ernst, S. Ostanin, C.-T. Chiang, P. Yu, A. Winkelmann, and J. Kirschner. Unconventional spin topology in surface alloys with rashba-type spin splitting. *Phys. Rev. B*, 79(24):245428, Jun 2009.
- [27] C. R. Ast, H. J. Dil, I. Gierz, and F. Meier. private communication.

Paper III

Unconventional spin topology in surface alloys with Rashba-type
spin splitting



Unconventional spin topology in surface alloys with Rashba-type spin splitting

H. Mirhosseini, J. Henk,* A. Ernst, S. Ostanin, C.-T. Chiang, P. Yu, A. Winkelmann, and J. Kirschner
 Max-Planck-Institut für Mikrostrukturphysik, Weinberg 2, D-06120 Halle (Saale), Germany

(Received 4 May 2009; published 24 June 2009)

The spins of a pair of spin-orbit split surface states at a metal surface are usually antiparallely aligned, in accord with the Rashba model for a two-dimensional electron gas. By first-principles calculations and two-photon photoemission experiments we provide evidence that in the surface alloy Bi/Cu(111) the spins of an unoccupied pair of surface states are parallelly aligned. This unconventional spin polarization, which is not consistent with that imposed by the Rashba model, is explained by hybridization of surface states with different orbital character and is attributed to the spin-orbit interaction. Since hybridization is a fundamental effect our findings are relevant for spin electronics in general.

DOI: 10.1103/PhysRevB.79.245428

PACS number(s): 73.20.At, 71.70.Ej, 79.60.Dp

I. INTRODUCTION

In the emerging field of spin electronics, proposals for device applications often utilize the Rashba effect in a two-dimensional electron gas (2DEG),¹ thereby relying on the spin topology of the 2DEG's electronic states (e.g., Refs. 2–6). The structural inversion asymmetry, that is, the asymmetric confinement of the 2DEG, leads via spin-orbit (SO) interaction to a splitting in the dispersion relation of the free electrons,

$$\epsilon_{\pm}(\mathbf{k}) = \epsilon_0 + \frac{\hbar^2 \mathbf{k}^2}{2m^*} \pm \alpha |\mathbf{k}|, \quad \mathbf{k} = (k_x, k_y), \quad (1)$$

where m^* is the effective mass. The Rashba parameter α comprises the strength of the atomic SO interaction and of the gradient of the confining potential in the z direction.^{7,8} The splitting, quantified by the displacement $\Delta k = 2|\alpha m^*|/\hbar^2$ of the band extrema in reciprocal space, shows up as two concentric circles in the momentum distribution. The spins of the two electronic states at energy ϵ are (i) oppositely aligned, are (ii) lying within the xy plane, and are (iii) normal to the wave vector \mathbf{k} .⁹ The spin polarization can therefore be written as $\mathbf{P}_{\pm}(\mathbf{k}) = \pm (k_y, -k_x, 0)/|\mathbf{k}|$, implying also $|\mathbf{P}|=100\%$ [Fig. 1(a)].¹⁰

The above paradigmatic spin topology is found to a large extent in semiconductor heterojunctions¹¹ and in surface states at (111) surfaces of noble metals, in particular in Au(111).^{12,13} The surface states in surface alloys such as Bi/Ag(111) (Refs. 14–16) or Pb/Ag(111) (Refs. 16–18) show an unmatched spin splitting (large Rashba parameter α), which is caused by an additional in-plane gradient of the potential;¹⁹ the sp_z surface states in these alloys show the conventional topology of the Rashba model as well but with minor deviations (e.g., a nonzero but small P_z due to the in-plane gradient).

From the experimental and theoretical findings available so far one is lead to conclude that the spin topology imposed by the Rashba model shows up in a large number of systems, if not in all systems. In this paper, we show by first-principles calculations and two-photon photoemission (2PPE) experiments for the surface alloy Bi/Cu(111) that this topology cannot be taken for granted. Instead of the conven-

tional topology with oppositely rotating spins [Fig. 1(a)], we find momentum distributions with identical spin-rotation directions [Fig. 1(b)]. The origin of this effect is explained by the hybridization of surface states with different orbital character mediated by the spin-orbit interaction.

Our findings differ qualitatively from those in conventional Rashba systems. The momentum distribution of the latter comprises spin topologies with identical rotation direction as well but these are restricted to the low-density regime⁶ (or region I in Ref. 20), i.e., to energies between ϵ_0 and the band extrema. This regime extends over 0.015 eV for the sp_z surface states in Bi/Cu(111).²¹ But we find such topology in a 0.7 eV wide window in the high-density regime of the $p_x p_y$ surface states. Note that the present findings are similar to those for topological metals and insulators.^{22,23}

Previous studies of the Rashba effect at metal surfaces focused on occupied surface states since these can be accessed by angle-resolved photoelectron spectroscopy (ARPES).²⁴ These states are mainly of sp_z orbital character and thus agree with those of a 2DEG [see Ref. 10 for Au(111)]. As a consequence, their spin topology is consistent with that of the Rashba model [Fig. 1(a)].

In the Bi/Ag(111) and Pb/Ag(111) surface alloys, the adatoms induce also sp_z states but with larger splitting [as compared to Au(111)] and negative dispersion (effective mass $m^* < 0$).¹⁶ Further, there are indications for another mainly

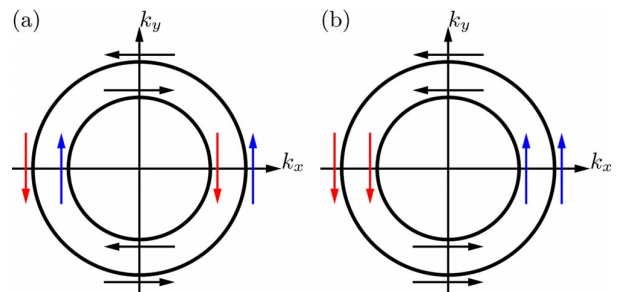


FIG. 1. (Color online) Spin topologies in a spin-orbit split 2DEG (schematic): (a) Conventional Rashba-type and (b) unconventional spin topology in the momentum distribution. The spin polarization of the “inner” and the “outer” state is represented by arrows.

unoccupied set of bands. Since these bands cross at energies ϵ_0 above the Fermi energy E_F , their splitting Δk could only be extrapolated from their occupied “tails.” First-principles calculations show that these states are of $p_x p_y$ orbital character (i.e., oriented within the surface plane). Their occupied tails display the same spin topology as the sp_z states [Fig. 1(a)].

In the present work we focus on Bi/Cu(111) which shows a $\sqrt{3} \times \sqrt{3}$ -R30° surface geometry,²⁵ such as Bi/Ag(111) and Pb/Ag(111). Consequently, the surface electronic structure of Bi/Cu(111) consists also of two sets of Rashba-split surface states, namely, the sp_z and the $p_x p_y$ branch. As found by ARPES and scanning tunneling microscopy experiments,^{21,26} the partially occupied sp_z branch extends to about $E_F + 0.23$ eV and shows a Rashba splitting of $\Delta k \approx 0.035$ Bohr⁻¹.

II. EXPERIMENTAL FINDINGS

In contrast to ARPES which maps the *occupied* states, we can additionally access the *unoccupied* states by angle-dependent 2PPE. Experimental details are as described in Ref. 27. The single-photon energy used in the 2PPE measurements was 3.1 eV, using off-normal-incident p -polarized light. Bi was deposited by thermal evaporation on the Cu(111) substrate kept at 500 K. The formation of the $\sqrt{3} \times \sqrt{3}$ -R30° structure was checked by low-energy electron diffraction.

Angle-dependent 2PPE spectra were measured by rotating the sample around the axis perpendicular to the optical plane. The sample was oriented so that \mathbf{k}_{\parallel} was measured in the plane containing the $[111]$ and $[11\bar{2}]$ directions. The resulting experimental 2PPE intensity map is shown in Fig. 2. After the deposition of Bi, a reduction in the work function from about 4.9 eV for clean Cu(111) to below 4.4 eV is observed, as judged from the low-energy cutoff of the 2PPE spectrum at $\mathbf{k}_{\parallel}=0$ in Fig. 2. This makes possible the observation of additional unoccupied intermediate states in the energy region below 1.8 eV which cannot be excited above the work function on clean Cu(111) using 3.1 eV photons.

In the lower half of Fig. 2, at about 4.5 eV final-state energy, a pair of split bands is clearly visible. These bands belong to unoccupied states located one photon energy (3.1 eV) below the final-state energy; as will become clear from the comparison with theory, these bands originate from the $p_x p_y$ surface states. They cross at $\bar{\Gamma}$ at about $E_F + (1.38 \pm 0.05)$ eV, and their maxima are shifted symmetrically from $\bar{\Gamma}$ by about (0.06 ± 0.01) Bohr⁻¹ [$\Delta k \approx (0.12 \pm 0.02)$ Bohr⁻¹] (Fig. 3).

In addition to the unoccupied states, the 2PPE experiment measures also the occupied states of sp_z character (see Fig. 4), which are excited by two photons to final-state energies near 6.2 eV in the upper half of Fig. 2. We note that a slightly increased intensity is also observed in the region extending to about 0.5 eV above the crossing point of the unoccupied split bands in Fig. 2. While no clearly dispersing bands can be observed experimentally, this intensity is consistent with the theoretical bands in Fig. 4 above 1.5 eV; their weak ex-

perimental intensity correlates with a comparably small theoretical spectral density.

The 2PPE intensity depends strongly on the emission angle, as can be seen by the pronounced intensity maximum at about 4.5 eV final-state energy and +5° emission angle (red spot in Fig. 2; note the comparably small intensity at -5°). Such features also appear also in the conventional (one-photon) photoemission from these surface alloys and can be explained by the transition matrix elements.

III. THEORETICAL FINDINGS

To elucidate the dispersion and especially the spin topology of the unoccupied bands we performed first-principles electronic-structure calculations, in close analogy to our previous investigations on surface alloys (e.g., Ref. 16). The interatomic distances at the surface are obtained from total-energy minimization using the Vienna *Ab initio* Simulation Package.²⁸ Due to the much smaller lattice constant of Cu as compared to Ag ($d_{\text{Cu-Cu}}=4.83$ Bohr and $d_{\text{Ag-Ag}}=5.40$ Bohr), the Bi atoms are more relaxed outward (by 38% of the bulk interlayer distance of Cu, $d_{\perp}=3.94$ Bohr) than in Bi/Ag(111). The optimum surface geometry serves as input for Korringa-Kohn-Rostoker (KKR) calculations. The electronic structure is analyzed in detail by means of the spectral density $n(E, \mathbf{k})$, which is computed from the Green’s function in the relativistic layer-KKR method. $n(E, \mathbf{k})$ is resolved with respect to site, spin, and angular momentum.

The spin-averaged spectral density of a Bi site shows the split sp_z and $p_x p_y$ surface states (Fig. 4). Each branch comprises an “inner” band (with smaller $|\mathbf{k}|$) and an “outer” band (with larger $|\mathbf{k}|$). The sp_z bands cross at $E_F + 0.1$ eV; their Rashba splitting is $\Delta k=0.10$ Bohr⁻¹ (Bi/Ag(111): $\Delta k=0.14$ Bohr⁻¹). The $p_x p_y$ bands cross at $E_F + 1.4$ eV [experiment: $E_F + (1.38 \pm 0.05)$ eV], with $\Delta k=0.08$ Bohr⁻¹ [experiment: $\Delta k=(0.12 \pm 0.02)$ Bohr⁻¹]. The theoretical results are thus consistent with the experimental findings and identify the split bands in experiment (Fig. 3) with the $p_x p_y$ surface states. The spectral density becomes blurred in regions in which the surface states hybridize with Cu-bulk states. The dispersion of the two branches follows closely that imposed by the Rashba model [Eq. (1) with negative effective mass m^*]. An exception, however, might be a “kink” in the inner $p_x p_y$ band at $(E, k) \approx (E_F + 0.6$ eV, ± 0.12 Bohr⁻¹) (marked in Fig. 4).

The spin topology of the surface states is visualized by the difference $n(E, \mathbf{k})_{\uparrow} - n(E, \mathbf{k})_{\downarrow}$ of the spectral densities, where \uparrow and \downarrow indicate the projection of the in-plane spin-polarization component normal to \mathbf{k} (Fig. 5; this \mathbf{P} component is prescribed by the Rashba model and is by far dominating). For the sp_z branch we find the expected conventional spin topology which is imposed by the Rashba model; the opposite spin-rotation direction of the two bands shows up at energies below the crossing at $\bar{\Gamma}$ as a red-blue-red-blue color coding with increasing wave number [line a in Fig. 5; cf. Fig. 1(a)]. In contrast, the $p_x p_y$ branch shows a red-red-blue-blue coding at, say, $E_F + 1.0$ eV (line b in Fig. 5); thus these surface states have identical rotation direction [cf. Fig. 1(b)]. This finding is not consistent with the Rashba model: It

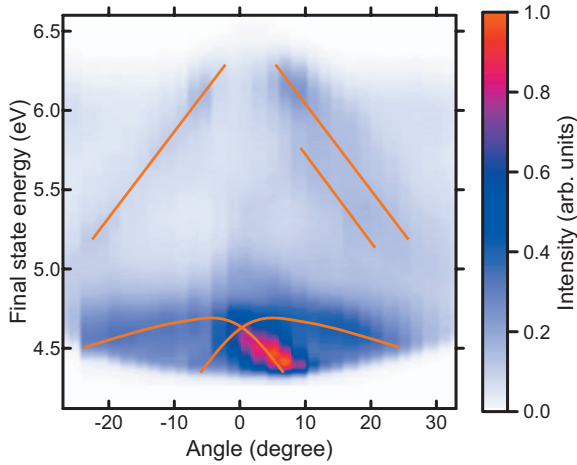


FIG. 2. (Color) Two-photon photoemission from Bi/Cu(111). The intensity for given final-state energy and emission angle is shown as color scale. The unoccupied $p_x p_y$ surface states appear at about 4.5 eV. To guide the eye, orange lines highlight the dispersion of the electronic states.

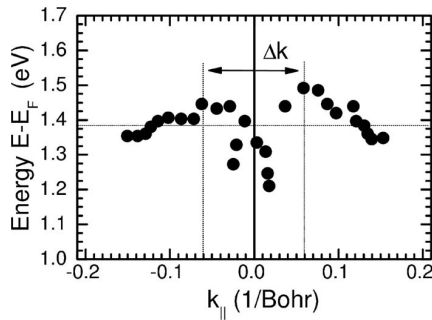


FIG. 3. Rashba splitting Δk in the unoccupied $p_x p_y$ surface states of Bi/Cu(111), as obtained from two-photon photoemission experiments (Fig. 2).

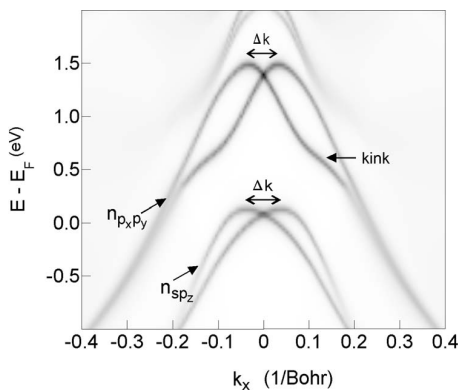


FIG. 4. Surface electronic structure of Bi/Cu(111) as obtained from first-principles calculations. The spectral density $n(E, \mathbf{k})$ for a Bi site is depicted as gray scale (white=zero). The sp_z and the $p_x p_y$ surface-state branches are indicated.

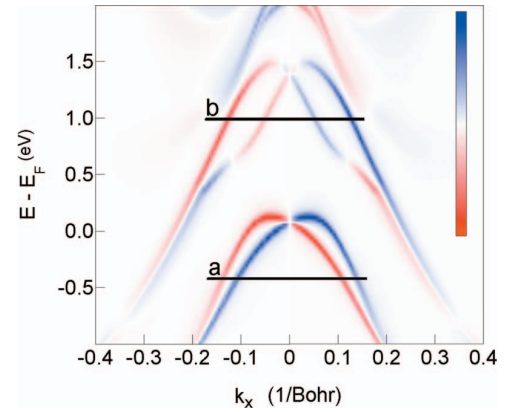


FIG. 5. (Color) Spin-resolved electronic structure of Bi/Cu(111) as obtained by first-principles calculations. The difference $n(E, \mathbf{k})|_{\uparrow} - n(E, \mathbf{k})|_{\downarrow}$ of the spin-projected spectral densities for a Bi site is depicted as color scale (red=negative, white=zero, and blue=positive). The spin projection is in-plane and perpendicular to the wave vector. Horizontal lines are guides to the conventional (line a) and unconventional (line b) spin topology of the sp_z and the $p_x p_y$ states, respectively.

appears that the spin polarization of the inner $p_x p_y$ state is reversed in comparison to that of the inner sp_z state. It is important to note that at energies below the kink the spin polarization of this band has changed sign, e.g., at $E_F + 0.2$ eV, and the conventional spin topology is restored; in other (E, \mathbf{k}) regions its absolute value is as large as 90%.

Deviations from a smooth dispersion, as seen at the kink (Fig. 4), indicate hybridization of electronic states. A group-theoretical analysis shows that wave functions can be represented either as^{29,30}

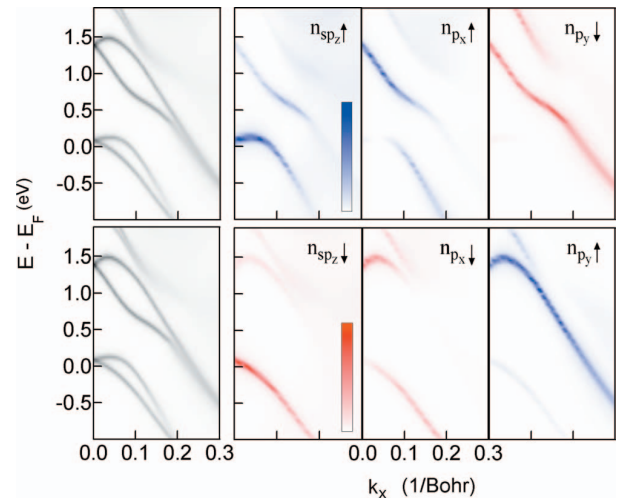


FIG. 6. (Color) Hybridization of surface states in Bi/Cu(111). The orbital- and spin-resolved spectral densities at a Bi site are depicted as color scales. The top [bottom] panels comprise contributions according to Eq. (2) [Eq. (3)]. All data share the same color scale, with white=zero and dark red (dark blue)=maximum spectral density (70 states/Hartree). The left panels display the total spectral density for comparison (in gray scale; cf. Fig. 4).

$$|\psi\rangle = |sp_z\uparrow\rangle + |p_x\uparrow\rangle + |p_y\downarrow\rangle \quad (2)$$

or as

$$|\psi\rangle = |sp_z\downarrow\rangle + |p_x\downarrow\rangle + |p_y\uparrow\rangle. \quad (3)$$

The spinors $|\uparrow\rangle$ and $|\downarrow\rangle$ are quantized with respect to the y axis. Both the outer sp_z band and the inner $p_x p_y$ state belong to the representation of Eq. (2) and hence are allowed to hybridize. Thus, if the usually dominating $|p_y\downarrow\rangle$ component of the inner $p_x p_y$ state is surpassed by the $|p_x\uparrow\rangle$ component, the spin polarization of this state changes sign. That this is indeed the case is seen by the $|p_x\uparrow\rangle$ contribution to $n(E, \mathbf{k})$, which increases with energy (top row in Fig. 6). At the kink, where the inner $p_x p_y$ band and outer sp_z band approach, both the $|sp_z\uparrow\rangle$ and the $|p_y\downarrow\rangle$ orbitals show a significant spectral density; the kink shape is thus attributed to the hybridization of these two bands. The inner sp_z and the outer $p_x p_y$ states belong to the representation of Eq. (3) and hybridize as well but less due to their larger (E, \mathbf{k}) “distance” (bottom row in Fig. 6).

Note that hybridization of orbitals with opposite spin is brought about only by SO coupling.³¹ Further, the effect is not described by first-order perturbation theory in the SO interaction because this order would produce the spin splitting but not the hybridization.

The Dresselhaus effect could in principle produce a deviation from the Rashba-type spin topology.³² A closer analysis, however, shows that it vanishes in the present case. Therefore, hybridization as a result of the spin-orbit interaction remains as the sole reason for the unconventional spin topology in Bi/Cu(111).

An important ingredient for the unmatched splitting found in these surface alloys is the in-plane gradient of the potential.^{15,19} As the gradient perpendicular to the surface (along z) produces the in-plane spin polarization (P_x and P_y),

the in-plane gradient gives rise to a nonzero P_z . A $p_x p_y$ surface state is expectedly more susceptible to the in-plane gradient than a sp_z surface state. Consequently, its P_z should be larger. Indeed, P_z of the $p_x p_y$ states is negligibly for small $|\mathbf{k}|$ but reaches 20% in absolute value for larger wave vectors ($|\mathbf{k}| > 0.15 \text{ Bohr}^{-1}$). In contrast, the sp_z states have no significant P_z .

The demonstrated mechanism for changing the spin topology of the surface states in surface alloys is also present in Bi/Ag(111), as we have investigated theoretically as well (results not shown here). In comparison with Bi/Cu(111), the effect is less pronounced because hybridization of the sp_z and $p_x p_y$ branches is decreased by the smaller outward relaxation of Bi.¹⁸ Another aspect is that the surface states hybridize with Ag bulk states in a large (E, \mathbf{k}) region due to projected bulk-band structure of Ag. As a consequence, they show no clear kink.

IV. CONCLUDING REMARKS

In summary, there is more to the spin-resolved electronic structure of surface states in surface alloys than first imagined. Although the basic properties are described by the standard Rashba model, additional effects (e.g., hybridization and the in-plane potential gradient) can change important features of the electronic states and their spin topology. In turn, there is the possibility to exploit these mechanisms in new spintronics devices and in new effects (e.g., Refs. 6 and 23).

Since hybridization is a general mechanism, the present effect can be important also in other systems, possibly at other high-symmetry points in the two-dimensional Brillouin zone or at other energies. It is therefore desirable to carry out spin-resolving experiments on the spin-orbit splitting of surface states.

*Corresponding author; henk@mpi-halle.de

¹ Y. A. Bychkov and E. I. Rashba, *J. Phys. C* **17**, 6039 (1984).

² S. Datta and B. Das, *Appl. Phys. Lett.* **56**, 665 (1990).

³ T. Koga, J. Nitta, H. Takayanagi, and S. Datta, *Phys. Rev. Lett.* **88**, 126601 (2002).

⁴ J. Sinova, D. Culcer, Q. Niu, N. A. Sinitsyn, T. Jungwirth, and A. H. MacDonald, *Phys. Rev. Lett.* **92**, 126603 (2004).

⁵ J.-i. Ohe, M. Yamamoto, T. Ohtsuki, and J. Nitta, *Phys. Rev. B* **72**, 041308(R) (2005).

⁶ E. Cappelluti, C. Grimaldi, and F. Marsiglio, *Phys. Rev. Lett.* **98**, 167002 (2007).

⁷ L. Petersen and P. Hedegård, *Surf. Sci.* **459**, 49 (2000).

⁸ Y. M. Koroteev, G. Bihlmayer, J. E. Gayone, E. V. Chulkov, S. Blügel, P. M. Echenique, and P. Hofmann, *Phys. Rev. Lett.* **93**, 046403 (2004).

⁹ R. Winkler, *Spin-Orbit Coupling Effects in Two-Dimensional Electron and Hole Systems* (Springer, Berlin, 2003).

¹⁰ J. Henk, M. Hoesch, J. Osterwalder, A. Ernst, and P. Bruno, *J. Phys.: Condens. Matter* **16**, 7581 (2004).

¹¹ J. Nitta, T. Akazaki, H. Takayanagi, and T. Enoki, *Phys. Rev.*

Lett. **78**, 1335 (1997).

¹² S. LaShell, B. A. McDougall, and E. Jensen, *Phys. Rev. Lett.* **77**, 3419 (1996).

¹³ F. Reinert, *J. Phys.: Condens. Matter* **15**, S693 (2003).

¹⁴ T. Hirahara, T. Nagao, I. Matsuda, G. Bihlmayer, E. V. Chulkov, Y. M. Koroteev, P. M. Echenique, M. Saito, and S. Hasegawa, *Phys. Rev. Lett.* **97**, 146803 (2006).

¹⁵ C. R. Ast, J. Henk, A. Ernst, L. Moreschini, M. C. Falub, D. Pacilé, P. Bruno, K. Kern, and M. Grioni, *Phys. Rev. Lett.* **98**, 186807 (2007).

¹⁶ C. R. Ast *et al.*, *Phys. Rev. B* **77**, 081407(R) (2008).

¹⁷ D. Pacilé, C. R. Ast, M. Papagno, C. Da Silva, L. Moreschini, M. Falub, A. P. Seitsonen, and M. Grioni, *Phys. Rev. B* **73**, 245429 (2006).

¹⁸ G. Bihlmayer, S. Blügel, and E. V. Chulkov, *Phys. Rev. B* **75**, 195414 (2007).

¹⁹ J. Prempfer, M. Trautmann, J. Henk, and P. Bruno, *Phys. Rev. B* **76**, 073310 (2007).

²⁰ C. R. Ast, G. Wittich, P. Wahl, R. Vogelgesang, D. Pacilé, M. C. Falub, L. Moreschini, M. Papagno, M. Grioni, and K. Kern,

- Phys. Rev. B **75**, 201401(R) (2007).
- ²¹L. Moreschini, A. Bendounan, H. Bentmann, M. Assig, F. Reinert, C. R. Ast, M. Grioni, and J. Henk (unpublished).
- ²²J. W. Wells *et al.*, Phys. Rev. Lett. **102**, 096802 (2009).
- ²³D. Hsieh *et al.*, Science **323**, 919 (2009).
- ²⁴F. Reinert, G. Nicolay, S. Schmidt, D. Ehm, and S. Hufner, Phys. Rev. B **63**, 115415 (2001).
- ²⁵D. Kaminski, P. Poodt, E. Aret, N. Radenovic, and E. Vlieg, Surf. Sci. **575**, 233 (2005).
- ²⁶H. Bentmann, F. Forster, L. Moreschini, M. Grioni, and F. Reinert (unpublished).
- ²⁷F. Bisio, M. Nyvlt, J. Franta, H. Petek, and J. Kirschner, Phys. Rev. Lett. **96**, 087601 (2006).
- ²⁸G. Kresse and J. Furthmüller, Phys. Rev. B **54**, 11169 (1996).
- ²⁹T. Inui, Y. Tanabe, and Y. Onodera, *Group Theory and Its Applications in Physics*, Springer Series in Solid State Sciences Vol. 78 (Springer, Berlin, 1990).
- ³⁰T. Oguchi and T. Shishidou, J. Phys. Condens. Matter **21**, 092001 (2009).
- ³¹That SO coupling is the origin of the kink was checked by scaling the SO strength following Ref. 33: With vanishing SO coupling, the kink disappears.
- ³²G. Dresselhaus, Phys. Rev. **100**, 580 (1955).
- ³³H. Ebert, H. Freyer, and M. Deng, Phys. Rev. B **56**, 9454 (1997).

Paper IV

Towards a ferroelectric control of Rashba spin-orbit coupling:
Bi on BaTiO₃(001) from first principles

Toward a ferroelectric control of Rashba spin-orbit coupling: Bi on BaTiO₃(001) from first principles

H. Mirhosseini,¹ I. V. Maznichenko,² Samir Abdelouahed,¹ S. Ostanin,¹ A. Ernst,¹ I. Mertig,^{1,2} and J. Henk^{1,*}

¹Max-Planck-Institut für Mikrostrukturphysik, Weinberg 2, D-06120 Halle (Saale), Germany

²Institut für Physik, Martin-Luther-Universität Halle-Wittenberg, D-06120 Halle (Saale), Germany

(Received 30 October 2009; published 22 February 2010)

As demonstrated conceptually by first-principles calculations, the Rashba spin splitting in the $6p$ states of a Bi adlayer on BaTiO₃(001) can be manipulated by the electric polarization in the ferroelectric substrate. Although this spin-electric effect is moderate, with a relative change in the splitting of about 5%, the absolute splitting of about 0.24 \AA^{-1} is unmatched. Further, the occupied $6p$ surface states display an anisotropic dispersion and deviate significantly from the free-electron model of the Rashba effect. Our findings may pave a route for spin-electronic devices.

DOI: [10.1103/PhysRevB.81.073406](https://doi.org/10.1103/PhysRevB.81.073406)

PACS number(s): 73.20.At, 77.84.Ek, 77.84.Cg, 71.70.Ej

I. INTRODUCTION

A key issue in spin electronics¹ is the manipulation of the electrons' spins by an electric field. This goal can be achieved for example by the magnetoelectric coupling in a multiferroic²⁻⁴ or by the tunable strength of the Rashba spin-orbit coupling in a two-dimensional electron gas at a semiconductor interface.⁵⁻⁸

In an isotropic two-dimensional electron gas, the Rashba effect lifts Kramers' degeneracy.⁹ As a consequence, the dispersion relations of the free electrons which are confined to the xy plane become split,

$$E_{\pm}(\mathbf{k}_{\parallel}) = \frac{\hbar^2 \mathbf{k}_{\parallel}^2}{2m^*} \pm \gamma_R |\mathbf{k}_{\parallel}| + E_0, \quad \mathbf{k}_{\parallel} = (k_x, k_y). \quad (1)$$

Here, the electronic states are labeled by $+$ and $-$, and m^* is the effective electron mass. The Rashba parameter γ_R which quantifies the spin-orbit coupling strength comprises effectively two contributions:¹⁰ The "atomic" contribution is due to the strong potential of the ions and the "confinement" contribution is due to the gradient of the confinement potential in z direction.

Surface states which are subject to the Rashba spin-orbit coupling have gained considerable attention in the last years.^{11,12} A particularly large Rashba splitting $k_R = |m^*| \gamma_R / \hbar^2$, which is defined as the mutual shift of the split bands, is observed for adlayers of heavy elements with p valence shell on noble metal and semiconductor surfaces, e. g., Bi/Ag(111) (Ref. 13) and Bi/Si(111).¹⁴ With regard to the abovementioned contributions, the strength of the Rashba spin-orbit coupling in an adlayer can be manipulated by alloying, for example of Pb and Bi (atomic contribution),¹⁵ or by changing the charge density in the surface region by adatoms (confinement contribution; e. g., Refs. 16 and 17).

In this Brief Report, we propose a third route for manipulating the Rashba splitting of electronic states in an adsorbed layer: While keeping a Bi adlayer, we use a ferroelectric, here BaTiO₃(001), in place of a metallic or semiconducting substrate. The idea is to (ferro)electrically control the Rashba splitting as follows. The reversal of the intrinsic electric polarization \mathbf{P} in the perovskite by an external electric field is equivalent to reversing the mutual displacements of Ti and O

atoms in [001] direction. Consequently, the charge density at the Bi/BaTiO₃ interface is changed, leading eventually to a modification of the Rashba splitting of the surface states in the Bi adlayer. This scenario of a "spin-electric coupling" is similar to the magnetoelectric coupling in a two-phase multiferroic, say in Fe/BaTiO₃.¹⁸⁻²⁰

Rashba/ferroelectric systems have a number of advantages. First, because the electric polarization \mathbf{P} is changed by an electric pulse (in contrast to a steady electric field),⁸ the Rashba splitting would remain switched permanently. This feature makes such a system suitable for information storage devices.²¹ Second, the deposition of adatoms could alter the surface electronic structure significantly²² and switching of the splitting may be difficult or even impossible.²³ Thus, Bi/BaTiO₃ and similar systems lend themselves support for a new class of materials for spin electronics devices.

In this Brief Report, we demonstrate conceptually the proposed mechanism for a complete monolayer of Bi on BaTiO₃(001). Using *ab initio* methods of computational material science, we focus on (i) the strength of the Rashba splitting in the $6p$ surface states of Bi, (ii) the effect of switching the electric polarization in the ferroelectric substrate on the Rashba splitting of the Bi surface states, and (iii) their dispersion and spin polarization as compared to the free-electron model of the Rashba effect.

II. COMPUTATIONAL ASPECTS

We follow the first-principles approach which has proved successful in earlier studies of two-phase multiferroics²⁰ and of Rashba systems.^{14,15,24}

We consider a BaTiO₃(001) substrate with TiO₂ termination; the deposited Bi atoms form a complete (1×1) monolayer. The geometric structures have been obtained by the Vienna *ab initio* simulation package (VASP).²⁵ The adatoms have initially been placed at different positions and are subsequently relaxed to their equilibrium positions.

The structural data serve as input for the relativistic calculations which aim at the Rashba splitting and rely on our multiple-scattering theoretical codes for semi-infinite systems [Korringa-Kohn-Rostoker (KKR) and layer-KKR methods; e. g., Ref. 26]. A detailed analysis of the electronic

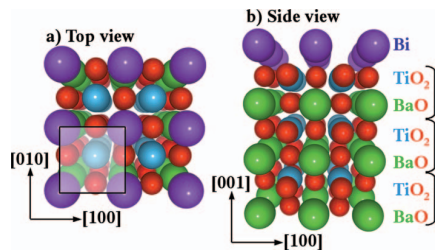


FIG. 1. (Color) Geometry of Bi/BaTiO₃(001). (a) Perspective top and (b) side views of the Bi-covered BaTiO₃(001) surface for electric polarization P_{\uparrow} . Spheres represent Bi (violet), Ba (green), Ti (blue), and O (red) sites. A two-dimensional unit cell is displayed in (a) as transparent square. Three BaTiO₃ stacks which each comprising a BaO and a TiO₂ layer are depicted in (b).

structure is obtained from the Bloch spectral density

$$n_{ls}(E, \mathbf{k}_{\parallel}) = -\frac{1}{\pi} \text{Im Tr } G^{+}(\mathbf{r}_{ls}, \mathbf{r}_{ls}; E, \mathbf{k}_{\parallel}), \quad (2)$$

which is determined from the site-diagonal Green function $G^{+}(\mathbf{r}_{ls}, \mathbf{r}_{ls}; E, \mathbf{k}_{\parallel})$. The trace involves integration over the muffin-tin sphere of site s in the two-dimensional unit cell of layer l , with \mathbf{r}_{ls} being associated with this sphere.²⁶ $n_{ls}(E, \mathbf{k}_{\parallel})$ can be resolved further with respect to orbital composition and spin orientation.

We have checked that basic quantities are consistently reproduced by the VASP and the KKR codes. These also agree nicely with those obtained by our additional FLAPW calculations.²⁷

III. SURFACE GEOMETRY

In the following, we consider two major configurations which are distinguished by their intrinsic electric polarization \mathbf{P} in the bulk of the BaTiO₃ substrate. In accordance with the mutual displacement of the Ti and O atoms, \mathbf{P} is along the [001] direction which is taken as z direction. For \mathbf{P} pointing

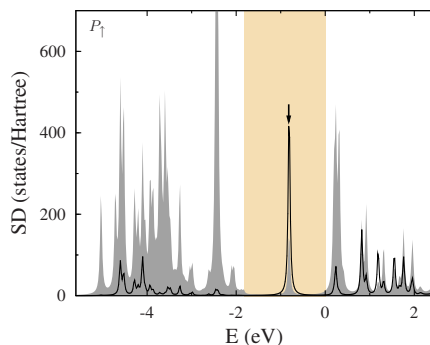


FIG. 2. (Color online) Surface electronic structure of Bi/BaTiO₃(001) for P_{\uparrow} . Bloch spectral densities (“SD”) $n(E, \mathbf{k}_{\parallel})$ are shown for the Bi adlayer (line) and for the adjacent BaTiO₃ stack (filled) at $\bar{\Gamma}$ ($\mathbf{k}_{\parallel}=0$). The underlying rectangle marks the fundamental band gap; the conduction band minimum is taken as energy zero. The Bi $6p$ surface states are indicated by an arrow.

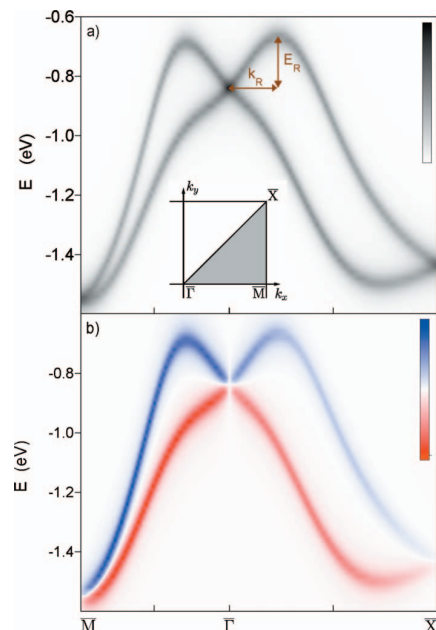


FIG. 3. (Color) Surface states in Bi/BaTiO₃(001) for P_{\uparrow} . (a) Spin-integrated Bloch spectral density for Bi imaged as gray scale (white 0, black 400 states/Hartree) along $\bar{M}-\bar{\Gamma}-\bar{X}$ of the two-dimensional Brillouin zone. The Rashba splitting k_R and the Rashba energy E_R are indicated. The inset shows a quarter of the Brillouin zone. (b) Spin-resolved density for Bi depicted as color scale. Blue (red) indicates a positive (negative) difference $n^{\uparrow}-n^{\downarrow}$, with the spin projection normal to \mathbf{k}_{\parallel} and with extrema of ± 150 states/Hartree. Energy scale as in Fig. 2.

toward $-z$, referred to as P_{\downarrow} , the z coordinates of Ti and O sites in the same layer obey $z_{\text{Ti}} < z_{\text{O}}$ ($z_{\text{Ti}} - z_{\text{O}} = -0.09$ Å). The opposite case is referred to as P_{\uparrow} , with $z_{\text{Ti}} > z_{\text{O}}$.

A total-energy analysis shows that Bi forms a 1×1 adlayer, with Bi on top of the Ba atoms of the subsurface BaO layer (Fig. 1 for P_{\uparrow} ; all results for P_{\downarrow} agree qualitatively with those for P_{\uparrow} and are therefore not shown). Their distance in z direction to the surface Ti sites is 2.11 Å for P_{\uparrow} , which is

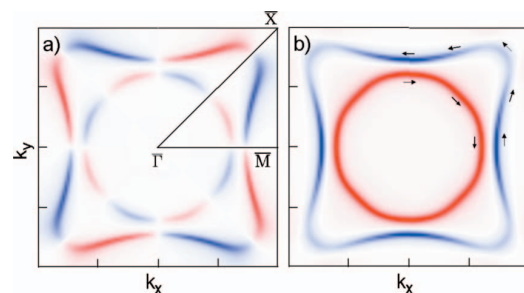


FIG. 4. (Color) Spin topology of the surface states in Bi/BaTiO₃(001) for P_{\uparrow} . (a) Radial and (b) tangential spin polarization components are visualized as the difference $n^{\uparrow}-n^{\downarrow}$ of Bloch spectral densities at Bi in the entire two-dimensional Brillouin zone. The energy is -1.30 eV (energy scale as in Fig. 2). Dark blue and red indicate $+150$ and -150 states/Hartree, respectively. Arrows in (b) give a visual impression of the total spin polarization.

TABLE I. Rashba effect in Bi/BaTiO₃. The splitting k_R , the Rashba energy E_R , the effective mass m^* (in units of the electron mass m_e), and the Rashba parameter γ_R for both bulk electric polarization P_\uparrow and P_\downarrow are given for the $\bar{\Gamma}-\bar{M}$ and the $\bar{\Gamma}-\bar{X}$ direction of the two-dimensional Brillouin zone [inset in Fig. 3(a)].

	$\bar{\Gamma}-\bar{M}$				$\bar{\Gamma}-\bar{X}$			
	k_R (\AA^{-1})	E_R (eV)	m^* (m_e)	γ_R (eV \AA)	k_R (\AA^{-1})	E_R (eV)	m^* (m_e)	γ_R (eV \AA)
P_\uparrow	0.22	0.16	-1.14	1.45	0.25	0.18	-1.36	1.42
P_\downarrow	0.23	0.16	-1.22	1.39	0.27	0.18	-1.48	1.36

equivalent to 52.9% of the bulk Ba-Ba z distance (3.99 \AA). For P_\downarrow we find a z distance of 2.16 \AA (54.0%).

It turns out that for both P_\uparrow and P_\downarrow , the polarization at the topmost TiO₂ layer is negative (i. e., $z_{\text{Ti}} < z_{\text{O}}$).²⁸ However, the relaxations of these atoms differ: $z_{\text{Ti}} - z_{\text{O}} = -0.13$ \AA for P_\uparrow and -0.18 \AA for P_\downarrow . In summary, the surface geometry depends slightly on the orientation of the bulk electric polarization.

IV. RASHBA SPLITTING IN THE BI SURFACE STATES

The Bi adlayer gives rise to occupied $6p$ electronic states in the fundamental band gap of the surface BaTiO₃ stack. At $\bar{\Gamma}$ these show up at energies $E_0 = -0.82$ eV for P_\uparrow (arrow in Fig. 2) and at -0.84 eV for P_\downarrow , respectively. These are mostly confined to the Bi layer but show also considerable spectral weight in the adjacent layer, making them subject to switching of \mathbf{P} .

The dispersions of the Bi surface states show the typical signatures of the Rashba splitting: k_R and the Rashba energy E_R which are indicated in Fig. 3(a). Since the dispersion is anisotropic, the characteristics of the Rashba splitting are anisotropic as well (Table I). Although the origin of this anisotropy are higher-order terms in \mathbf{k}_\parallel ,²⁹ we quantify the effect by means of an anisotropic effective mass and Rashba parameter.

The switching of the electric polarization \mathbf{P} affects indeed the Rashba splitting k_R (Table I), thereby confirming the above motivation. The strength of this spin-electric coupling is quantified by the relative change in k_R ; for $\bar{\Gamma}-\bar{M}$ it is about 4.5% whereas for $\bar{\Gamma}-\bar{X}$ it is about 5.5%. These numbers are qualitatively explained on one hand by the weak polarization dependence of the surface geometry and on the other hand by the strong localization of the Bi $6p$ states to the adlayer. Both a larger relaxation and a stronger hybridization of the Bi states with those of the substrate could enhance the effect. We would like to stress that the relative change in the surface magnetization of a single Fe layer on BaTiO₃(001) is 2.8%;²⁰ this shows that the spin-electric coupling is at least as large as the magnetoelectric coupling.

The average splitting k_R of about 0.24 \AA^{-1} is sizably larger than the unmatched 0.13 \AA^{-1} reported for Bi/Ag(111).¹³ However, E_R is with about 0.170 eV less than in Bi/Ag(111) (0.200 eV). Consequently, the effective masses $m^* = -\hbar^2 k_R^2 / (2E_R)$ of Bi/BaTiO₃ are larger (in absolute value) than in Bi/Ag(111) ($-0.32m_e$). Because the

Rashba parameter of the free-electron model depends on m^* , the numerical values for $\gamma_R = 2|E_R|/k_R$ in Bi/BaTiO₃ are considerable less than that in Bi/Ag(111) (3.08 eV \AA), although the splitting in reciprocal space is about as twice as large.

We note that relevant for applications is not the strength γ_R of the Rashba spin-orbit coupling but the actual splitting k_R . A large splitting in reciprocal space is equivalent to a small wavelength in direct space. As a consequence, the spatial range in which the electronic wave functions of the split states can effectively interfere in a spin electronics device is small as well. This feature is favorable since it allows reduced device dimensions.

V. MOMENTUM DISTRIBUTIONS AND SPIN TOPOLOGY OF THE BI SURFACE STATES

Momentum distributions which display the Bloch spectral density versus \mathbf{k}_\parallel at fixed energy E (Fig. 4) deviate significantly from the circular momentum distributions of the free-electron model, in accordance with the dispersion relations (Fig. 3). The anisotropy shows up in particular for the outer band (with larger $|\mathbf{k}_\parallel|$) which reflects the $4mm$ symmetry of the surface.

Another signature of the Rashba effect—besides k_R and E_R —is the spin polarization \mathcal{S}_\pm of the split electronic states. For free electrons, \mathcal{S}_\pm lies within the confinement plane, is tangential to the circular momentum distribution and is complete ($|\mathcal{S}_\pm| = 100\%$). For Bi/BaTiO₃ we find in-plane \mathcal{S}_\pm but also distinct deviations from the free-electron model, as is exemplified at $E = -1.30$ eV (Fig. 4). The inner state, with small $|\mathbf{k}_\parallel|$, compares well with the free-electron model; confer the almost circular momentum distribution with small radial component (a) and constant tangential component (b). The outer state, with larger $|\mathbf{k}_\parallel|$, shows a large tangential component, in particular along $\bar{\Gamma}-\bar{M}$, but significantly less along $\bar{\Gamma}-\bar{X}$. This together with the shape of its sizable radial component implies that its spin follows the curvature of its noncircular momentum distribution [arrows in Fig. 4(b)].

VI. CONCLUDING REMARKS

Our theoretical investigation provides a proof of concept for spin-electric coupling in an adlayer of a heavy p metal on

a ferroelectric substrate: Switching of the intrinsic electric polarization \mathbf{P} in the ferroelectric (here: BaTiO₃) affects the strength of the Rashba splitting in the adlayer (here: Bi).

The present work predicts a moderate spin-electric coupling but a large absolute Rashba-type spin splitting. Nevertheless, it is conceivable to increase the effect by larger atomic displacements in particular at the ferroelectric/adlayer interface. A possible candidate might be PbTiO₃ which shows larger displacements and electric polarizations than BaTiO₃.²⁸

We encourage to search for improved Rashba-split/ferroelectric systems in both theory and experiment. The ultimate spin-electric coupling would be a change in sign of the Rashba parameter γ_R —and hence of the spin polarization \mathbf{S} —upon reversal of \mathbf{P} .

We appreciate very much fruitful discussions with M. Fechner and Chr. R. Ast. This work is supported by the *Sonderforschungsbereich 762* “Functionality of Oxide Interfaces.”

*Corresponding author; henk@mpi-halle.de

- ¹I. Žutić, J. Fabian, and S. Das Sarma, *Rev. Mod. Phys.* **76**, 323 (2004).
- ²W. Eerenstein, N. D. Mathur, and J. F. Scott, *Nature (London)* **442**, 759 (2006).
- ³S.-W. Cheong and M. Mostovoy, *Nature Mater.* **6**, 13 (2007).
- ⁴H. Béa, M. Gajek, M. Bibes, and A. Barthélémy, *J. Phys.: Condens. Matter* **20**, 434221 (2008).
- ⁵Y. A. Bychkov and E. I. Rashba, *J. Phys. C* **17**, 6039 (1984).
- ⁶S. Datta and B. Das, *Appl. Phys. Lett.* **56**, 665 (1990).
- ⁷N. Samarth, in *Solid State Physics* Vol. 58, edited by H. Ehrenreich and F. Spaepen (Elsevier, Amsterdam, 2004), p. 1.
- ⁸H. C. Koo, J. H. Kwon, J. Eom, J. Chang, S. H. Han, and M. Johnson, *Science* **325**, 1515 (2009).
- ⁹R. Winkler, *Spin-Orbit Coupling Effects in Two-Dimensional Electron and Hole Systems* (Springer, Berlin, 2003).
- ¹⁰L. Petersen and P. Hedegård, *Surf. Sci.* **459**, 49 (2000).
- ¹¹F. Reinert, *J. Phys. Condens. Matter* **15**, S693 (2003).
- ¹²J. H. Dil, *J. Phys. Condens. Matter* **21**, 403001 (2009).
- ¹³C. R. Ast, J. Henk, A. Ernst, L. Moreschini, M. C. Falub, D. Pacilé, P. Bruno, K. Kern, and M. Grioni, *Phys. Rev. Lett.* **98**, 186807 (2007).
- ¹⁴I. Gierz, T. Suzuki, E. Frantzeskakis, S. Pons, S. Ostanin, A. Ernst, J. Henk, M. Grioni, K. Kern, and C. R. Ast, *Phys. Rev. Lett.* **103**, 046803 (2009).
- ¹⁵C. R. Ast, D. Pacilé, L. Moreschini, M. C. Falub, M. Papagno, K. Kern, M. Grioni, J. Henk, A. Ernst, S. Ostanin, and P. Bruno, *Phys. Rev. B* **77**, 081407(R) (2008).
- ¹⁶L. Moreschini, A. Bendounan, C. R. Ast, F. Reinert, M. Falub, and M. Grioni, *Phys. Rev. B* **77**, 115407 (2008).
- ¹⁷H. Bentmann, F. Forster, G. Bihlmayer, E. V. Chulkov, L. Moreschini, M. Grioni, and F. Reinert, *Europhys. Lett.* **87**, 37003 (2009).
- ¹⁸C.-G. Duan, S. S. Jaswal, and E. Y. Tsymlal, *Phys. Rev. Lett.* **97**, 047201 (2006).
- ¹⁹J. P. Velev, C.-G. Duan, K. D. Belashchenko, S. S. Jaswal, and E. Y. Tsymlal, *J. Appl. Phys.* **103**, 07A701 (2008).
- ²⁰M. Fechner, I. V. Maznichenko, S. Ostanin, A. Ernst, J. Henk, P. Bruno, and I. Mertig, *Phys. Rev. B* **78**, 212406 (2008).
- ²¹C. Jia and J. Berakdar, *Appl. Phys. Lett.* **95**, 012105 (2009).
- ²²O. Krupin, G. Bihlmayer, K. Starke, S. Gorovikov, J. E. Prieto, K. Döbrich, S. Blügel, and G. Kaindl, *Phys. Rev. B* **71**, 201403(R) (2005).
- ²³S. Prakash, M. B. Karacor, and S. Banerjee, *Surf. Sci. Rep.* **64**, 233 (2009).
- ²⁴H. Mirhosseini, J. Henk, A. Ernst, S. Ostanin, C.-T. Chiang, P. Yu, A. Winkelmann, and J. Kirschner, *Phys. Rev. B* **79**, 245428 (2009).
- ²⁵G. Kresse and D. Joubert, *Phys. Rev. B* **59**, 1758 (1999).
- ²⁶*Electron Scattering in Solid Matter*, edited by J. Zabloudil, R. Hammerling, L. Szunyogh, and P. Weinberger (Springer, Berlin, 2005).
- ²⁷Forschungszentrum Jülich, Institut für Festkörperforschung, Institute Quantum Theory of Materials, D-52425 Jülich, Germany.
- ²⁸M. Fechner, S. Ostanin, and I. Mertig, *Phys. Rev. B* **77**, 094112 (2008).
- ²⁹T. Oguchi and T. Shishidou, *J. Phys.: Condens. Matter* **21**, 092001 (2009).

Paper V

Tunable Spin Gaps in a Quantum-Confined Geometry

Tunable Spin Gaps in a Quantum-Confined Geometry

Emmanouil Frantzeskakis,¹ Stéphane Pons,^{1,2,*} Hossein Mirhosseini,³ Jürgen Henk,³ Christian R. Ast,⁴ and Marco Grioni¹

¹Laboratoire de Spectroscopie Électronique, Institut de Physique des Nanostructures, École Polytechnique Fédérale de Lausanne (EPFL), station 3, CH-1015 Lausanne-Switzerland

²Laboratoire de Physique des Matériaux, Nancy-Université, CNRS, Boulevard des Aiguillettes, B.P. 239, F-54506 Vandoeuvre lès Nancy, France

³Max-Planck-Institut für Mikrostrukturphysik, Weinberg 2, D-06120 Halle (Saale), Germany

⁴Max-Planck-Institut für Festkörperforschung, D-70569 Stuttgart, Germany

(Received 26 May 2008; published 7 November 2008)

We have studied the interplay of a giant spin-orbit splitting and of quantum confinement in artificial Bi-Ag-Si trilayer structures. Angle-resolved photoelectron spectroscopy reveals the formation of a complex spin-dependent gap structure, which can be tuned by varying the thickness of the Ag buffer layer. This provides a means to tailor the electronic structure at the Fermi energy, with potential applications for silicon-compatible spintronic devices.

DOI: 10.1103/PhysRevLett.101.196805

PACS numbers: 73.20.At, 73.21.Fg, 79.60.Jv, 79.60.Bm

In nonmagnetic centrosymmetric bulk solids like silicon, electronic states of opposite spin have the same energy. A surface or an interface breaks the translational invariance of a three-dimensional crystal. Thus, as predicted by Bychkov and Rashba [1], the spin-orbit (SO) interaction can lead to spin-split electronic states in two-dimensional electron gases (2DEG), in asymmetric quantum wells [2], at a surface or at an interface [3,4]. The size of the splitting is related to the strength of the atomic SO coupling (i.e., to the gradient of the atomic potential [5]) and to the potential gradient perpendicular to the confinement [6]. An unexpectedly large splitting was recently reported for a Bi-Ag surface alloy grown on a Ag(111) single crystal [7]. It is attributed to an additional in-plane gradient of the surface potential, hence being a direct consequence of the chemical alloy configuration [7,8].

The spin-orbit interaction could be used to control via a gate voltage the dynamics of spins injected into a semiconductor [2,9–11]. Moreover, the spin Hall effect—also induced by the SO interaction—could find applications in new spintronic devices [12,13] which rely neither on magnetic materials nor on optical pumping. Interfaces between silicon and materials exhibiting large spin-orbit splitting are therefore expected to open novel vista for spintronics. The challenge is to control the electronic states and spin polarization at the Fermi level which determine the electron and spin transport through interfaces [14,15] and nanostructures. Among the heavy metals which exhibit strong spin-orbit interactions, bismuth may be favored for environmental considerations. Experiments on thin layers of bismuth on silicon have evidenced a SO splitting in the Bi surface states, but not of their bulk counterparts [16,17]. Moreover, it was observed that the splitting is removed by the hybridization between surface and bulk states.

In this Letter we explore a different approach. We fabricated trilayer systems composed of a Bi-Ag surface alloy [7], a thin Ag buffer layer of variable thickness d , and a Si

(111) substrate [Fig. 1(a)]. Along the z direction, the vacuum/BiAg/Ag/Si related potential is asymmetric and SO splitting of delocalized electronic states is expected. The good interfacial adhesion of the silver film makes the system stable at room temperature (RT) and results in a sharp interface. We investigated the complex interface by angle-resolved photoelectron spectroscopy (ARPES), supported by first-principles electronic-structure calculations. We find that the SO splitting is large. We also find that, due

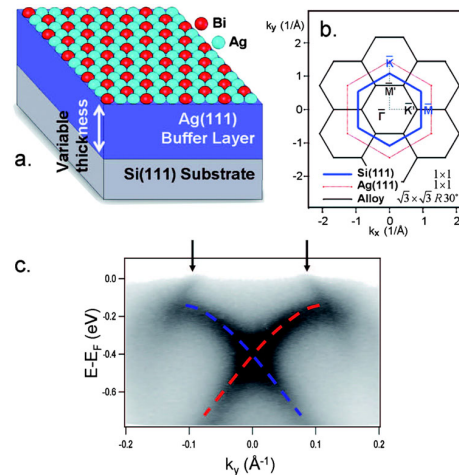


FIG. 1 (color online). (a) Schematic view of a trilayer sample. The $\sqrt{3} \times \sqrt{3}R30^\circ$ Bi-Ag alloy is grown on a Ag buffer—whose thickness can be varied—deposited on a silicon substrate. (b) First Brillouin zones of the surface structures. The symmetry lines $\bar{\Gamma}\bar{K}\bar{M}$ and $\bar{\Gamma}\bar{K}'\bar{M}'$ refer to Si(111) and to the alloy, respectively. (c) ARPES intensity of the surface states of a Bi-Ag alloy grown on a thick Ag layer deposited on Si(111) along $\bar{\Gamma}\bar{K}'\bar{M}'$. This system is similar to the alloy grown on a Ag(111) single crystal. Dashed lines indicate the branches of opposite spins of the sp_z surface state. Arrows point out bands of $p_x p_y$ symmetry. Close to $\bar{\Gamma}$ all bands exhibit a rotational symmetry around the surface normal.

to quantum confinement in the buffer layer, the electronic structure exhibits patches of highly spin-polarized spectral density. The spin-dependent density of states close to the Fermi energy can be tuned by the thickness of the Ag buffer.

The experiments were performed with a multichamber setup under an ultrahigh vacuum. During preparation, Si(111) (highly phosphorus doped, resistivity 0.009–0.011 $\Omega \cdot \text{cm}$) was flashed at 1200 °C by direct current injection. After the flashes, the substrate was cooled slowly in order to obtain a sharp 7×7 signature in low-energy electron diffraction (LEED). The Ag films were deposited with a homemade Knudsen cell while the sample was kept at 80 K and then annealed at 400 K. The quality of the silver thin film was checked by LEED. Ag grows in the [111] direction [18]. The $\sqrt{3} \times \sqrt{3}R30^\circ$ Bi-Ag surface alloy was obtained by depositing 1/3 ML of Bi with an EFM3 Omicron source on the sample at RT followed by a soft annealing. Angle-resolved photoemission spectroscopy (ARPES) spectra were acquired at RT and 55 K with a PHOIBOS 150 Specs analyzer. We used a monochromatized and partially polarized GammaData VUV 5000 high brightness source of 21.2 eV photons.

The first-principles electronic-structure calculations are based on the local spin-density approximation to density functional theory, as implemented in relativistic multiple-scattering theory (Korringa-Kohn-Rostoker and layer-Korringa-Kohn-Rostoker methods; for details, see Refs. [7,19]). Spin-orbit coupling is taken into account by solving the Dirac equation. The computer codes used consider the boundary conditions present in experiment, that is the semi-infinite substrate, a buffer of finite thickness, the surface, and the semi-infinite vacuum. The potentials of all sites (atoms) are computed self-consistently, except for the Si substrate which is mimicked by spherical repulsive potentials of 1 Hartree height. This so-called hard-sphere substrate follows the face-centered cubic structure of the Ag buffer. The electronic structure is addressed in terms of the spectral density which is obtained from the imaginary part of the Green function of the entire system. The latter can be resolved with respect to wave vector, site, spin, and angular momentum, thus allowing a detailed analysis of the local electronic structure.

The surface electronic properties of the alloy grown on top of a thick Ag film ($d = 80$ monolayers (ML)), as obtained by ARPES [Fig. 1(c)], agree with those of the alloy grown on a Ag(111) single crystal [7]. The spin-split bands which belong to electronic states with sp_z character cross at $\bar{\Gamma}$ (in-plane wave vector $\mathbf{k}_{\parallel} = \mathbf{0}$). They are well described by parabolas (effective mass $m^* = -0.35m_e$) which are offset by $\Delta k = \pm 0.13 \text{ \AA}^{-1}$. This shift in wave vector is a signature of the aforementioned Rashba effect. Two sets of side bands stem from electronic states of mainly $p_x p_y$ character which are also spin polarized but less split [7,8,20]. The $p_x p_y$ bands cross the Fermi level at $k_F^{\text{inner}} \approx \pm 0.09 \text{ \AA}^{-1}$ and $k_F^{\text{outer}} \approx \pm 0.21 \text{ \AA}^{-1}$. Electronic-

structure calculations [7] show that the Bi-Ag surface states are much more strongly localized in the top layer than the Ag(111) or Au(111) Shockley surface states. Thus, the spin-split bands and the giant SO splitting are not directly affected by the Ag/Si interface for Ag film thickness larger than a few monolayers. This implies that prior results for BiAg/Ag(111) [7] can be transferred to silicon technology [i.e., to BiAg/Ag/Si(111)] at RT.

A new and interesting situation arises for thinner Ag buffer layers, where d is of the order of the attenuation length of the electronic states. The Ag sp states are confined to the Ag film by the potential barrier (image-potential barrier) on the vacuum side (surface) and by the fundamental band gap of Si on the substrate side. This confinement leads to quantized wave vectors along z and to discrete energy levels [21]. These so-called quantum well states (QWS's) play a central role in transport properties [22] and in the coupling of magnetic layers in superlattices [23–25]. Ag/Si(111) QWS's, in particular, have been extensively studied by ARPES [18,26,27]. For Ag(111) films, their in-plane dispersion consists of a set of parabolic bands centered at $\bar{\Gamma}$, with energies determined by the film thickness [Fig. 2(a); $d = 17$ ML]. The electronic fringe structure with a negative parabolic dispersion appears due to the accumulation of QWS's near the k -dependent valence band edge of Si. This is an indirect manifestation of the heavily doped n -type character of the Si(111) substrates used here [18]. The narrow line shapes of the energy

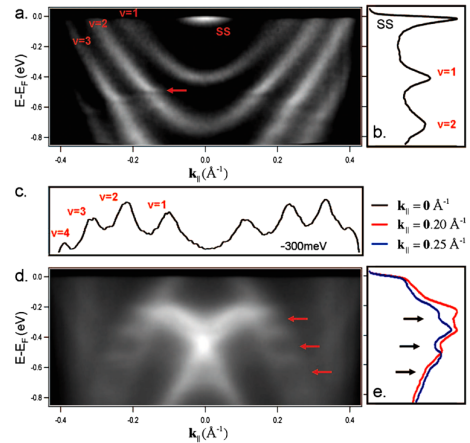


FIG. 2 (color online). (a) Raw ARPES data along $\bar{\Gamma}\bar{K}$ at 55 K. QWS's in a 17 ML bare Ag buffer deposited on Si(111). These parabolic states are numbered $\nu = 1 \dots n$. Kinks in the dispersion (arrow) are due to the hybridization of the QWS with the p bands of silicon. SS stands for the Shockley surface state of Ag (111). (b) EDC extracted from Fig. 2(a) at $\bar{\Gamma}$, i.e., $k = 0.0 \text{ \AA}^{-1}$. The 1st and 2nd QWS signatures and the SS are indicated. (c) MDC extracted from Fig. 2(a) at -300 meV shows the successive branches of the QWS. (d) Raw ARPES intensity along $\bar{\Gamma}\bar{M}'$ at 55 K of the Bi-Ag alloy grown on 17 ML of Ag. (e) EDC extracted from Fig. 2(d) for $k_{\perp} = 0.20 \text{ \AA}^{-1}$ and $k_{\perp} = 0.25 \text{ \AA}^{-1}$. Arrows indicate gaps of 100–200 meV in the dispersion of the $p_x p_y$ bands.

distribution curves [EDC's; Fig. 2(b)] and momentum distribution curves [MDC's; Fig. 2(c)], and the observation of the electronic fringes reflect the uniformity of the Ag buffers and the high resolution of the experiment.

We now consider the interaction of the spin-split alloy surface states and the QWS's in a BiAg/Ag/Si trilayer, focusing first on a 17 ML thick Ag buffer [Fig. 2(d); i.e., the sample of Fig. 2(a) covered by the Bi-Ag alloy). The Ag Shockley surface state disappears and the resulting surface electronic structure agrees in general with that of the system without Si substrate [BiAg/Ag(111); no QWS's] but shows intensity modulations in both the sp_z and p_xp_y bands. The energy distribution curves, extracted from the raw data, clearly evidence band gaps [Fig. 2(e)].

The remaining signature of the Ag QWS's (at large k values) and the gaps in Bi-Ag surface states are clearly seen even at RT in the second derivative of the ARPES intensities ($d^2I(E, \mathbf{k}_{\parallel})/dE^2$) for samples with selected Ag film thicknesses ($d = 19, 16,$ and 10 ML) in Fig. 3. The parabolic in plane dispersion of the QWS's (circles in Fig. 3) is obtained from MDC's of Ag/Si(111) with the corresponding Ag thicknesses [as presented in Fig. 2(c)]. Agreement between the parabolic fits (uncovered Ag buffer) and the QWS's of the alloyed sample is obtained after shifting rigidly the parabolas by 50–150 meV to lower binding energies. These shifts can be attributed to the different reflection properties of the bare Ag surface and

of the Bi-Ag surface alloy [28]. However, the effective masses of the QWS's may also change. Therefore, these fits are to be considered as guides to the eye. Band gaps are found at the intersection of the QWS parabola with both branches of the surface-alloy bands regardless of their symmetry or spin, providing strong evidence of their hybridization. The hybridization is spin selective [29,30]; thus, we can consider in a first approximation that the QWS are spin-degenerate or their spin-splitting is small. For thinner Ag buffers [10 ML; Fig. 3(c)], the number of QWS's is reduced. As a result, the number of band gaps is also decreased but their widths are larger, in particular, for the p_xp_y states.

To further corroborate the above interpretation of the band gaps, first-principles electronic-structure calculations for BiAg/Ag(111) reported in [7,19] were extended. Since the Ag/Si(111) interface is incommensurate [18], we are forced to approximate the Si substrate. Therefore, the confinement of the Ag QWS's by the Si(111) substrate is mimicked by replacing Ag bulk layers by repulsive potentials. The latter provide the complete reflection of the Ag states at the Ag/Si(111) interface. Note that by this means details of the Ag/Si interface are roughly approximated and the binding energies of the theoretical quantum well states may differ from experiment. However, the essential features are well captured, as will be clear from the agreement of experiment and theory discussed below. The systems investigated comprise the Bi-Ag surface alloy, Ag layers, and the substrate built from hard spheres [HS; i.e. BiAg/Ag $_{d-1}$ /HS(111)]. The theoretical analysis focuses on the wave vector and spin-resolved spectral density $N(E, \mathbf{k}_{\parallel}; \sigma)$ at a Bi site ($\sigma = \uparrow$ or \downarrow is the spin quantum number). Spin dependent band gaps are visualized by displaying $\Delta N(E, \mathbf{k}_{\parallel}) = N(E, \mathbf{k}_{\parallel}; \uparrow) - N(E, \mathbf{k}_{\parallel}; \downarrow)$.

For BiAg/Ag(111), the Bi surface states hybridize with Ag bulk states, resulting in a rather blurred spectral density [Fig. 4(a); compare Fig. 1(c) for the experiment]. For the systems with Si substrate, focusing here on exemplary results for $d = 10$ [Fig. 4(b)] and 19 [Fig. 4(c)], quantum well states show up as parabolas centered at $\bar{\Gamma}$. The most striking difference to BiAg/Ag(111) are, however, spin-dependent band gaps at $(E, \mathbf{k}_{\parallel})$ points at which the QWS's would cross the Bi bands. With increasing thickness of the Ag buffer, the number of gaps (or QWS's) increases and the width of the gaps decreases. The spectral densities of the Bi states are slightly less blurred than for BiAg/Ag(111) because hybridization with Ag states occurs only at the band gaps, due to quantization. Eventually, we find a shift of the QWS's energies upon covering the Ag buffer with the Bi-Ag alloy, as observed by the experiment.

We now focus on the agreement of the experimental findings and the present theoretical approach. Apart from the similar trends concerning the number and the width of the gaps with varying the buffer layer thickness, theory predicts the experimentally observed strong spectral weight of the remaining ungapped parts of the alloy states.

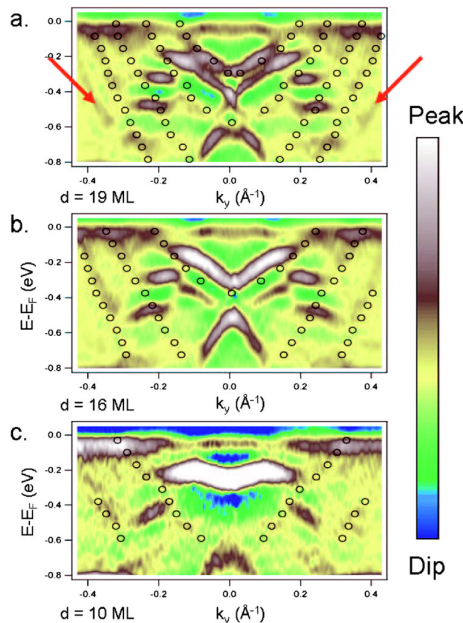


FIG. 3 (color online). (a),(b), and (c) second derivative of the ARPES intensity along $\bar{\Gamma}\bar{M}'$ for three alloy-covered samples at RT with different Ag film thicknesses, respectively, 19, 16, and 10 ML. Circles correspond to MDC fits of the QWS observed on the bare Ag thin films of the corresponding thicknesses shifted by 50–150 meV upwards in order to match the remaining parts of the QWS at large k values after Bi deposition (e.g., red arrows).

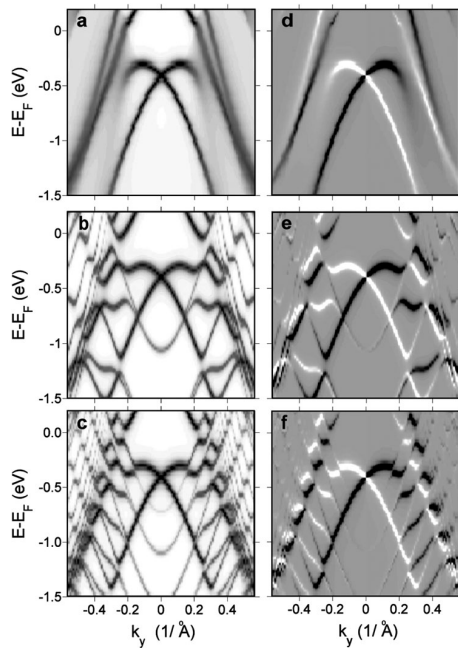


FIG. 4. Effect of QWS's on the spin-split electronic structure of the Bi/Ag surface alloy, as obtained from first-principles electronic-structure calculations. (a)–(c): The spectral density at the Bi site is displayed as gray scale (with white indicating vanishing spectral weight) for BiAg/Ag(111) (a) and BiAg/Ag/Si(111) for Ag buffer thicknesses $d = 10$ (b) and $d = 19$ (c). The wave vector is chosen as in the experiment (Fig. 3). (d)–(f): The spin polarization of the electronic states is visualized by $\Delta N(E, \mathbf{k}_{\parallel})$, i.e., the difference of the spin-up and the spin-down spectral density. White and black indicate positive and negative values, respectively, where gray is for zero ΔN .

Moreover, it points towards the association of the ungapped parts of the sidebands both with the $p_x p_y$ bands and the continuation of the sp_z band at large wave vectors. The finite experimental resolution prevents us from identifying each single contribution. Nevertheless, both in the experimental (Fig. 3) and the theoretical data [Figs. 4(e) and 4(f)], the overall shape of each ungapped structure of the sidebands exhibits a continuously changing curvature from positive to negative with decreasing d .

By contrast with what has been observed in Bi thin layers on silicon [16,17], the theoretical results of Figs. 4(e) and 4(f) clearly show that the Ag quantum well states are spin-polarized due to the Rashba effect. Close to $\bar{\Gamma}$, the branches of opposite spins of the QWS follow a parabolic dispersion and their momentum separation decreases with the Ag thickness. This feature is evident in the figures which show the spin polarization of the electron states. We now address, in particular, the electronic structure at the Fermi level. For $d = 10$ ML [Fig. 4(e)], highly spin-polarized states show up at $k_{\parallel} = k_F = 0.22 \text{ \AA}^{-1}$, with a spin polarization of about 33%. On the contrary, a complete gap appears for $d = 19$ ML [Fig. 4(f)]. These findings imply that the spin-dependent electronic structure at

the Fermi level—and thus the transport properties—can be drastically modified by the Ag film thickness.

Our findings for BiAg/Ag/Si(111) trilayers suggest that it is indeed possible to match systems with large spin-orbit splitting [here: BiAg/Ag(111)] with a semiconductor substrate. Furthermore, interfacial properties can be custom tailored, in the present case by a single parameter, namely, the Ag buffer layer thickness. In this respect, multilayer systems which comprise semiconducting Si layers and Rashba-split subsystems (like BiAg/Ag) may be very useful in the development of new spintronics devices. Tuning the band-gap structure at the Fermi level could also be achieved by chemical means, as was demonstrated for $\text{Bi}_x\text{Pb}_{1-x}\text{Ag}_2$ mixed alloys grown on Ag(111) [19]. Peculiar transport properties and spin Hall effects can be anticipated based on this interface, namely, in nanostructured systems or (Bi-Ag-Si) superlattices.

E.F. acknowledges the Alexander S. Onassis Public Benefit Foundation for financial support. This research was supported in part by the Swiss NSF and the NCCR MaNEP.

*Electronic address: stephane.pons@epfl.ch

- [1] Y. A. Bychkov and E. I. Rashba, JETP Lett. **39**, 78 (1984).
- [2] T. Koga *et al.*, Phys. Rev. Lett. **88**, 126601 (2002).
- [3] S. LaShell, B. McDougall, and E. Jensen, Phys. Rev. Lett. **77**, 3419 (1996).
- [4] E. Rotenberg, J. W. Chung, and S. Kevan, Phys. Rev. Lett. **82**, 4066 (1999).
- [5] D. Malterre *et al.*, New J. Phys. **9**, 391 (2007).
- [6] F. Forster, S. Hüfner, and F. Reinert, J. Phys. Chem. B **108**, 14692 (2004).
- [7] C. R. Ast *et al.*, Phys. Rev. Lett. **98**, 186807 (2007).
- [8] J. Prempere *et al.*, Phys. Rev. B **76**, 073310 (2007).
- [9] S. Datta and B. Das, Appl. Phys. Lett. **56**, 665 (1990).
- [10] D. Awschalom and M. Flaté, Nature Phys. **3**, 153 (2007).
- [11] J. Nitta *et al.*, Phys. Rev. Lett. **78**, 1335 (1997).
- [12] Y. Kato *et al.*, Nature (London) **427**, 50 (2004).
- [13] S. Valenzuela and M. Tinkham, Nature (London) **442**, 176 (2006).
- [14] F. Greullet *et al.*, Phys. Rev. Lett. **99**, 187202 (2007).
- [15] E. Tsymlal *et al.*, Prog. Mater. Sci. **52**, 401 (2007).
- [16] T. Hirahara *et al.*, Phys. Rev. Lett. **97**, 146803 (2006).
- [17] T. Hirahara *et al.*, Phys. Rev. B **76**, 153305 (2007).
- [18] N. Speer, S. Tan, and T.-C. Chiang, Science **314**, 804 (2006).
- [19] C. R. Ast *et al.*, Phys. Rev. B **77**, 081407(R) (2008).
- [20] F. Meier *et al.*, Phys. Rev. B **77**, 165431 (2008).
- [21] T.-C. Chiang, Surf. Sci. Rep. **39**, 181 (2000).
- [22] M. Jalochofski *et al.*, Phys. Rev. B **45**, 13 607 (1992).
- [23] J. E. Ortega and F. J. Himpsel, Phys. Rev. Lett. **69**, 844 (1992).
- [24] J. Ortega *et al.*, Phys. Rev. B **47**, 1540 (1993).
- [25] P. Bruno, Phys. Rev. B **52**, 411 (1995).
- [26] A. L. Wachs *et al.*, Phys. Rev. B **33**, 1460 (1986).
- [27] J. F. Sanchez-Royo *et al.*, Phys. Rev. B **66**, 035401 (2002).
- [28] T. Hirahara *et al.*, Phys. Rev. B **78**, 035408 (2008).
- [29] C. Didiot *et al.*, Phys. Rev. B **74**, 081404(R) (2006).
- [30] I. Barke *et al.*, Phys. Rev. Lett. **97**, 226405 (2006).

Paper VI

Electron correlation beyond local density approximation:
Self-interaction correction in Gadolinium

Electron correlation beyond the local density approximation: self-interaction correction in gadolinium

H Mirhosseini, A Ernst and J Henk

Max-Planck-Institut für Mikrostrukturphysik, Weinberg 2, D-06120 Halle (Saale), Germany

E-mail: [hossein@mpi-halle.de](mailto:hosseini@mpi-halle.de)

Received 9 March 2010, in final form 6 May 2010

Published 1 June 2010

Online at stacks.iop.org/JPhysCM/22/245601

Abstract

We report on detailed first-principles calculations which focus on the magnetic and structural properties of the (0001) surface of gadolinium. The electronic correlation within the localized 4f states is treated within the self-interaction correction (SIC), thus going beyond the local spin-density approximation. The ferromagnetic ground state is predicted correctly if the SIC is applied; the effect of surface relaxations on Heisenberg exchange parameters and on the Curie temperature are addressed by Monte Carlo calculations. The SIC also has a profound effect on the dispersion of the d surface states, due to hybridization of the 4f states with the 5d valence states. The best agreement with photoemission experiments is obtained within the transition state approximation, which takes into account the orbital relaxation. The Rashba spin-orbit coupling in the d surface states is fully captured by our relativistic multiple scattering approach.

(Some figures in this article are in colour only in the electronic version)

1. Introduction

Density functional theory (DFT) is the most widely used method for electronic structure calculations. Despite the success of the local spin-density approximation (LSD) to DFT, there are serious shortcomings: the properties of 3d metal oxides are described badly, the band gaps of semiconductors are underestimated, in *f*-systems the density of states is in strong disagreement with experiment, in some cases the LSD gives qualitatively wrong results for Mott–Hubbard insulators, to name a few. Some of the discrepancies are due to the restriction of DFT to describe the ground state properties, but some failures can be attributed to the partial cancellation of the spurious self-interaction of an electron with itself, which is present in the Kohn–Sham (KS) effective potential. This kind of systematic error can be corrected by removing the self-interaction from the total energy functional [1]. Application of the self-interaction correction (SIC) to transition metal oxides (TMOs) [2] and wide-gap semiconductors [3], for example, shows promising results. Another method to study TMOs and semiconductors is LDA + *U* [4], which adds an on-site Coulomb interaction to the LSDA functional [5]. LDA+*U* was used to study other systems with localized electrons such as

gadolinium [6]. However, in this method the on-site Coulomb interaction *U* is an adjustable parameter and is chosen to optimize agreement with experiment.

Gd is a prototype for investigation of the electron correlation. Correct treatment of the strongly localized 4f states changes the ground state magnetic ordering from antiferromagnetic to ferromagnetic. Other properties of Gd also improve when the electron correlation is taken into account. The surface states of Gd(0001), which are mostly *d*_{z²} majority states, hybridize with the localized 4f majority states. As we will see later the SIC of the localized states has a significant effect on the surface states and is essential. So far, to our knowledge, all studies on Gd bulk and Gd(0001) have been done by means of LDA + *U* or a 4f-core model [6–8]. In this paper we report the results of an *ab initio* investigation of the SIC in the bulk and on the (0001) surface of Gd.

Applying the SIC to calculate the ground state properties of Gd, e.g. magnetic ordering and local magnetic moments, is very successful. For excited states, it appears that the binding energies of the SI-corrected localized levels are significantly too large when compared to those determined from spectroscopical data, i.e. from photoemission intensities. This ‘overcorrection’ of the SIC is attributed to the orbital

relaxation. SIC calculations are ground state calculations and one cannot expect accurate results for excited states. In our calculations we used the transition state approximation (TSA), that is an average of two ground state potentials (LSD and SIC potentials), to obtain a better agreement with experiments that are associated with the excited states.

The paper is organized as follows: in section 2 local SIC and TSA are explained in detail. Section 3 is devoted to the calculated magnetic properties of Gd bulk and Gd(0001). The surface states and the effect of the Rashba splitting on the surface states are also studied. The paper ends with a summary in section 4.

2. Computational aspects

First-principles calculations were performed within the framework of multiple scattering theory, using scalar-relativistic and relativistic Korringa–Kohn–Rostoker (KKR) computer codes. The self-consistent KKR scheme allows us to treat semi-infinite systems. Consequently, the entire system comprises the Gd bulk, the surface region (six Gd layers and four vacuum layers), and the vacuum region. The image potential barrier is mimicked by so-called empty spheres.

Spin–orbit coupling is included by solving the Dirac equation in our relativistic layer KKR code. The layer- and wavevector-resolved spectral density

$$N_{al}(E, \vec{k}_{\parallel}) = -\frac{1}{\pi} \text{Im Tr } G_{al,al}^+(E, \vec{k}_{\parallel}) \quad (1)$$

provides detailed information on the electronic structure. Here, $G^+(E, \vec{k}_{\parallel})$ is the side limit of the site-diagonal Green function at energy E and in-plane wavevector \vec{k}_{\parallel} . The trace is over the muffin-tin sphere of site a in layer l . The spectral density can be decomposed with respect to spin and angular momentum, to give access to the relevant properties.

All calculations are performed with the experimental structural parameters of $a = 6.866$ bohr and $c/a = 1.59$ [9]. The interlayer distance at the surface is reduced with respect to the bulk, as has been determined experimentally [10]. A surface relaxation of 4% contraction is taken into account.

2.1. Self-interaction correction

The self-interaction correction, which is implemented according to [11] in terms of local orbital- and spin-dependent potentials, is applied to the electronic states of Gd. Based on this method, the degree of localization is determined by the energy derivative of the single-site phase shift, that is the Wigner delay time [12]. For a localized state, characterized by the main quantum number n , angular momentum $L = (l, m)$, and spin σ , the charge density is

$$n_{L\sigma}^{(n)\text{SIC}}(\vec{r}) = -\frac{1}{\pi} \int_{E_1}^{E_2} \text{Im } G_{L\sigma, L\sigma}(\vec{r}, \vec{r}; \epsilon) d\epsilon, \quad (2)$$

where E_1 and E_2 lie slightly below and above the energy of the state ($nL\sigma$). This charge density is used to construct the effective self-interaction potential,

$$V_{\text{eff}, L\sigma}^{(n)\text{LSD-SIC}}(\vec{r}) = V_{\text{eff}, \sigma}^{\text{LSD}}(\vec{r}) + V^{\text{SIC}}(\vec{r}), \quad (3)$$

where

$$V^{\text{SIC}}(\vec{r}) = -V_{\text{H}}[n_{L\sigma}^{(n)\text{SIC}}](\vec{r}) - V_{\text{xc}}^{\text{LSD}}[n_{L\sigma}^{(n)\text{SIC}}, 0](\vec{r}). \quad (4)$$

Hence, the Hartree (H) and the exchange–correlation (xc) potential of the localized state are explicitly subtracted from the effective potential. Note that this correction vanishes for delocalized states.

For each SI-corrected channel ($n\tilde{L}\tilde{\sigma}$), indicated by a tilde, the ($\tilde{L}\tilde{\sigma}$) element of the single-site scattering matrix $t^{(n)}$, calculated within the local spin-density approximation, is replaced by that obtained from the SI-corrected potential,

$$\tilde{t}_{L\sigma}^{(n)} = t_{L\sigma}^{(n)}(1 - \delta_{L\sigma, \tilde{L}\tilde{\sigma}}) + t_{L\sigma}^{(n)\text{LSD-SIC}} \delta_{L\sigma, \tilde{L}\tilde{\sigma}}. \quad (5)$$

The resulting scattering matrix $\tilde{t}^{(n)}$ is then used to calculate the SI-corrected scattering-path operator which enters the KKR Green function [13]. The self-interaction is thus corrected self-consistently, without any adjustable parameter. Further, the set of SI-corrected channels is determined by total energy minimization. For Gd it turns out that all 4f majority states have to be corrected.

At present, there is no relativistic version of the SIC. To investigate the effect of the SIC on effects which are mediated by the spin–orbit coupling—in particular the Rashba effect in the majority surface state—we thus proceed as follows. We employ a scaling transformation of the (radial) Dirac equation which allows us to switch between the fully relativistic (including spin–orbit coupling) and the scalar-relativistic description (excluding spin–orbit coupling) [14]. This transformation is applied only to the SI-corrected 4f majority levels, thus keeping the relativistic description for all other electronic states, in particular for the d surface states. By this means we rely on the non-relativistic SIC but in a relativistic framework.

2.2. Transition state approximation

In the calculation of the ground state properties, e.g. magnetic ordering and local magnetic moments, the SI correction is applied with full strength. For excited states, it appears that the binding energies of the SI-corrected localized levels are significantly too large when compared to those determined from spectroscopical data, i.e. from photoemission intensities. This ‘overcorrection’ of the SIC is attributed to the orbital relaxation.

The density functional theory of Hohenberg, Kohn, and Sham applies only if the occupation numbers of the orbitals are either zero or one. If the occupancy of one of the single-particle states has been changed, one has to generalize the theory by including the occupation number, as was done by Janak [15]. According to Janak’s theorem, the derivative of the total energy E with respect to the orbital occupation is equal to the eigenenergy ϵ_{α} of the corresponding orbital,

$$\frac{\partial E}{\partial f_{\alpha}} = \langle \psi_{\alpha} | H^{\text{LSD}} | \psi_{\alpha} \rangle = \epsilon_{\alpha}, \quad (6)$$

where H^{LSD} is the LSD Hamiltonian and f_α is the occupation number of the orbital ψ_α . The relaxation energy $\Delta E_{\text{relaxed}}$ is calculated by removing an electron from an occupied state,

$$\Delta E_{\text{relaxed}} = - \int_0^1 \epsilon_\alpha(f_\alpha) df_\alpha. \quad (7)$$

The total energy E includes the relaxation of all orbitals due to the change of the occupation number. Several ways to calculate the removal energy have been proposed [16] but they lead to unphysical effects [17].

We start from the Taylor expansion of the eigenvalue as a function of the occupation number in the neighborhood of F_α ,

$$\epsilon_\alpha(f_\alpha) \approx \epsilon(F_\alpha) + (f_\alpha - F_\alpha) \left(\frac{\partial \epsilon}{\partial f_\alpha} \right)_{f_\alpha=F_\alpha}. \quad (8)$$

The restriction to the first order is justified if the eigenvalue depends almost linearly on its occupation number [18, 19]. Inserting (8) into (7) and integrating from $f_\alpha = 1$ to $1 - p$ gives

$$E(f_\alpha = 1 - p) - E(f_\alpha = 1) = -p\epsilon_\alpha(F_\alpha) + \left[\frac{p^2}{2} - p(1 - F_\alpha) \right] \left(\frac{\partial \epsilon_\alpha}{\partial f_\alpha} \right)_{f_\alpha=F_\alpha}. \quad (9)$$

To have a method similar to Koopmans' theorem one would need the eigenvalues at full occupancy. For $F_\alpha = 1$ and $p = 1$,

$$\Delta E_{\text{relaxed}} = -\epsilon_\alpha(1) + \frac{1}{2} \left(\frac{\partial \epsilon_\alpha}{\partial f_\alpha} \right)_{f_\alpha=1}. \quad (10)$$

The first term is the energy of the fully occupied orbital α . The second term accounts for the orbital's relaxation. This term includes a 'non-Koopmans'-like correction (relaxation of the localized state) and the relaxation energy (relaxation of the other orbitals). In many applications to localized states, the relaxation is significant. To achieve an accurate electron removal energy, this term has to be included in the energy calculation. Using the Hellmann–Feynman theorem [20], the second term on the right-hand side of (10) can be written as

$$\frac{\partial \epsilon_\alpha}{\partial f_\alpha} = \langle \psi_\alpha | \frac{\partial H^{\text{LSD}}}{\partial f_\alpha} | \psi_\alpha \rangle. \quad (11)$$

If the relaxation of other orbitals is neglected (in analogy to Koopmans' theorem), then (11) reduces to

$$\frac{\partial \epsilon_\alpha}{\partial f_\alpha} = \langle \psi_\alpha | u_\alpha + \rho_\alpha \frac{\partial \epsilon_{\text{xc}}}{\partial \rho} | \psi_\alpha \rangle, \quad (12)$$

where u_α is the Coulomb potential associated with orbital α and ϵ_{xc} is the exchange–correlation energy per particle. For $f_\alpha = 1$, the first term is the self-Coulomb interaction of an electron. The second term is the change of the exchange–correlation energy (to first order in the occupation number) of the system due to removing one electron from the orbital α . Equation (12) can be interpreted as the self-interaction of an orbital whose occupation number is reduced. Adding this positive term to the energy of the orbital α increases the removal energy calculated within the LSD. Thus, the

removal energy of a localized orbital with corrected potential V_α becomes

$$\Delta E_{\text{unrelaxed}} = -\langle \psi_\alpha | H^{\text{LSD}} | \psi_\alpha \rangle - \frac{1}{2} \langle \psi_\alpha | V_\alpha^{\text{SIC}} | \psi_\alpha \rangle. \quad (13)$$

This is the unrelaxed removal energy when an electron is removed from orbital α . The removal energy is larger than its experimental counterpart because the relaxation of other orbitals is neglected.

As is apparent from (13), the removal energy of the orbital α is calculated with half strength of the SIC potential associated with this orbital. By this method, i.e. by calculating the LSD and the SIC ground state potentials, one obtains removal energies with good accuracy [3, 17]. Following previous works we call this approach the transition state approximation (TSA).

2.3. Exchange parameters and Curie temperature

The self-interaction correction also affects the exchange interaction among the Gd sites. To address this issue, we calculated the Curie temperature of both the bulk and the surface. The Curie temperature is calculated within the Heisenberg model by Monte Carlo simulations (MCSs). The exchange parameters J_{ij} are calculated by means of the Liechtenstein formula [21]. The critical temperature is determined accurately by the fourth-order Binder cumulant [22].

3. Results and discussion

3.1. Magnetic structure

The total energy minimization implies that all 4f majority states have to be SI corrected. As a result, their binding energies increase sizably from about 5.0 eV for LSD to about 17.0 eV for SIC (figure 1). Consequently, these states become more localized.

The magnetic ground state is changed from antiferromagnetic ordering, as obtained within the LSD approximation, to ferromagnetic ordering upon application of the SIC. The LDA + U method also predicts the magnetic ordering ground state and the magnetic moment correctly but relies on adjustable parameters. In LDA + U calculations the change of magnetic ordering was attributed to the removal of the 4f minority states from the Fermi level to larger energies [6, 7]. A small shift of the minority states is found in our calculations as well; it is a result of the charge redistribution.

For the ferromagnetic ground state, Heisenberg exchange parameters J_{ij} were computed for Gd bulk (figure 2). For the first three nearest neighbors the coupling is ferromagnetic ($J_{ij} > 0$); the exchange parameters for larger distances change sign and oscillate (inset of figure 2). However, the exchange parameters decrease (in absolute value) rapidly with distance; for example, J_{ij} of the sixth shell is about 5% of that of the first shell.

To address the effect of the surface relaxation on the exchange parameters, a calculation was performed for two slabs with 12-layer thickness, one unrelaxed, the other with 4%

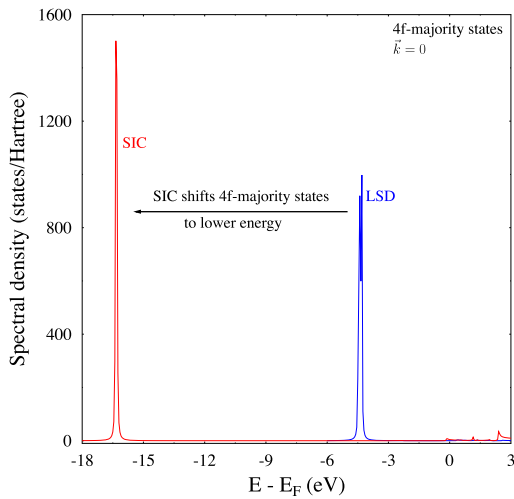


Figure 1. Effect of self-interaction correction on the binding energy of 4f majority states in bulk Gd(0001). The spin-resolved spectral density is calculated within the local spin-density (LSD) approximation and within the self-interaction correction (SIC) at $\vec{k}_{\parallel} = 0$.

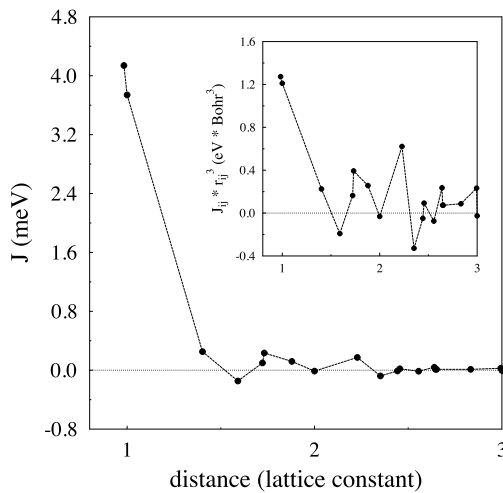


Figure 2. Heisenberg exchange parameters J_{ij} of Gd bulk (top). To emphasize the oscillations of the J_{ij} , we show $J_{ij}r_{ij}^3$ in the inset (r_{ij} distance of sites i and j).

surface contraction (figure 3). The relaxation has a profound effect on the surface J_{ij} ; more precisely, this J_{ij} is increased by about 50%. Thus, we expect a sizable effect on the Curie temperature for the slabs. Please note that in any case the magnetic coupling of the surface layer with the sub-surface layer is ferromagnetic.

We applied MCSs for three 12-layer slabs: (i) with J_{ij} taken from the bulk calculation ('bulk'), (ii) with J_{ij} for the unrelaxed surface ('unrelaxed'), and (iii) with J_{ij} for the relaxed surface ('relaxed'). In accordance with the increasing exchange parameters, in particular those of the first shells, T_C increases as well: from 320 to 330 K for 'bulk' via 330–340 K

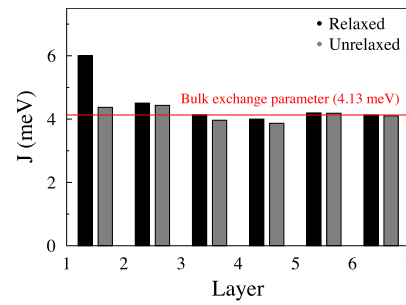


Figure 3. Effect of the surface relaxation on the Heisenberg exchange parameters. The bars represent J_{ij} of the first shell with sites located in adjacent layers (black with 4% surface contraction; gray without surface relaxation).

for 'unrelaxed' up to 380–400 K for 'relaxed'. To be more precise, the exchange parameter of the first shell is 4.13 meV for 'bulk', 4.37 meV for 'unrelaxed', and 6.00 meV for 'relaxed'. Consequently, T_C for the 'bulk' case matches best the experimental bulk value of 293 K [23]. We also performed MCSs for 'bulk' systems with a significantly increased size; in all cases T_C was within the range reported above. Please note that slabs are free-standing Gd layers with two surfaces. Therefore it is not possible to compare our results directly with experiments [24].

The findings reported in the preceding evidence the importance of the self-interaction correction for the magnetic ordering in systems with correlated electrons. Second, they show the importance of the surface relaxation to the critical temperature. The increased Heisenberg exchange parameters at the surface result in an enhanced T_C as compared to the unrelaxed system.

3.2. Surface state dispersion and Rashba spin-orbit coupling

So far, all calculated properties, such as magnetic ordering and geometrical constants, were associated with the ground state. To take into account the relaxation of electrons due to an excitation we applied the transition state approximation.

In figure 4 the spectral density of the 4f majority states in Gd(0001) calculated within the LSD, SIC, and TSA is shown. Compared with experimental values (gray bar), the LSD predicts too low a binding energy, while the SIC produces too high a binding energy (cf. the 'overcorrection' in figure 1). Applying the TSA, the binding energy increases to 10.5 eV, which is in reasonable agreement with the experimental value (8.0–8.5 eV).

The occupied surface states of Gd(0001) are mostly d_{z^2} majority states which hybridize with the 4f majority states. Consequently, the treatment of the electronic correlation within the 4f states has an effect on both binding energy and dispersion of the surface states. The d–f hybridization of the surface state can be quantified by the ratio of the d and f contributions to its spectral density N at $\vec{k}_{\parallel} = 0$. The d–f hybridization of the surface state is larger for SIC ($d/f = 7$) than for LSD ($d/f = 50$), which is at first glance

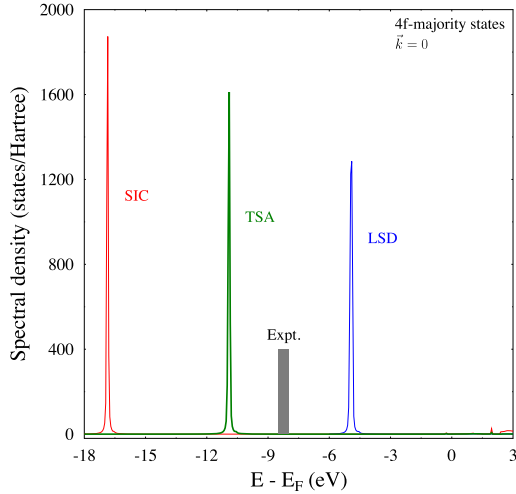


Figure 4. Effect of the electronic correlation on the binding energy of 4f majority states in the surface layer of Gd(0001). The spectral density at $\vec{k}_{\parallel} = 0$ is calculated within the local spin-density approximation (LSD), the self-interaction correction (SIC), and the transition state approximation (TSA). The range of experimental binding energies [6] is marked by the gray bar (of arbitrary height).

counterintuitive. A closer inspection of the spectral density shows that the d contribution to the majority surface state does not change upon application of TSA or SIC. However, spectral weight of f majority character is transferred from the unoccupied to the occupied states and is mixed into the d majority surface state for TSA and SIC. This ‘band-filling’ effect manifests itself in the decreasing d/f ratios and in the increased magnetic moments for TSA and SIC ($8.0 \mu_B$), as compared to LSD ($8.0 \mu_B$).

The majority surface state dispersion of Gd(0001) is shown in figure 5. For the LSD approximation, the binding energy of 0.22 eV at $\vec{k}_{\parallel} = 0$ ($\vec{\Gamma}$) deviates sizably from the experimental result (0.16 eV, dots). More striking, however, is the positive dispersion at small wavevectors, which does not match the negative dispersion in experiment. Application of the SIC leaves the binding energy almost unchanged (0.23 eV) but results in a strongly negative dispersion, which also does not fit to experiment. The surface state dispersion calculated by the TSA shows a plateau at small k_{\parallel} , and the binding energy of 0.18 eV almost hits that of the experiment.

In a non-magnetic crystal with inversion symmetry the electronic states are not spin polarized, due to Kramers’ degeneracy. The spin degeneracy is the result of both time-reversal and inversion symmetry. At surfaces the inversion asymmetry results, via the spin-orbit coupling (SOC), in a splitting in the dispersion relation. At a magnetic surface, spin degeneracy is lifted by the exchange interaction and majority spins are aligned along the quantization axis. The effect of the spin-orbit interaction is mainly modification of the energy dispersion, i.e. moving the dispersion relations with respect to each other. Figure 6 depicts the spin structure of split surface states at a non-magnetic and a magnetic surface.

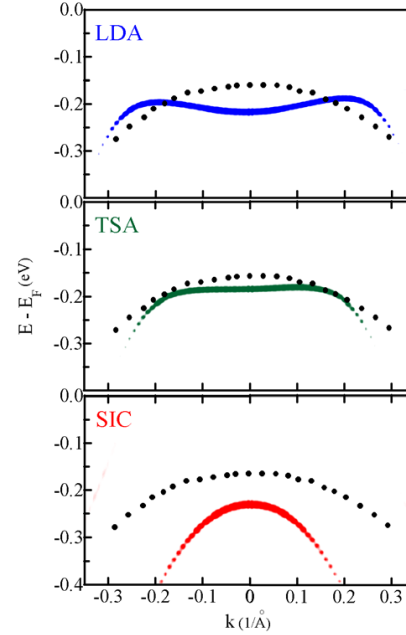


Figure 5. Effect of electronic correlations on the d_{z^2} majority surface state of Gd(0001). The spectral densities calculated within the local spin-density (LSD) approximation, the transition state approximation (TSA), and the self-interaction correction (SIC) are shown along the $\vec{M}-\vec{\Gamma}-\vec{M}$ line of the surface Brillouin zone. Experimental data (dots) are reproduced from [8].

The spin-orbit interaction and magnetism are taken into account on equal footing in our relativistic layer KKR code. For clarity, we reproduce the TSA data from figure 5 and add eye-guiding horizontal lines in figure 7. As a consequence of the Rashba SOC, the surface state dispersion, as obtained from the spectral density at the surface, becomes asymmetric in the direction normal to the in-plane magnetization. As in experiment, the maximum of the dispersion is shifted off the Brillouin center to positive \vec{k}_{\parallel} . We note in passing that magnetization reversal ($\vec{M} \rightarrow -\vec{M}$) mirrors the dispersion, that is $E(\vec{k}_{\parallel}, \vec{M}) = E(-\vec{k}_{\parallel}, -\vec{M})$. Further, the dispersion maximum of the associated d minority state (not shown here) is shifted oppositely to that of the majority surface state.

From figure 7 one might conclude that the Rashba effect is overestimated in theory. One possible reason could be too large an asymmetry of the surface state confinement, which essentially determines the size of the Rashba effect. Although we cannot rule out this explanation, there may be a few other explanations for this mismatch between theory and experiment. (i) The TSA is a first-order perturbation to SIC and LSD; it does not rely on an adjustable parameter. Thus, the curvature of the surface states could perhaps be better described within LDA + U but at the cost of the adjustable parameter U (which is fitted to experimental data). (ii) The effective mass of surface states is sometimes overestimated in KKR, in which the vacuum region is described by so-called empty muffin-tin spheres on the parent lattice (here

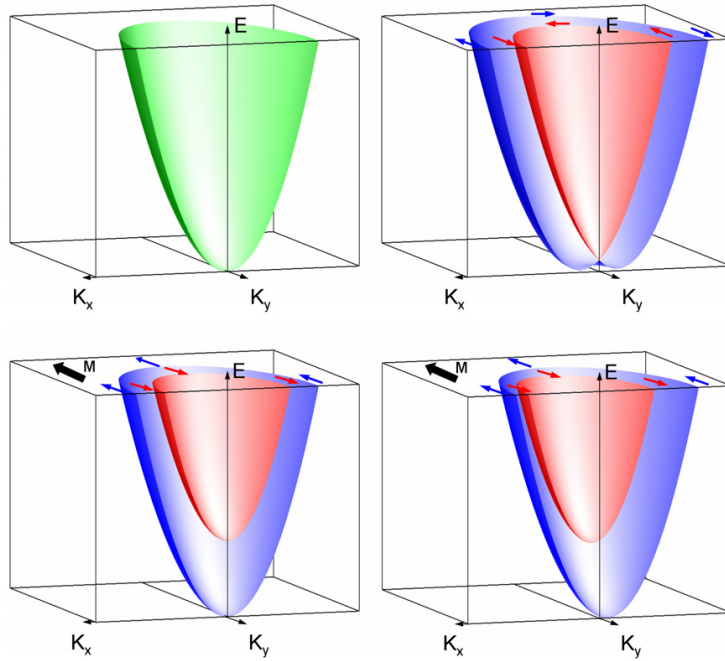


Figure 6. The schematic spin structure of Rashba-split and exchange-split surface states at a non-magnetic surface (top) and at a magnetic surface (bottom). The left panels show systems with inversion symmetry while the right panels show systems without inversion symmetry. The Rashba spin-orbit coupling in a ferromagnetic two-dimensional electron with in-plane magnetization \vec{M} removes the inversion symmetry of the spin-split band structure, $E(+\vec{k}_{\parallel}) \neq E(-\vec{k}_{\parallel})$ for $\vec{k}_{\parallel} \perp \vec{M}$.

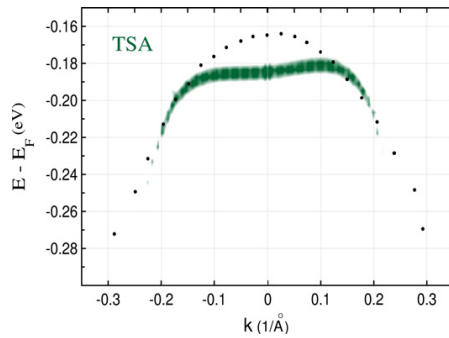


Figure 7. The d majority surface states of Gd(0001) calculated within TSA. The Rashba effect shows up as asymmetry of the dispersion ($E(\vec{k}) \neq E(-\vec{k})$). The in-plane magnetization is perpendicular to \vec{k}_{\parallel} , \vec{k}_{\parallel} along $\vec{M}-\vec{\Gamma}-\vec{M}$. Experimental data (dots) are reproduced from [8].

hcp(0001)). This effect showed up for example in the free-electron-like surface state on Au(111); see [25]. (iii) The experimental dispersion was obtained from the peak positions in angle-resolved photoemission spectra. The maxima are typically rather broad for ferromagnetic systems (about 0.2–0.3 eV FWHM in figure 1(a) of [8]) and, thus, introduce some uncertainty in the detailed dispersion.

Summarizing this section, we conclude that the TSA considerably improves the description of excited states in

systems with electronic correlations, as compared to the LSD approximation and the SIC. Although the agreement with spectroscopical data, e.g. photoemission, is not as good as in LDA + U, we would like to add in favor of the TSA that it does not rely on any adjustable parameters, like the Hubbard parameters U and J in LDA + U approaches [5]. The latter are typically chosen to reproduce experiments.

The hybridization of the 4f majority states (which are treated by SIC) with the d majority surface state has a profound effect on both the binding energy and the dispersion of the latter. On top of the TSA treatment, we have shown that even the Rashba spin-orbit coupling in the surface states is captured correctly. As a result, we conclude that an advanced treatment of the electronic correlation in the localized spin-polarized states is not only important for the magnetic structure but also improves the properties of the valence states.

4. Concluding remarks

The present first-principles study on Gd(0001) shows that the self-interaction correction to the local spin-density approximation improves considerably the description of ground state properties of correlated systems. Its flavor for excited states, i.e. the transition state approximation, is able to describe correctly spectroscopic data. In summary, we have dealt successfully with a complex interplay of electronic correlations, surface relaxation, and spin-orbit coupling on the magnetic ordering, the Curie temperature, and the surface state

dispersion. A key issue in our multiple scattering theoretical calculations is that these do not rely on any adjustable parameter which is related to electronic correlations.

The combination of *ab initio* calculations beyond LSDA and Monte Carlo calculations makes it possible to extend the Curie temperature calculation to more realistic systems, e.g. to Gd(0001)/W(110). This system shows in particular a thickness dependence of the Curie temperature [24].

Acknowledgment

We are grateful for helpful discussion with M Lüders (Daresbury).

References

- [1] Perdew J P and Zunger A 1981 Self-interaction correction to density-functional approximations for many-electron systems *Phys. Rev. B* **23** 5048
- [2] Däne M, Lüders M, Ernst A, Ködderitzsch D, Temmerman W M, Szotek Z and Hergert W 2009 Self-interaction correction in multiple scattering theory: application to transition metal oxides *J. Phys.: Condens. Matter* **21** 045604
- [3] Filippetti A and Spaldin N A 2003 Self-interaction-corrected pseudopotential scheme for magnetic and strongly-correlated systems *Phys. Rev. B* **67** 125109
- [4] Anisimov V I, Solovyev I V, Korotin M A, Czyzyk M T and Sawatzky G A 1993 Density-functional theory and NiO photoemission spectra *Phys. Rev. B* **48** 16929
- [5] Anisimov V I, Aryasetiawan F and Lichtenstein A I 1997 First principles calculation of the electronic structure and spectra of strongly correlated systems: the LDA + *U* method *J. Phys.: Condens. Matter* **9** 767
- [6] Shick A B, Pickett W E and Fadley C S 2000 Electron correlation effects and magnetic ordering at the Gd(0001) surface *Phys. Rev. B* **61** R9213
- [7] Kurz Ph, Bihlmayer G and Blügel S 2002 Magnetism and electronic structure of hcp Gd and Gd(0001) surface *J. Phys.: Condens. Matter* **14** 6353
- [8] Krupin O, Bihlmayer G, Starke K, Gorovikov S, Prieto J E, Döbrich K, Blügel S and Kaindl G 2005 Rashba effect at magnetic metal surfaces *Phys. Rev. B* **71** 201403(R)
- [9] Norman M, Harris I R and Raynor G V 1966 The lattice spacings of thorium-rich solid solutions with praseodymium, samarium, gadolinium and erbium *J. Less-Common Met.* **11** 395
- [10] Giergiel J, Hopster H, Lawrence J M, Hemminger J C and Kirschner J 1995 A video-based spin-polarized LEED data-acquisition system *Rev. Sci. Instrum.* **66** 3475
- [11] Lüders M, Ernst A, Däne M, Szotek Z, Svane A, Ködderitzsch D, Hergert W, Györfly B L and Temmerman W M 2005 Self-interaction correction in multiple scattering theory *Phys. Rev. B* **71** 205109
- [12] Wigner E P 1955 Lower limit for the energy derivative of the scattering phase shift *Phys. Rev.* **98** 145
- [13] Gonis A and Butler W H 2000 *Multiple Scattering in Solids* (Berlin: Springer)
- [14] Ebert H, Freyer H, Vernes A and Guo G Y 1996 Manipulation of the spin-orbit coupling using the Dirac equation for spin-dependent potentials *Phys. Rev. B* **53** 7721
- [15] Janak J F 1978 Proof that $\delta\epsilon/\delta n_i = \epsilon_i$ in density-functional theory *Phys. Rev. B* **18** 7165
- [16] Schulthess T C, Temmerman W M, Szotek Z, Svane A and Petit L 2007 First-principles electronic structure of Mn-doped GaAs, GaP, and GaN semiconductors *J. Phys.: Condens. Matter* **19** 165207
- [17] Svane A, Christensen N E, Petit L, Szotek Z and Temmerman W M 2006 Electronic structure of rare-earth impurities in GaAs and GaN *Phys. Rev. B* **74** 165204
- [18] Harris M and Ballone P 1999 Electronic removal energies from density functional computations *Chem. Phys. Lett.* **303** 420
- [19] Göransson C, Olovsson W and Abrokosov I A 2005 Numerical investigation of the validity of the Slater-Janak transition-state model in metallic systems *Phys. Rev. B* **72** 134203
- [20] Parr R G and Yang W 1989 *Density-Functional Theory of Atoms and Molecules* (New York: Oxford University Press)
- [21] Lichtenstein A I, Katsnelson M I, Antopov V P and Gubanov V A 1987 Local spin density functional approach to the theory of exchange interactions in ferromagnetic metals and alloys *J. Magn. Mater.* **67** 65–74
- [22] Binder K and Heermann D W 1997 *Monte Carlo Simulation in Statistical Physics: An Introduction* (Berlin: Springer)
- [23] Jensen J and Mackintosh A R 1991 *Rare Earth Magnetism* (Oxford: Clarendon)
- [24] Farle M, Baberschke K, Stetter U, Aspelmeier A and Gerhardt F 1993 Thickness-dependent Curie temperature of Gd(0001)/W(110) and its dependence on the growth conditions *Phys. Rev. B* **47** 11571
- [25] Henk J, Hoesch M, Osterwalder J, Ernst A and Bruno P 2004 Spin-orbit coupling in the L-gap surface states of Au(111): spin-resolved photoemission experiments and first-principles calculations *J. Phys.: Condens. Matter* **16** 7581

Bibliography

- [1] G. Dresselhaus. Spin-orbit coupling in zinc blende structures. *Phys. Rev.*, 100:580, 1955.
- [2] Y. A. Bychkov and E. I. Rashba. Oscillatory effects and the magnetic susceptibility of carriers in inversion layers. *J. Phys.: Condens. Matt.*, 17:6039, 1984.
- [3] S. LaShell, B. A. McDougall, and E. Jensen. Spin splitting of an Au(111) surface state band observed with angle-resolved photoelectron spectroscopy. *Phys. Rev. Lett.*, 77:3419, 1996.
- [4] F. Reinert. Spin-orbit interaction in the photoemission spectra of noble metal surface states. *J. Phys.: Condens. Matt.*, 15:S693, 2003.
- [5] Chr. R. Ast, J. Henk, A. Ernst, L. Moreschini, M. C. Falub, D. Pacilé, P. Bruno, K. Kern, and M. Grioni. Giant spin splitting through surface alloying. *Phys. Rev. Lett.*, 98:186807, 2007.
- [6] J. Henk, M. Hoesch, J. Osterwalder, A. Ernst, and P. Bruno. Spin-orbit coupling in the L-gap surface states of Au(111): Spin-resolved photoemission experiments and first-principles calculations. *J. Phys.: Condens. Matt.*, 16:7581, 2004.
- [7] J. Prempfer, M. Trautmann, J. Henk, and P. Bruno. Spin-orbit splitting in an anisotropic two-dimensional electron gas. *Phys. Rev. B*, 76:073310, 2007.
- [8] S. G. Davison and M. Stęślicka. *Basic Theory of Surface States*. Clarendon, Oxford, 1992.
- [9] R. de L. Kronig and W. G. Penney. Quantum mechanics of electrons in crystal lattices. *Proc. Roy. Soc. A*, 130:499, 1931.
- [10] W. Shockley. On the surface states associated with a periodic potential. *Phys. Rev.*, 56:317, 1939.
- [11] J. Zak. Symmetry criterion for surface states in solids. *PRB*, 32:2218, 1985.
- [12] P. M. Echenique and J. B. Pendry. The existence and detection of rydberg states at surfaces. *JPhysC*, 11:2065, 1978.

- [13] P. Strange. *Relativistic Quantum Mechanics: With Applications in Condensed Matter and Atomic Physics*. Cambridge University Press, Cambridge, 1998.
- [14] L. Petersen and P. Hedegård. A simple tight-binding model of spin-orbit splitting of *sp*-derived surface states. *Surf. Sci.*, 459:49, 2000.
- [15] O. Krupin, G. Bihlmayer, K. Starke, S. Gorovikov, J. E. Prieto, K. Döbrich, S. Blügel, and G. Kaindl. Rashba effect at magnetic metal surfaces. *Phys. Rev. B*, 71:201403(R), 2005.
- [16] R. G. Parr and W. Yang. *Density-Functional Theory of Atoms and Molecules*. Oxford University Press, New York, 1989.
- [17] P. Hohenberg and W. Kohn. Inhomogeneous electron gas. *Phys. Rev. B*, 136:864, 1964.
- [18] W. Kohn and L. J. Sham. Self-consistent equations including exchange and correlation effects. *Phys. Rev.*, 140:A1133, 1965.
- [19] R. M. Martin, editor. *Electronic Structure. Basic Theory and Practical Methods*. Cambridge University Press, Cambridge, 2004.
- [20] J. P. Perdew and A. Zunger. Self-interaction correction to density-functional approximations for many-electron systems. *Phys. Rev. B*, 23:5048, 1981.
- [21] M. R. Pederson, R. A. Heaton, and C. C. Lin. Density-functional theory with self-interaction correction: Application to the lithium molecule. *J. Chem. Phys.*, 82:2688, 1985.
- [22] F. Aryasetiawan. GW method for 3d and 4f systems. *Phys. B*, 237–238:321, 1997.
- [23] A. Svane and O. Gunnarsson. Transition-metal oxides in the self-interaction-correction density-functional formalism. *Phys. Rev. Lett.*, 65:1148, 1990.
- [24] Z. Szotek, W. M. Temmerman, and H. Winter. Self-interaction correction of localized bands within the LMTO-ASA band structure method. *Phys. B*, 172:19, 1991.
- [25] A. Filippetti and N. A. Spaldin. Self-interaction-corrected pseudopotential scheme for magnetic and strongly-correlated systems. *Phys. Rev. B*, 67:125109, 2003.
- [26] M. Lüders, A. Ernst, M. Däne, Z. Szotek, A. Svane, D. Ködderitzsch, W. Hergert, B. L. Györffy, and W. M. Temmerman. Self-interaction correction in multiple scattering theory. *Phys. Rev. B*, 71:205109, 2005.
- [27] E. P. Wigner. Lower limit for the energy derivative of the scattering phase shift. *Phys. Rev.*, 98:145, 1955.

- [28] J. F. Janak. Proof that $\delta E / \delta n_i = \epsilon_i$ in density-functional theory. *Phys. Rev. B*, 18:7165, 1978.
- [29] T. C. Schulthess, W. M. Temmerman, Z. Szotek, A. Svane, and L. Petit. First-principles electronic structure of mn-doped gaas, gap, and gan semiconductors. *J. Phys.: Condens. Matt.*, 19:165207, 2007.
- [30] A. Svane, N. E. Christensen, L. Petit, Z. szotek, and W. M. Temmerman. Electronic structure of rare-earth impurities in gaas and gan. *Phys. Rev. B*, 74:165204, 2006.
- [31] A. R. Williams, R. A. Robert, A. deGroot, and C. B. Sommers. Generalization of slater’s transition state conceot. *J. Chem. Phys.*, 63:628, 1975.
- [32] M. Harris and P. Ballone. Electronic removal energies from density funtional computations. *Chem. Phys. Lett.*, 303:420, 1999.
- [33] C. Göransson, W. Olovsson, and I. A. Abrokosov. Numerical investigation of the validity of the slater-janak transition-state model in metallic systems. *Phys. Rev. B*, 72:134203, 2005.
- [34] J. C. Slater. Damped Electron Waves in Crystals. *Phys. Rev.*, 51:840–846, 1937.
- [35] A. Gonis W. H. Butler. *Multiple Scattering in Solids*. Springer, 2000.
- [36] P. Weinberger. *Electron Scattering Theory of Ordered and Disordered Matter*. Clarendon Press, Oxford, 1990.
- [37] B. L. Gyorffy and M. J. Stott. In D. J. Fabian and L. M. da Watson, editors, *Band Structure Spectroscopy of Metals and Alloys*. Academic, New York, 1973.
- [38] J. Zabloudil, R. Hammerling, L. Szunyogh, and P. Weinberger, editors. *Electron Scattering in Solid Matter*. Springer, Berlin, 2005.
- [39] J. S. Faulkner and G. M. Stocks. Calculating properties with the coherent-potential approximation. *Phys. Rev. B*, 21:3222, 1980.
- [40] J. M. MacLaren, S. Crampin, D. D. Vvedensky, and J. B. Pendry. Layer Korringa-Kohn-Rostoker technique for surface and interface electronic properties. *Phys. Rev. B*, 40:12164, 1989.
- [41] C. R. Ast, D. Pacilé and L. Moreschini, M. C. Falub, M. Papagno, K. Kern, M. Gri-
oni, J. Henk, A. Ernst, S. Ostanin, and P. Bruno. Spin-orbit split two-dimensional
electron gas with tunable Rashba and Fermi energy. *Phys. Rev. B*, 77:081407(R),
2008.
- [42] C. R. Ast, H. J. Dil, I. Gierz, and F. Meier. private communication.

- [43] L. Moreschini, A. Bendounan, H. Bentmann, M. Assig, K. Kern, F. Reinert J. Henk, C. R. Ast, and M. Grioni. Influence of the substrate on the spin-orbit splitting in surface alloys on (111) noble-metal surfaces. *Phys. Rev. B*, 80:035438, 2009.
- [44] K. Wittel and R. Manne. Accurate calculation of ground-state energies in an analytic Lanczos expansion. *Theor. chim. Acta.*, 33:347, 1974.
- [45] T. Inui, Y. Tanabe, and Y. Onodera. *Group Theory and Its Applications in Physics*, volume 78 of *Springer Series in Solid State Sciences*. Springer, Berlin, 1990.
- [46] T. Hirahara, T. Nagao, I. Matsuda, G. Bihlmayer, E. V. Chulkov, Yu. M. Koroteev, P. M. Echenique, M. Saito, and S. Hasegawa. Role of spin-orbit coupling and hybridization effects in the electronic structure of ultrathin Bi films. *Phys. Rev. Lett.*, 97:146803, 2006.

Acknowledgment

I am indebted to my supervisor Jürgen Henk who gave me the chance to join the theory group at MPI. I deeply appreciate his great help during the three years of my PhD work. My special regards go to Arthur Ernst for his support and friendship. I should not forget to thank Patrick Bruno. I learned a lot from the group discussions conducted by him.

Ina Goffin deserves my gratitude because of the kind assistance she has been always providing. My sincere thanks are given to Udo Schmidt, who has helped me work with the (sometimes unfriendly) computers and machines.

I am also thankful to Prof. Gross for providing me the opportunity to stay in Halle for more years. Since his presence as the director of our department, I have been enjoying the membership in a large scientific group.

Finally I would like to thank all my friends for providing a warm pleasant atmosphere at work and offering love and support in social life. Being with them makes my life more delightful. I owe deep gratefulness to Yeganeh for her love, support and understanding in these years.

Hossein

مايلم از مامان، بابا، كامبيز و نيلوفر به خاطر حضور هميشگي شان، در دوری و نزديکی، محبت و همراهی
شان سپاسگزارى كنم.

حسين

Erklärung an Eides statt

Hiermit erkläre ich, dass ich die vorliegende Arbeit selbstständig und ohne fremde Hilfe verfasst, andere als die von mir angegebenen Quellen und Hilfsmittel nicht benutzt und die den benutzten Werken wörtlich oder inhaltlich entnommenen Stellen als solche kenntlich gemacht habe.

Eine Anmeldung der Promotionsabsicht habe ich an keiner anderen Fakultät einer Universität oder Hochschule beantragt.

Hossein Mirhosseini
Halle (Saale), 20.05.2010

Curriculum Vitae

Hossein Mirhosseini

Address: Max-Planck-Institute of Microstructure Physics
Weinberg 2, D-06120 Halle, Germany

Email: hossein@mpi-halle.mpg.de

Personal data:

- Birth day and place: January 1976, Yazd Iran
- Nationality: Iranian
- Sex/Marital status: Male/Married

Education:

- **PhD (Since June 2007)**
 - Theory department, MPI, Halle Germany
 - Supervisor: PD Dr. Jürgen Henk
 - Title of thesis : *Ab initio* investigations of the Rashba spin-orbit coupling in the electronic structure of surfaces
- **MSc (September 2005-May 2007)**
 - Applied Material Physics division, department of Materials Science and Engineering, KTH, Stockholm Sweden
 - Supervisor: Dr. Pavel Korzhavyi
 - Title of thesis: Theoretical study of the physical properties of 3d-metal doped Zinc oxide
- **BSc (September 1997-June 2002)**
 - Materials science and engineering department, Sharif university, Tehran Iran

